

## **INFORMATION TO USERS**

**This manuscript has been reproduced from the microfilm master. UMI films the text directly from the original or copy submitted. Thus, some thesis and dissertation copies are in typewriter face, while others may be from any type of computer printer.**

**The quality of this reproduction is dependent upon the quality of the copy submitted. Broken or indistinct print, colored or poor quality illustrations and photographs, print bleedthrough, substandard margins, and improper alignment can adversely affect reproduction.**

**In the unlikely event that the author did not send UMI a complete manuscript and there are missing pages, these will be noted. Also, if unauthorized copyright material had to be removed, a note will indicate the deletion.**

**Oversize materials (e.g., maps, drawings, charts) are reproduced by sectioning the original, beginning at the upper left-hand corner and continuing from left to right in equal sections with small overlaps.**

**Photographs included in the original manuscript have been reproduced xerographically in this copy. Higher quality 6" x 9" black and white photographic prints are available for any photographs or illustrations appearing in this copy for an additional charge. Contact UMI directly to order.**

**ProQuest Information and Learning  
300 North Zeeb Road, Ann Arbor, MI 48106-1346 USA  
800-521-0600**

**UMI<sup>®</sup>**



RICE UNIVERSITY

**Analyzing Dynamics and Stimulus Feature Dependence in the  
Information Processing of Crayfish Sustaining Fibers**

by

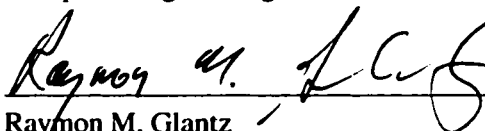
**Christopher John Rozell**

A THESIS SUBMITTED  
IN PARTIAL FULFILLMENT OF THE  
REQUIREMENTS FOR THE DEGREE  
**MASTER OF SCIENCE**

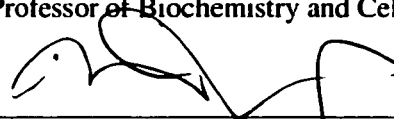
APPROVED, THESIS COMMITTEE:



Don H. Johnson, Chair  
J.S. Abercrombie Professor of Electrical and  
Computer Engineering and of Statistics



Raymon M. Glantz  
Professor of Biochemistry and Cell Biology



Robert Nowak  
Assistant Professor of Electrical and Computer  
Engineering

Houston, Texas

April, 2002

**UMI Number: 1408705**



---

**UMI Microform 1408705**

**Copyright 2002 by ProQuest Information and Learning Company.  
All rights reserved. This microform edition is protected against  
unauthorized copying under Title 17, United States Code.**

---

**ProQuest Information and Learning Company  
300 North Zeeb Road  
P.O. Box 1346  
Ann Arbor, MI 48106-1346**

## **ABSTRACT**

### **Analyzing Dynamics and Stimulus Feature Dependence in the Information Processing of Crayfish Sustaining Fibers**

by

Christopher John Rozell

The sustaining fiber (SF) stage of the crayfish visual system converts analog stimulus representations to spike train signals. A recent theory quantifies a system's information processing capabilities and relates to statistical signal processing. To analyze SF responses to light stimuli, we extend a wavelet-based algorithm for separating analog input signals and spike output waveforms in composite intracellular recordings. We also present a time-varying RC circuit model to capture nonstationary membrane noise spectral characteristics. In our SF analysis, information transfer ratios are generally on the order of  $10^{-4}$ . The SF information processing dynamics show transient peaks followed by decay to steady-state values. A simple theoretical spike generator is analyzed analytically and shows general dynamic and steady-state properties similar to SFs. The information transfer ratios increase with spike rate and dynamic properties are due to direct spike generator dependence on input changes.

## **Acknowledgments**

I would like to thank Dr. Raymon Glantz and Dr. Rob Nowak for taking the time to serve on my thesis committee. Your comments and feedback have been very helpful and caused me to consider many issues I would have neglected otherwise. A special thank you is also in order to Dr. Glantz both for providing the data analyzed in this work and for his valuable guidance as I learn about neural systems. Dr. Don Johnson has been an excellent advisor and mentor, exhibiting wisdom, experience, and patience that is invaluable as I progress in this field. I am also grateful to my truly wonderful family and friends who provide endless support and are the joy of my life.

# Contents

Abstract	ii
Acknowledgments	iii
List of Figures	vi
<b>1 Introduction</b>	<b>1</b>
<b>2 Background</b>	<b>3</b>
2.1 Neural Communication . . . . .	3
2.2 The Crayfish Visual Pathway . . . . .	5
2.3 Experimental Setup . . . . .	6
2.4 A Theory of Information Processing . . . . .	8
<b>3 Data Preparation</b>	<b>13</b>
3.1 Intracellular Sustaining Fiber Recordings . . . . .	13
3.2 Extension to Wavelet-Based Spike Separation Algorithm . . . . .	14
3.3 Electrical Noise (Hum) Removal . . . . .	18
<b>4 Calculating Kullback-Leibler Distances</b>	<b>21</b>
4.1 Estimating Spike KL Distances . . . . .	21
4.2 Estimating EPSP KL Distances . . . . .	23
4.2.1 Neurophysiologic Model . . . . .	26
4.2.2 Model-Based EPSP KL Calculation . . . . .	30
4.3 Stimulus Dependent Latency: Comparing KLs . . . . .	33

<b>5</b>	<b>Data Analysis</b>	<b>37</b>
5.1	Sudden-Onset Light Intensity Dataset 1 ( $LI_1$ ) . . . . .	37
5.2	Sudden-Onset Light Intensity Dataset 2 ( $LI_2$ ) . . . . .	49
5.3	Sine-wave Grating Spatial Frequency Dataset 1 ( $SW_1$ ) . . . . .	60
5.4	Sine-wave Grating Spatial Frequency Dataset 2 ( $SW_2$ ) . . . . .	63
5.5	Sine-wave Grating Orientation (Motion Direction) Dataset ( $SD$ ) . . . . .	71
5.6	Theoretical Spike Generator Example . . . . .	72
<b>6</b>	<b>Conclusions</b>	<b>78</b>
	<b>References</b>	<b>83</b>
<b>A</b>	<b>Membrane Physiology</b>	<b>85</b>
<b>B</b>	<b>Correlation structure of a non-stationary system</b>	<b>89</b>
<b>C</b>	<b>Analytic Analysis of Theoretical Spike Generator</b>	<b>92</b>



## List of Figures

2.1	General neuron anatomy. . . . .	3
2.2	The crayfish visual pathway. . . . .	6
2.3	Sine-wave grating stimulus. . . . .	7
2.4	Input and output signals to the SF. . . . .	9
3.1	Example EPSP response. . . . .	14
3.2	Coefficients from wavelet transform of example SF recording. . . . .	15
3.3	Locating action potentials in SF recordings. . . . .	17
3.4	Smoothed EPSP approximation. . . . .	17
3.5	Example results from the wavelet-based spike separation algorithm. . . . .	18
3.6	Power spectrum of a mean EPSP before and after hum removal. . . . .	20
4.1	RC circuit model of resting membrane. . . . .	27
4.2	Example EPSP, time-varying membrane resistance and moving pole. . . . .	29
4.3	Stimulus dependent delay in the crayfish visual pathway. . . . .	34
4.4	Correction for stimulus dependent delay. . . . .	35
5.1	Mean EPSP signals from dataset $LI_1$ . . . . .	38
5.2	Post-stimulus time (PST) histograms from dataset $LI_1$ . . . . .	39
5.3	Dataset $LI_1$ EPSP responses with stimulus-dependent delay removed. . . . .	40
5.4	SF input (EPSP) KL distances for dataset $LI_1$ . . . . .	43
5.5	Total SF EPSP KL distances for dataset $LI_1$ . . . . .	44
5.6	SF output (spike) KL distances for dataset $LI_1$ . . . . .	45

5.7	Total SF spike response KL distances for dataset $LI_1$ . . . . .	46
5.8	SF information transfer ratios for dataset $LI_1$ . . . . .	47
5.9	Steady-state SF information transfer ratios for dataset $LI_1$ . . . . .	48
5.10	Mean EPSP signals from dataset $LI_2$ . . . . .	49
5.11	Post-stimulus time (PST) histograms from dataset $LI_2$ . . . . .	50
5.12	Dataset $LI_2$ EPSP responses with stimulus-dependent delay removed. . . . .	51
5.13	SF input (EPSP) KL distances for dataset $LI_2$ . . . . .	54
5.14	Total SF EPSP KL distances for dataset $LI_2$ . . . . .	55
5.15	SF output (spike) KL distances for dataset $LI_2$ . . . . .	56
5.16	Total SF spike response KL distances for dataset $LI_2$ . . . . .	57
5.17	SF information transfer ratios for dataset $LI_2$ . . . . .	58
5.18	Steady-state SF information transfer ratios for dataset $LI_2$ . . . . .	59
5.19	Mean EPSP signals from dataset $SW_1$ . . . . .	61
5.20	Post-stimulus time (PST) histograms for dataset $SW_1$ . . . . .	62
5.21	Total SF EPSP KL distances for dataset $SW_1$ . . . . .	63
5.22	Total SF spike response KL distances for dataset $SW_1$ . . . . .	64
5.23	SF information transfer ratios for dataset $SW_1$ . . . . .	65
5.24	Mean EPSP signals from dataset $SW_2$ . . . . .	66
5.25	Post-stimulus time (PST) histograms from dataset $SW_2$ . . . . .	67
5.26	Total SF EPSP KL distances for dataset $SW_2$ . . . . .	68
5.27	Total SF spike response KL distances for dataset $SW_2$ . . . . .	69
5.28	SF information transfer ratios for dataset $SW_2$ . . . . .	70
5.29	Information processing summary for dataset $SD$ . . . . .	71

5.30	Information processing characteristics for a simple theoretical spike generator. . . .	73
5.31	Sample mean EPSPs, estimated spike rates from data and predicted event rates. . .	75
5.32	Information processing characteristics of a time-varying spike generator. . . . .	76
6.1	Graphical description of information transfer ratio . . . . .	79

## **Chapter 1**

### **Introduction**

In the crayfish visual pathway, the sustaining fibers (SFs) comprise the first stage where an analog representation of light stimuli is converted to a spike train. Clearly, information from the light stimulus is encoded in the SF output spike train, but what is not evident is how much information present in the input signal is lost in the conversion process. Analyzing a system that takes signals with different forms as input and output (e.g., analog input and point process output) is very difficult using traditional signal processing methods. A recent theory of information processing quantifies how well changes in a system's input are reflected in the system's output. This theory works regardless of the form of the input and output signals, and relates a system's information processing capabilities to statistical signal processing. Although this theoretical framework can analyze a general system, many practical problems arise in analyzing a real-world system. The present work addresses many of these practical problems in the context of analyzing the SF stage of the crayfish visual pathway.

Systems may selectively "filter" information: some types of informational changes at the input will be reflected in the output with more fidelity than others. One question considered here is whether SF information processing varies with stimulus feature. We consider whether different stimulus features (e.g., light intensity, spatial frequency, motion direction) are represented in the SF output spike train with comparable fidelity. When sudden-onset light stimuli are used, SFs have transient and steady-state segments in both the SF input and output responses. We also consider the dynamics of SF information processing capabilities by analyzing the sustaining fibers' time-varying encoding efficiency.

Chapter 2 provides introductions to the crayfish visual pathway (including the experiments performed to collect SF data) and the theory of information processing we employ. A number of technical details need consideration before information-processing based data analysis can be performed. Chapter 3 describes the preliminary steps taken to prepare the data for analysis, including our extension to a wavelet-based technique for separating SF input and output signals from a composite recording. Chapter 4 presents the details of our information processing analysis methods, including development of a model for SF input response characteristics. The resulting SF analysis is presented in Chapter 5. Conclusions are drawn and future work detailed in Chapter 6.

## Chapter 2

### Background

#### 2.1 Neural Communication

Sensorineural systems gather information about the outside world and communicate that information to higher centers of the brain. These systems contain both transducers to convert stimulus energy into electrochemical signals, and neurons to communicate and process those signals. Neural morphology varies throughout a biological system, but typical neurons have three distinct components: an input region, an integrative region, and an output path, seen in figure 2.1. The *dendritic*

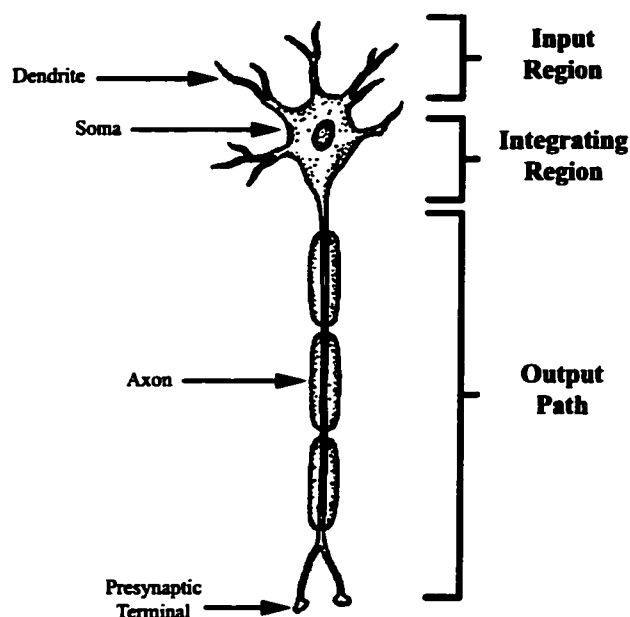


**Figure 2.1** Basic anatomy of a general neuron (adapted from [16]). Typical neurons have three distinct regions: an input region generally consisting of dendrites, an integration region made up of the cell body and the output path composed of the axon. The axon terminates in a presynaptic terminal that forms a synapse with an adjacent neuron.

*tree* makes up most of a neuron's input region. The cell body, or *soma* contains the biological components common to all cells, housing the machinery necessary to maintain cellular function. The

soma also typically serves as the neuron's integrating region, combining inputs initiated in distinct portions of the dendritic tree. The *axon* is the major extension projecting away from the soma to another neuron. Axons carry neural output signals away from the soma and end in a *synapse*, making a connection to another neuron's input region. The synapse consists of the *presynaptic terminal* (a specialized area on the sending neuron) and a *postsynaptic terminal* (a specialized area on the receiving neuron) [16, 20]. A typical neuron has many dendrites but only one axon.

Neurons represent signals by an electrical potential across the cell membrane. In most neurons, input analog potentials in the soma drive the stochastic production of *action potentials*, or spikes in membrane electrical potential. Spike trains actively propagate down the axon as a neural output signal. Spike waveforms are generally stereotyped, leaving only event timing as the significant feature. The action potential rising phase is quite fast ( $\sim 1$  ms), and the falling phase is slightly slower. The whole event typically lasts only a few milliseconds ( $\sim 10$  ms in crustaceans,  $\sim 1$ –2 ms in mammals). Spike trains are frequently modeled mathematically as *point processes*, stochastic processes completely defined by event timing [11]. In neurons only needing to communicate over very short distances, graded (analog) potentials may be passed directly to adjacent neurons without generating action potentials.

When action potentials (or graded potentials in non-spiking neurons) reach the presynaptic terminal, a chemical neurotransmitter is released into the extracellular space. The transmitter presence at the adjacent neuron's postsynaptic terminal generates an excitatory postsynaptic potential (EPSP). The resulting current travels down the electrical gradient from the dendrite to the soma and is integrated with inputs from other dendrites [16, 20].

Neural communication is difficult to analyze in part because the system adapts based on what has previously occurred in each neuron. For instance, when the EPSP in a neuron's integrative

region (also called the spike initiating zone) crosses a threshold, an action potential is produced. This threshold varies, depending on recent activity history. For example, after spike generation the system goes through both an absolute and a relative refractory period. During the absolute refractory period, the threshold is very high, making it virtually impossible to generate another spike. Following the absolute refractory period is a relative refractory period when the threshold is elevated, allowing spike generation but only with stronger than normal input [20]. When EPSPs are present (or absent) for an extended period of time, the threshold can exhibit extended adaptations.

## **2.2 The Crayfish Visual Pathway**

The crayfish optic lobe presents an interesting system, useful for studying information representation in a sensorineural system. The retina of the crayfish compound eye has groups of photoreceptors projecting down the visual pathway in a 1:1 fashion to a column of interneurons in the medulla. These retinotopically organized interneurons synapse on sustaining fiber (SF) dendrites [18]. The crayfish visual pathway up to and including a SF is depicted in figure 2.2. The SFs are the system analyzed in this report. In crayfish, fourteen distinct SFs have been identified. The retinotopic organization of the medullary interneurons together with the sustaining fibers' unique dendritic architectures result in each SF having its own distinct, well-defined receptive field. The SFs have overlapping receptive fields and the ensemble covers the entire panoramic visual field [18, 27].

SFs are spiking neurons whose projections include the optomotor neurons responsible for eye-stalk reflex movement. The photoreceptors and interneurons comprising the pre-sustaining fiber optic pathway have been shown to be non-spiking [26], and SFs have been shown to have little interaction with each other [19]. Therefore, SF input EPSPs closely resemble graded and delayed versions of summed photoreceptor activity over a segment of the visual field. The SFs are critical



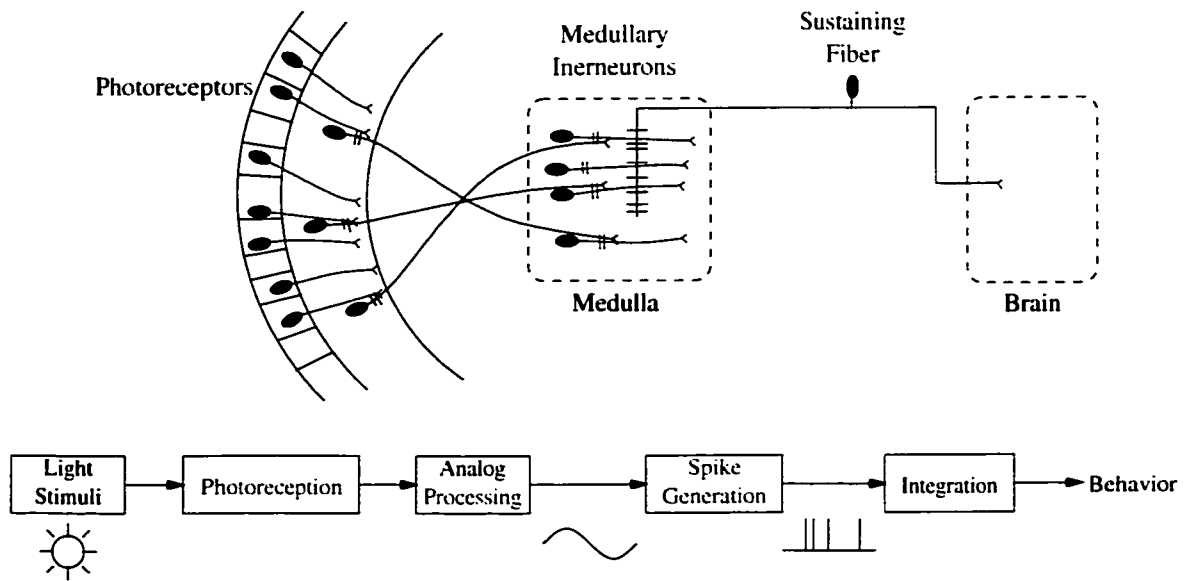


**Figure 2.2** Shown is a diagram depicting the crayfish visual pathway up to and including a SF. Light is transduced by the retinal photoreceptors. Each group of photoreceptors in the compound eye project in a 1:1 fashion to a column of medullary interneurons. The medullary interneurons synapse on SFs, which produce spike train outputs. The pre-SF pathway is non-spiking, so the SF receive graded and delayed signals representing summed photoreceptor activity over a receptive field.

from an information processing perspective because they are the first stage where an analog signal representing an outside stimulus is converted to a discrete spike train. From a signal processing point of view, the SFs represent a “front-end” for later information processing in higher centers of the brain.

### 2.3 Experimental Setup

In the data analyzed here, an intracellular SF recording was made with a microelectrode placed near the spike initiating zone. More detail about preparing the resulting data records for analysis is given in Chapter 3. The preparation is placed in a holding apparatus and eye position is secured. The fixed preparation is surrounded by a projection surface for light stimuli. Stimuli can be moved through the visual field with a specified direction and speed while recording from the SF. Data collection experimental methods are fully described in [17–19, 26].

Both the input EPSPs and the output spike trains are known to exhibit transient and steady-state behavior proportional to stimulus intensity [18, 27]. We are interested in examining and comparing the information transfer efficiency during these different response segments and sudden onset stimuli are used to elicit strong transient behavior. During a sudden onset experiment, the preparation is dark-adapted and a light stimulus with a specific intensity is suddenly presented over the SF receptive field. A small set of intensity values are pre-selected and several trials performed with each stimulus.

We would also like to explore how neural coding efficiency varies with stimulus feature. Sine-wave grating stimuli were also used to contrast the sudden-onset stimuli. An example sine-wave grating is shown in figure 2.3. Two-dimensional sine-wave gratings are specified by their con-

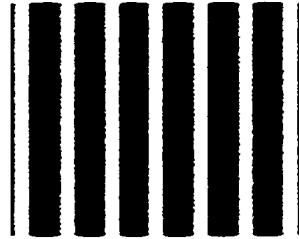


**Figure 2.3** *An example sine-wave grating. This stimuli is moved through the visual field at a particular orientation. The sine-wave grating is specified by the spatial frequency, the contrast, the orientation and the temporal frequency of the movement.*

trast, spatial frequency (measured in gratings/degree), motion direction, and the speed (temporal frequency) of one cycle. The contrast parameter in this type of stimuli is given as

$$Contrast = \frac{I_{\max} - I_{\min}}{I_{\max} + I_{\min}},$$

where  $I_{\max}$  and  $I_{\min}$  are the maximum and minimum intensity values. Sine-wave gratings present a slowly increasing and decreasing light intensity to the SF visual field, contrasting the sudden onset stimuli described above.

## 2.4 A Theory of Information Processing

As mentioned previously, SFs have analog EPSP input signals and discrete (point process) spike train outputs. This disparity precludes application of many standard signal processing system evaluation techniques. For example, a traditional transfer function cannot be constructed for such a system, and a cross-correlation between an analog input and point-process output is difficult. To characterize a sustaining fiber's coding efficiency it is necessary to abstract from the standard *signal* processing framework (centered around signal form), and consider a system's *information* processing function. A system processing signals also processes information content, letting some information components pass through while others components are filtered out. A theory has recently been introduced that quantifies a system's information processing capabilities regardless of the form of its input and output signals [12, 13, 24]. This information processing theory is the basis of the crayfish SF analysis presented here, and is summarized.

In this information processing framework, information (such as a light stimulus parameter) is conveyed by a stochastic signal with a probability law that depends on the exact information value. In the following description, stimulus parameters are expressed by the vector  $\alpha$  and a stochastic signal representing that stimulus is given by  $X_\alpha$ . Here  $X_\alpha$  is distributed according to  $p_\alpha$ , a probability function that depends on  $\alpha$ . A system takes as input a stochastic signal  $X_\alpha$  and produce a stochastic signal  $Y_\alpha$  (governed by a different probability law  $q_\alpha$ ) as output. In the case of the SFs,  $X_\alpha$  would be an EPSP input representing a stimulus with parameter  $\alpha$ , and  $Y_\alpha$  would be the corresponding spike train output. We would like to compare the amount of information about  $\alpha$  that can be extracted from the input and output signals.

A measure such as entropy cannot be used to quantify the information transfer capabilities of a system because it cannot quantify the amount of information a signal contains *with regard to a spe-*



**Figure 2.4** Crayfish SFs take analog EPSPs responding to a stimulus condition  $\alpha$  as input and produce spike responses representing  $\alpha$  as output. An information processing analysis compares the performance of an optimal classifier operating on the input signals  $(X_{\alpha_0}, X_{\alpha_1})$  to the performance of another optimal classifier operating on the output signals  $(Y_{\alpha_0}, Y_{\alpha_1})$ .

*cific stimulus feature.* The input signal  $X_\alpha$  may contain information about a stimulus feature other than  $\alpha$ , and that extraneous information may actually act as noise when trying to make a decision about  $\alpha$ . As a specific example, when trying to determine the light intensity from a sustaining fiber's output, information about the stimulus spatial frequency would be nuisance. Because information is “in the eye of the beholder” here, it is necessary to consider controlled *changes* in the value of  $\alpha$  and observe the *changes* in  $X_\alpha$  and  $Y_\alpha$ .

Given two different values of stimulus parameter  $\alpha$ , we desire a distance measure  $d(\cdot, \cdot)$  that quantifies the stimulus-induced change in the input signal  $d_X(\alpha_1, \alpha_0)$  and the output signal  $d_Y(\alpha_1, \alpha_0)$ . Ali-Silvey defined a class of distance measures [1] that satisfy the data processing inequality [4], which states that

$$d_X(\alpha_1, \alpha_0) \geq d_Y(\alpha_1, \alpha_0). \quad (2.1)$$

In other words, while systems can convert a signal from one form to another (which may be more desirable for a given application), no amount of processing can increase the signal's fidelity in representing  $\alpha$ . The data processing inequality is satisfied by all Ali-Silvey distances (by definition) and several other information theoretic distances not in the Ali-Silvey class.

We use one particular distance in the Ali-Silvey class known as the *Kullback-Leibler distance*

(also called relative entropy) [4],

$$KL_{\mathbf{X}}(\boldsymbol{\alpha}_1, \boldsymbol{\alpha}_0) = \int p_{\boldsymbol{\alpha}_1}(\mathbf{x}) \log_2 \frac{p_{\boldsymbol{\alpha}_1}(\mathbf{x})}{p_{\boldsymbol{\alpha}_0}(\mathbf{x})} d\mathbf{x}. \quad (2.2)$$

Again,  $p_{\boldsymbol{\alpha}}$  is the probability law governing  $\mathbf{X}_{\boldsymbol{\alpha}}$ .

It should be noted here that the term “distance” is somewhat misleading. Though the KL distance is always non-negative, it is not a true distance metric because it is not symmetric in general. However, this quantity is important because it obeys the data processing inequality given in (2.1), and because it has significant relations to statistical signal processing. In a Neyman-Pearson binary hypothesis testing problem, Stein’s Lemma [4] tells us that the probability of a false alarm error (under a constraint on the probability of a miss error) decays exponentially with a rate equal to the KL distance between the probability functions [14]:

$$P_f \sim 2^{-KL_{\mathbf{X}}(\boldsymbol{\alpha}_1, \boldsymbol{\alpha}_0)}.$$

The asymmetry of the KL distance can be difficult to deal with, and it is unnatural in the present study to define a “reference” stimulus  $\boldsymbol{\alpha}_0$ . For those reasons, we often use a symmetric extension to the KL distance known as the *resistor-averaged KL distance*, given by:

$$RKL_{\mathbf{X}}(\boldsymbol{\alpha}_1, \boldsymbol{\alpha}_0) = \frac{KL_{\mathbf{X}}(\boldsymbol{\alpha}_0, \boldsymbol{\alpha}_1)KL_{\mathbf{X}}(\boldsymbol{\alpha}_1, \boldsymbol{\alpha}_0)}{KL_{\mathbf{X}}(\boldsymbol{\alpha}_0, \boldsymbol{\alpha}_1) + KL_{\mathbf{X}}(\boldsymbol{\alpha}_1, \boldsymbol{\alpha}_0)}. \quad (2.4)$$

The resistor averaged KL distance also satisfies the data processing inequality (2.1) and is often a reasonable approximation to twice the Chernoff distance [15]. The Chernoff distance is important because it plays a similar role in defining the asymptotic decay rate for the total probability of error

for optimal classifiers [4],

$$P_e \sim 2^{-CH_{\mathbf{X}}(\alpha_0, \alpha_1)}.$$

The Chernoff distance is not used here because it is computationally demanding, involving the solution of an optimization problem. Unless stated otherwise, the resistor-averaged KL is used as the default distance measure in the following analysis.

Given a change in stimulus parameter  $\alpha$ , the ratio of the distance at the output to the distance at the input quantifies the amount of information about  $\alpha$  that was suppressed (or filtered) by the system. This ratio is termed the information transfer ratio, defined by

$$\gamma_{\mathbf{X}, \mathbf{Y}}(\alpha_0, \alpha_1) = \frac{RKL_{\mathbf{Y}}(\alpha_0, \alpha_1)}{RKL_{\mathbf{X}}(\alpha_0, \alpha_1)}. \quad (2.6)$$

A critical property of the information transfer ratio is its invariance to signal form at the input and output. The signals are characterized only through their respective probability functions under  $\alpha_0$  and  $\alpha_1$ , and only the distances between the input and output probability laws under each stimulus condition are ever used. The input and output signals are never directly compared and can therefore have a different structure (e.g., analog inputs and point process outputs). Also, it has been shown that many properties of the information transfer ratio do not depend on the choice of  $d(\cdot, \cdot)$ , as long as it is an Ali-Silvey distance [24].

From the data processing inequality given in (2.1) it follows that the information transfer ratio is always a quantity between zero and one. A value of one means there was perfect information transfer of the change in  $\alpha$  from input to output, and a value of zero means all information about  $\alpha$  was suppressed. The value of the information transfer ratio itself can be interpreted as the performance difference (i.e., the multiplicative difference in asymptotic error decay rates) between opti-

mal classifiers operating on the input and output signals. A complete description of this information processing theory (including basic system properties) can be found in [24].

## Chapter 3

### Data Preparation

#### 3.1 Intracellular Sustaining Fiber Recordings

The SF dendritic tree is large enough to allow intracellular recording with a microelectrode near the spike initiating zone. Intracellular recording yields a simultaneous composite record of both the EPSP input signal and spike train output. Recordings of the EPSP alone could be made using a spike inhibiting agent (such as TTX [20]) and extracellular recording could isolate the spike train output, but intracellular recording allows capturing both simultaneously.

Performing an information processing analysis of a SF for a given stimulus feature requires characterizing the probability laws governing both the input and output signals representing the stimuli. Because only a composite recording is available, we must separate the original composite recording into input and output components. The spike waveforms are stereotyped and modeled as a point process, so a record of the spike times entirely preserves the SF output. However, the EPSPs are analog signals and faithful detail preservation is desired.

Examining a sample response in figure 3.1, three distinct components are visible: action potential waveforms, a slowly-varying analog signal, and broadband membrane noise. The input EPSP consists of both the slowly-varying signal and broadband membrane noise. The spikes are relatively discontinuous in time and represent a wide-band signal in the frequency domain. Because the spike signal shares significant frequency bandwidth with the broadband membrane noise, a linear filter cannot adequately separate a spike train and an EPSP (shown clearly in [13, figure 1]).



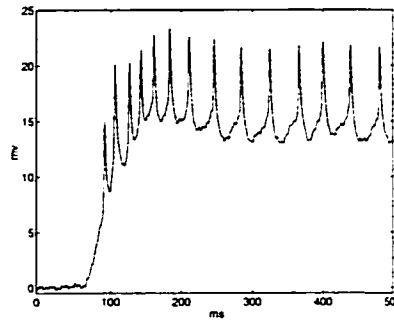


**Figure 3.1** *An example EPSP response is shown to a sudden-onset stimulus. Three different components are distinctly visible: spike waveforms, a slowly-varying signal, and broadband membrane noise. The membrane noise and the slowly varying signal are both part of the EPSP input, and spike waveforms constitute the SF output signal.*

### 3.2 Extension to Wavelet-Based Spike Separation Algorithm

A spike separation scheme based on wavelet denoising was presented in [13]. Traditional wavelet denoising is a nonlinear technique used to separate signals from broadband noise [2]. In a typical wavelet denoising application, a wavelet transform of the signal and noise combination is computed. The signal structure shows up as dominating wavelet coefficients at some scales of the decomposition, while noise power is distributed among all coefficients and scales. By eliminating coefficients below a threshold and computing the inverse transform, broadband noise is removed from the signal.

In the transform of a composite intracellular recording, spikes are discontinuities that persist as strong coefficients across scale but are localized in time. The wavelet decomposition scaling coefficients represent the lowest frequency content of the signal. The slowly-varying EPSP component is primarily low-frequency energy and it has been assumed that the EPSP is completely represented by the scaling coefficients. A threshold can be set (depending on the signal-to-noise ratio of the recording) that allows a spike signal to be extracted from a recording. The detail coefficients below threshold and all scaling coefficients are set to zero, eliminating energy from the slowly-varying EPSP and broadband noise. The inverse transform is computed with the remaining coefficients rep-

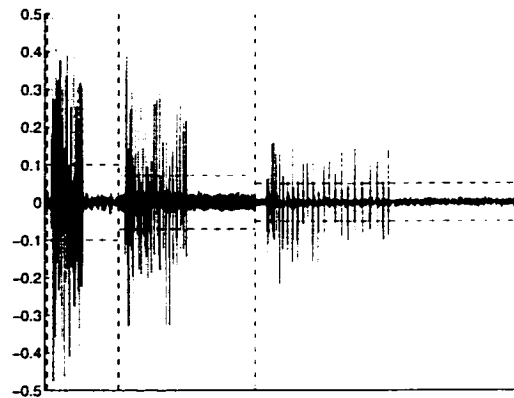


**Figure 3.2** Shown are a segment of coefficients from a discrete wavelet transform of an example SF intracellular recording. Only the three highest scales (finest detail coefficients) are shown, representing the highest frequency energy. The vertical dashed lines separate the three scales of coefficients. The action potentials are sharp discontinuities in time which persists strongly across each scale of coefficients. The lower energy, broadband membrane noise is also visible at all scales of coefficients, but is not localized in time. The slowly-varying EPSP signal has energy located primarily in the scaling coefficients, which are not shown here. The horizontal dashed line is the threshold (set based on the signal SNR) that can be used to separate the coefficients representing energy from action potentials from coefficients representing energy from the broadband membrane noise.

representing the spike signal. This denoising procedure has zero phase delay, so an extracted spike signal can be subtracted from the original recording to yield an estimated EPSP signal.

This method clearly extracts spike waveforms from the composite signal, and action potential event times are easily found by simple thresholding. However, little consideration has been given to faithfully preserving EPSP waveform detail. In particular, depending on the slowly-varying EPSP component, separated EPSPs can have significant deviations from the original recording even in areas where no spike events occurred. Some distortion in the separated EPSP could be tolerated in locations where spikes were removed from the original recording, but distortion in other areas is an unacceptable deviation from the true EPSP.

We developed an extension of this spike-separation algorithm that improves preservation of the EPSP signals. Our algorithm exactly preserves EPSP structure in areas where no spike events occurred. The spike separation method described above is based on the assumption that energy from the slowly-varying component of the EPSP is either completely contained in the scaling coefficients

of the wavelet transform, or contained in detail coefficients at a higher scale but below threshold. In a large set of intracellular recordings from crayfish SFs, this assumption was frequently violated. When significant energy from the slowly-varying potential is located in the detail coefficients, it is impossible to distinguish from energy contributed by spike events. EPSP energy above threshold in detail coefficients causes portions of the EPSP signal to be erroneously included in the separated spike signal. We need a method for extracting spike events that not only match a scale and energy profile, but are also localized in time. If spike event times are identified, the denoising procedure described above could be applied only where those events are known to occur. Denoising localized in time ensures the separated EPSPs exactly preserve the recorded signals in areas where no spikes occur.

Action potential waveforms are sharp increases in membrane potential, followed immediately by a sharp decrease. This signal's derivative would show a large positive slope on the rising phase of the spike and a large negative slope on the falling phase. Because of the discontinuity between the rising and falling phases, the second derivative of this signal has very negative values where spike peaks occur. By thresholding the signal's approximated second derivative, spike peaks are identified and precisely located. The approximated second derivative from an example SF recording is shown in figure 3.3.

A spike-removed signal is generated in the same spirit as the method outlined earlier. The wavelet transform of the entire original recording is computed and all detail coefficients above a threshold are eliminated. The inverse transform yields a signal (called the "smoothed" EPSP approximation here) with spike events completely removed and EPSP structure possibly partially removed. A separated EPSP is generated by merging the original recording with the smoothed EPSP approximation. Using identified spike peak locations, points can be found on either side of a spike

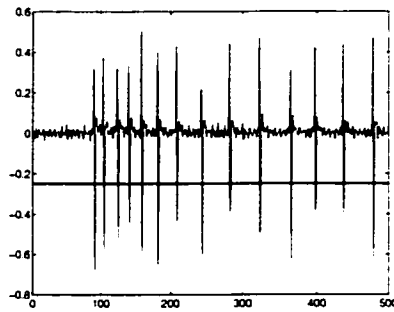


**Figure 3.3** Shown is the approximated second derivative for an example SF intracellular recording. Action potentials are sharp discontinuities in time, which will produce large negative deflections in the second derivative of the signal. A threshold can be easily applied to determine spike locations for use in the spike separation algorithm.

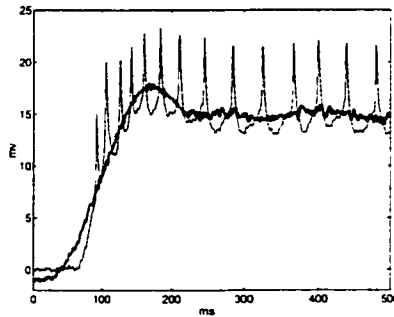


**Figure 3.4** Shown are an example SF recording (thin line) and the smoothed EPSP approximation (thick line) for this signal. The smoothed approximation was found by calculating the discrete wavelet transform of the recording, thresholding to remove coefficients representing spike energy and computing the inverse transform. The smoothed EPSP approximation removes the spike waveforms, but also can remove some of the EPSP signal when the slowly-varying signal has energy in the detail wavelet coefficients.

event where the original recording intersects the smoothed approximation. These points are used to define critical areas surrounding spike events. We separated the EPSP by using the original recording in areas away from spike events and using the smoothed approximation in these critical areas. Using intersect points as the merge boundaries minimizes discontinuity in the resulting separated EPSP signal. Because this operation is also zero-phase, the final separated spike signal is the difference of the separated EPSP signal and the original recording. The example SF recording and the resulting separated EPSP and spike waveforms are shown in figure 3.5.

Although this algorithm generates a separated EPSP that exactly preserves the original recording in areas away from spike events, distortion is clearly introduced where spikes have been removed.

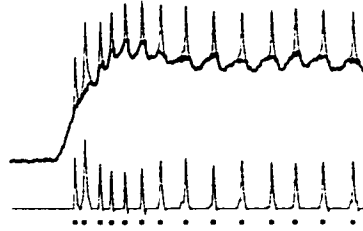


**Figure 3.5** Shown here are example results from the wavelet-based spike separation algorithm presented here. At the top of the figure, an example SF intracellular recording is shown as the thin line, and the separated EPSP signal is overlaid as the bold line. The separated EPSP signal is found by merging the smoothed EPSP approximation into the original recording in areas surrounding spike events. At the bottom of the figure, the resulting spike waveforms are shown with bold 'x' symbols indicating the event times. Only the bold elements in the figure are used for calculating the KL distance for the input and output responses.

The slowly-varying EPSP is sufficiently preserved, but little confidence can be given to the noise power or spectral character in these areas.

### 3.3 Electrical Noise (Hum) Removal

An information processing analysis using EPSPs must incorporate the membrane noise characteristics. Because the data recordings are made with electronic equipment, electrical noise (particularly 60 “hum” and its odd harmonics) can be introduced. We would like to ignore any measurement noise components unrelated to actual membrane activity. After a series of stimulus repetitions we separate the spike waveforms and EPSPs using the algorithm given in section 3.2, and calculate the mean EPSP signal by averaging the set of EPSP recordings. Before any further analysis is done, we attempt to remove hum that may be present in this mean EPSP signal.

Before the stimulus is applied, EPSP recordings contain only noise and no significant signal activity. A pre-stimulus segment of *membrane* noise is denoted by the vector  $C_{\alpha} \sim N(0, K_{\alpha})$ . The use of a Gaussian model and calculation of the covariance matrix  $K_{\alpha}$  is discussed in Chapter 4. Hum components will be denoted as sampled sinusoidal functions with known frequency but unknown phase,  $s(l, \phi) = \sin(2\pi 60l/F_s + \phi)$ , where  $F_s$  is the sampling rate. The recorded signal

vector  $\mathbf{R}_\alpha$  is the sum of the membrane noise and hum vectors:

$$\mathbf{R}_\alpha = \mathbf{C}_\alpha + A\mathbf{s}(\phi) \quad (3.1)$$

$$\mathbf{R}_\alpha \sim N(A\mathbf{s}(\phi), K_\alpha).$$

The probability function for this signal (conditioned on the unknown parameters) is

$$P_{\mathbf{R}_\alpha}(\mathbf{r}|A, \phi) = \frac{1}{\sqrt{|2\pi K_\alpha|}} \exp \frac{-\|\mathbf{r} - A\mathbf{s}(\phi)\|_{K_\alpha^{-1}}^2}{2}. \quad (3.2)$$

The maximum-likelihood estimates of  $\hat{A}$  and  $\hat{\phi}$  are found when equation (3.2) is maximized, which is the same as maximizing:

$$\max_{A, \phi} \left( -\|\mathbf{r} - A\mathbf{s}(\phi)\|_{K_\alpha^{-1}}^2 \right) = \max_{A, \phi} \left( 2A\langle \mathbf{r}, \mathbf{s}(\phi) \rangle_{K_\alpha^{-1}} - \|\mathbf{r}\|_{K_\alpha^{-1}}^2 - A^2\|\mathbf{s}(\phi)\|_{K_\alpha^{-1}}^2 \right). \quad (3.3)$$

The parameter  $\phi$  only has a significant effect on the term  $\langle \mathbf{r}, \mathbf{s} \rangle_{K_\alpha^{-1}}$  in equation (3.3). The maximum cross-correlation between the recording vector  $\mathbf{R}_\alpha$  and  $\mathbf{s}(0)$  (with a  $K_\alpha^{-1}$  kernel inner product) yields the maximum likelihood delay,  $\hat{\phi}$ . Equation (3.3) can also be differentiated with respect to  $A$  and set to zero to find the maximum likelihood amplitude:

$$\hat{A} = \frac{\langle \mathbf{r}, \mathbf{s}(\hat{\phi}) \rangle_{K_\alpha^{-1}}}{\|\mathbf{s}(\hat{\phi})\|_{K_\alpha^{-1}}^2}. \quad (3.4)$$

The maximum likelihood estimates  $\hat{A}$  and  $\hat{\phi}$  are used to remove hum from the entire mean EPSP recording vector. After removing 60 Hz hum, we also attempt to remove 180 Hz and 300 Hz harmonics in the same manner. There is significant 180 Hz and 300 Hz hum energy in some data

records, but no higher harmonics were significantly present. The power spectral density (PSD) of one example mean EPSP segment is shown in the left panel of figure 3.6. The PSD of the same signal with the hum removed is shown in the right panel. The hum removal algorithm removes most of noticeable electrical noise and does not cause damage to the neighboring spectrum the way a simple “notch filter” would.

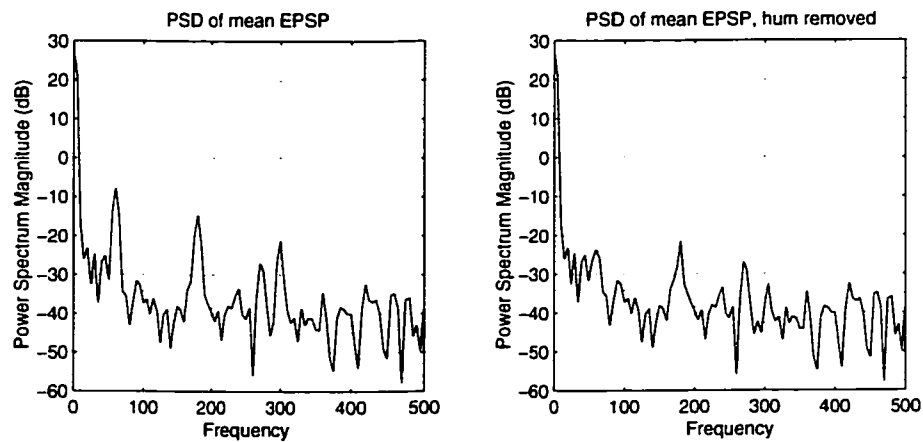


**Figure 3.6** Shown in the left panel is the power spectral density (PSD) of a mean EPSP segment. Peaks of energy at 60 Hz and its odd harmonics are evident, indicating the presence of electrical “hum”. The right panel shows the PSD of the signal after the hum removal algorithm has been applied. Most of the hum has been removed, and the neighboring spectrum is unchanged.

## Chapter 4

### Calculating Kullback-Leibler Distances

#### 4.1 Estimating Spike KL Distances

As described in section 2.1, SFs have spike train outputs typically modeled as point processes. An information processing analysis requires KL distance calculations between spike train probability laws under two different stimulus conditions. The most straight-forward KL distance estimate between true probability laws is the KL distance between probability law estimates. The spike train probability law does not have a known analytic form, so a non-parametric estimate is made. Johnson et al., outline a method in [12] for estimating KL distances using spike responses. During the experiment the stimulus is periodically repeated, yielding responses that are realizations of a cyclostationary [25] random process. Because the responses are stationary with a periodic offset, a type estimate can be formed for the probability of events occurring in a time bin. The type estimate of event probabilities in each bin is a post-stimulus time (PST) histogram [11] for a collection of spike responses to a periodically repeated stimulus.

In our notation, the vector  $\hat{q}_{\alpha_0} = (\hat{q}_{\alpha_0}(1), \hat{q}_{\alpha_0}(2), \dots, \hat{q}_{\alpha_0}(N))$  would represent type estimates for each of the  $N$  response bins under stimulus condition  $\alpha_0$ . If these bins are independent, the joint probability function is the product of all individual bin probabilities. With independent bins, the total KL distance between response vectors is the sum of KL distances at each bin:

$$d_Y(\alpha_0, \alpha_1) = \sum_{n=1}^N d_{Y(n)}(\alpha_0, \alpha_1). \quad (4.1)$$

Spike response KL distance estimation presents a few notable issues. First, with a small number



of responses, a bin in one type estimate can have no events while the same bin in the other type estimate (for the second stimulus condition) has at least one event. Non-overlapping support in a type estimate can be an artifact of the small dataset size and thus not representative of spike train probability laws. A support difference corresponds to an infinite KL distance, which is an undesirable artifact from estimation with small datasets. We correct for these artifacts by using a Krichevsky-Trofimov (K-T) modified type estimate [12]. The K-T modification adds  $\frac{1}{2}$  to each bin before normalization, yielding an asymptotically unbiased estimate with guaranteed support in every bin.

Another complication arises choosing the type estimate bin width. Larger bins will reduce time resolution in the type estimate. Smaller bins create more bins to fill with the same amount of data, resulting in less accurate estimates. The probability of events occurring in a bin changes with bin width, and therefore the KL *in each bin* also depends on bin width. However, the KL distance for the entire response vector (found by summing individual bin KLs) does *not* depend on the bin width [12] as the binwidth gets smaller (under Poisson assumptions). To reduce the appearance of bin-width affects in this analysis, we generally plot KLs cumulatively with increasing time rather than individual bin KLs.

The KL calculation procedure described above assumes that bins are statistically independent. An extension to this procedure includes Markov dependence between the bins [7, 12]. Any increase in the Markov order from  $D = 0$  (statistically independent bins) creates an exponential increase in the number of bins that need filling to create a probability function type estimate. The datasets available are not large enough for reliable estimates when Markov dependence is included ( $D > 0$ ), so the independent bin assumption ( $D = 0$ ) is necessarily used.

Spike response KL distances estimated using types can be considerably biased. Gruner and

Johnson [7, 12] employed the bootstrap procedure [5, 10] to estimate and remove bias from the spike response KL estimates. The bootstrap is a statistical resampling technique that estimates bias introduced by sampling from a population (i.e., collecting data). This procedure has worked well in simulation, producing more accurate estimates of known KL distances. The bootstrap also provides a means for calculating error bar around the spike KL estimates. Complete descriptions of spike train KL estimation are given in [7, 12].

## 4.2 Estimating EPSP KL Distances

The other component of our information processing analysis is a KL distance estimate between probability laws governing the analog EPSP inputs. Estimating a non-parametric probability function for analog signals requires a vast amount of data. Given the present constraints, we developed a parametric model describing EPSP signal characteristics. The compound EPSP input signal (measured near the integration region of the SF) is a sum of many individual EPSP events initiated in the dendritic tree. Because individual EPSPs are sudden onset signals (generated by presynaptic action potentials) with a relatively quick decay, the sum can be conceptualized as “shot noise” [22]. Asymptotically, the sum of many such individual EPSP “shots” is a Gaussian random process. Using statistical goodness-of-fit tests [3] we have found a Gaussian model is not an unrealistic fit for the EPSP data, and that model will be used here.

If two EPSP signals are characterized by  $\mathbf{X}_{\alpha_0} \sim N(\mathbf{m}_{\alpha_0}, K_{\alpha_0})$  and  $\mathbf{X}_{\alpha_1} \sim N(\mathbf{m}_{\alpha_1}, K_{\alpha_1})$ , the KL distance at the input is given by

$$KL_{\mathbf{X}}(\alpha_0, \alpha_1) = \frac{1}{2} \left( \ln \left( \frac{|K_{\alpha_1}|}{|K_{\alpha_0}|} \right) - N + \text{tr} [K_{\alpha_1}^{-1} K_{\alpha_0}] + (\mathbf{m}_{\alpha_1} - \mathbf{m}_{\alpha_0})^t K_{\alpha_1}^{-1} (\mathbf{m}_{\alpha_1} - \mathbf{m}_{\alpha_0}) \right), \quad (4.2)$$

where  $|K_{\alpha}|$  is the determinant of  $K_{\alpha}$  and  $\text{tr}[\cdot]$  is the trace of a matrix. If  $K_{\alpha_0} = K_{\alpha_1}$ , the first three terms of equation (4.2) are zero. If  $K_{\alpha_0} \neq K_{\alpha_1}$  the first three terms of equation (4.2) are always non-negative (KL distance non-negativity and substituting  $\mathbf{m}_{\alpha_0} = \mathbf{m}_{\alpha_1}$  into equation (4.2) yields this result). In the present analysis, only recordings from the same preparation and neural unit will be compared. Because the noise characteristics depend on individual SF membrane properties, correlation functions will be very similar for recordings from the same preparation and neural unit. Similar correlation structures and large SNRs make the first three terms of equation (4.2) insignificant ( $\sim .1\%$  of the total) compared to the final estimated KL distance. To reduce complexity in the KL estimate, only the most significant final term of equation (4.2) will be used as a lower bound (and reasonable estimate) of the true KL distance:

$$KL_X(\alpha_0, \alpha_1) \approx \frac{(\mathbf{m}_{\alpha_1} - \mathbf{m}_{\alpha_0})^t K_{\alpha_1}^{-1} (\mathbf{m}_{\alpha_1} - \mathbf{m}_{\alpha_0})}{2}. \quad (4.3)$$

Assuming a Gaussian random vector as the EPSP data model, two quantities are needed to estimate an input KL distance estimate for two stimuli: the mean vectors ( $\mathbf{m}_{\alpha_0}$  and  $\mathbf{m}_{\alpha_1}$ ) and covariance matrices ( $K_{\alpha_0}$  and  $K_{\alpha_1}$ ). As mentioned previously, each stimulus is repeated several times and SF recordings made. For each data record we separate EPSP and spike responses by applying the spike-separation procedure described in section 3.2. Because the responses are cyclostationary, we estimate the mean vector  $\mathbf{m}_{\alpha}$  for a stimulus condition by averaging EPSP responses.

Depending on the fundamental membrane noise structure, several techniques could be used to estimate the covariance matrix  $K_{\alpha}$  for a stimulus condition. Direct estimation of the sample covariance matrix is not desirable in this case because of the small dataset size (compared to the size of  $K_{\alpha}$ ). Spectral estimation techniques such as auto-regressive (AR) analysis (also called

linear predictive coding) [23] could be used to estimate the membrane noise correlation structure. Spectral estimation techniques are very sensitive and may require long segments of contiguous data, especially if that noise has a very “low-pass” character. Any additive noise from a source other than the neural membrane would significantly affect the results. The sensitivity of AR analysis presents a significant problem because “extraneous noise” can be introduced in both the measurement and spike separation stages. Because the measurements are made with electrical equipment, electrical noise (particularly 60 Hz “hum” and its odd harmonics) can be present. We attempt to remove hum from the mean EPSP signals using a technique described in section 3.3. No technique for hum removal is perfect however, and any remaining hum (or hum removal artifacts) can have significant negative impact on spectral estimation.

Even assuming that electrical hum could be adequately removed, noise introduced during spike separation is much more detrimental. The technique we use for separating EPSP and spike responses, described in section 3.2, produces noticeable artifacts where spikes were removed from the original recording. SFs discharge spontaneously in the absence of a stimulus, making it virtually impossible to find sufficiently long data records without artifacts from spike removal. Even if the resting membrane noise characteristics could be estimated, the noise characteristics are not guaranteed to be the same in active areas with significant EPSP and spike activity. Direct estimation of membrane noise correlation properties using established spectral estimation techniques is not possible given present constraints. To estimate EPSP KLs, we develop a model for membrane noise correlation based on membrane and synapse physiology.

#### 4.2.1 Neurophysiologic Model

The primary neural structures contributing to EPSP formation are functionally analogous to electrical components, leading naturally to neurophysiologic circuit models. Neural membrane electrical potential is created by an excess of charged ions (of equal and opposite charge) on opposite sides of the cell membrane. The membrane is a lipid, bilayer structure that is impermeable to ions, keeping extracellular and intracellular ions separated despite the mutual attraction. The membrane separates and stores ionic charge in the same way capacitors function with free electrons. Selective ion channels are embedded in the cell membrane, allowing passive ion movement. An ion channel ensemble has a conductance that may depend on the presence of electrical potential (*voltage-gated channels*) or specific chemical agents (*ligand-gated channels*). The resting membrane has a characteristic net conductance ( $G_{mem}$ ). An EPSP is created when an adjacent neuron releases a neurotransmitter that causes postsynaptic ligand-gated ion channels to open, increasing the synaptic conductance ( $G_{syn}$ ). The net membrane conductance is the sum of the synaptic and resting membrane conductances,  $G = G_{syn} + G_{mem}$ . The ion channel ensembles are modeled as a membrane resistor and a synaptic variable resistor in parallel with a capacitor. Conductance increases responsible for EPSP generation have been measured in crayfish SFs by Waldrop and Glantz [26]. Resting membrane conductances and membrane capacitances are provided from a biophysical model developed by Glantz [6]. The amount of ionic current into the cell depends on both the conductance and electrochemical potential specific to that ion. The net driving potential across the cell membrane is modeled as a voltage source. A more detailed neurophysiology introduction is in Appendix A and complete studies are found in [16, 20].

The composite circuit model for the *resting* membrane is a well-known RC low-pass filter shown in figure 4.1 with  $G_{syn}$  fixed. The circuit model has resistors and capacitors in parallel, and is clearly

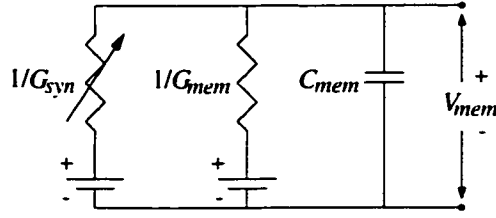


**Figure 4.1** The resting neural membrane is modeled as a RC circuit. The membrane itself is modeled as a capacitor with capacitance  $C$ , and the resting membrane conductance is modeled as a resistor with resistance  $1/G_{mem}$ . EPSPs are generated by an increase in the synaptic conductance  $G_{syn}$  (modeled as a variable resistor), triggered by the presence of neurotransmitters at the post-synaptic terminal. The net currents depend also on the net driving potential across the cell membrane, modeled as a voltage source.

a first order (i.e., single-pole) system. The single pole, RC lowpass-filter has a transfer function given by

$$H(s) = \frac{1/C}{s + 1/\tau}, \quad (4.4)$$

and an impulse response given by

$$h_c(t) = \frac{1}{C} e^{-t/\tau} u(t), \quad (4.5)$$

where  $R = 1/G$  (the total membrane resting conductance),  $\tau = RC$  and  $u(t)$  is the unit step function. A stationary RC circuit characterized by (4.4) captures resting membrane characteristics, but in the presence of membrane activity (EPSPs) a more complicated model is necessary. EPSP generation is due to increased synaptic conductance, causing an increase in the total membrane conductance. In the presence of time-varying EPSPs, the membrane conductance is also time-varying. A non-stationary RC circuit model with a time-varying resistance  $R_c(t)$  captures the time-varying nature of the membrane. Thus, the SF acts as a lowpass-filter with a *time-varying* pole at  $\frac{-1}{(R_c(t)C)}$ .

RC circuit models and the underlying neural processes are continuous-time systems. However, during data collection we sample the true membrane activity. All data processing and analysis

must be done in discrete-time. We need a method for converting the RC circuit model defined by neurophysiological characteristics to an approximately equivalent single-pole, discrete-time filter. There are several mappings from the  $s$ -plane to the  $z$ -plane that will serve this purpose. We use the *impulse invariance* method [21], ensuring the discrete-time unit sample response is a sampled version of the continuous-time impulse response. In this method, the  $s$ -plane is mapped to the  $z$ -plane by the equation

$$z = e^{(s/F_s)}, \quad (4.6)$$

where  $F_s$  is the sampling rate (1000 Hz presently). For the stationary RC circuit model described in equation (4.4), there is a pole in the  $s$ -plane at  $-1/\tau$ . This translates to a pole in the  $z$ -plane at  $a = e^{-(10^{-3}/\tau)}$ . The impulse-invariant discrete-time filter for the stationary RC circuit described in (4.4) has a unit sample response given by

$$h(n) = a^n u(n), \quad (4.7)$$

where  $u(n)$  is the discrete-time unit step function.

A sampled version of the time-varying resistance  $R(n)$  is determined using the EPSP value at time step  $n$  and the membrane resting conductance, according to the relationship measured in [26]. The  $s$ -plane moving pole  $\frac{-1}{R(n)C}$  can be mapped to a series of approximately equivalent  $z$ -plane pole locations  $a(n)$ . An example EPSP is shown in figure 4.2, along with the time-varying net membrane resistance  $R(n)$  and the corresponding pole location  $a(n)$ . The analogous non-stationary, discrete-time system is described by the difference equation

$$y(n) = a(n)y(n-1) + x(n). \quad (4.8)$$

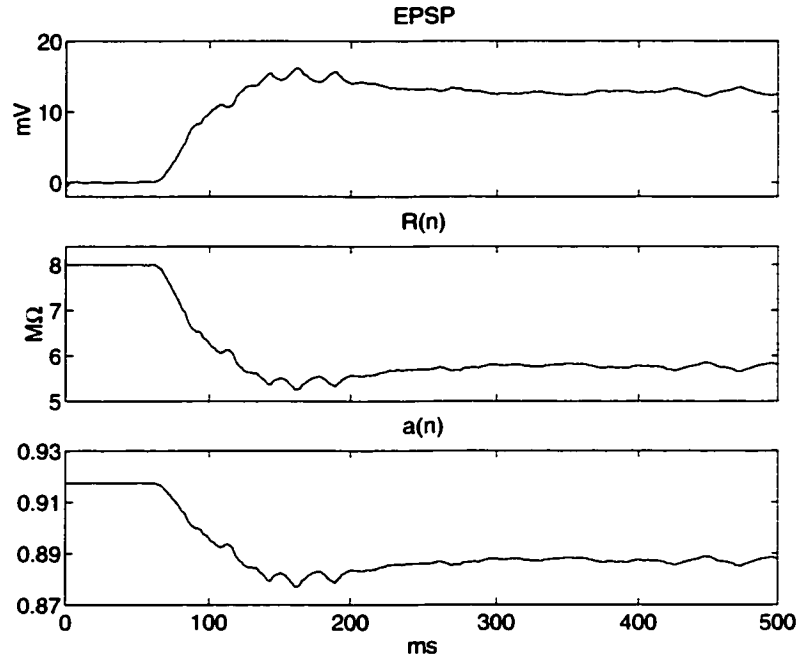


**Figure 4.2** Shown in the top panel is an example SF EPSP from a suddenly applied stimulus. The resting membrane has a resistance of  $1/G_{mem} = 8 \text{ M}\Omega$  in this example, and a capacitance of  $1.45 \text{ nF}$ . The time-varying resistance  $R(n)$  generating the EPSP is shown in the middle panel. The resulting time-varying pole location  $a(n)$  of the impulse-invariant equivalent discrete-time system is shown in the bottom panel.

The discrete-time system described by equation (4.8) has an impulse response given by

$$h(n, k) = \left( \prod_{l=k+1}^n a(l) u(n-k) \right) + \delta(n-k), \quad (4.9)$$

where  $h(n, k)$  is the response of the system at time step  $n$  to a unit sample at time step  $k$ ,  $\delta(k)$ .

It is important to note a notation convention here. The product operator used in equation (4.9) and throughout the remainder of this paper will be defined to be zero for any terms where the lower index exceeds the upper index,  $\prod_{l=\alpha}^{\beta} x(l) = 0, \alpha > \beta$ . The non-stationary system given in equation (4.9) is the basis for a SF membrane noise model used in estimating EPSP KLs.



### 4.2.2 Model-Based EPSP KL Calculation

To calculate a KL distance for EPSP inputs, the colored noise vector  $C_{\alpha}$  must be completely specified. Recall that  $C_{\alpha} \sim N(0, K_{\alpha})$ , and the covariance matrix  $K_{\alpha}$  is given by the correlation function

$$\Phi_{\alpha}(n, m) = E[C_{\alpha}(n)C_{\alpha}(m)]. \quad (4.10)$$

The colored noise vector  $C_{\alpha}$  can be thought of as white noise that has been passed through a single-pole lowpass filter, described in terms of the difference equation (4.8),

$$C_{\alpha}(n) = a(n)C_{\alpha}(n-1) + W_{\alpha}(n), \quad (4.11)$$

where  $W_{\alpha}(n) \sim N(0, \sigma_{\alpha}^2)$ .

If the system were stationary ( $a(n) = a$ ), the correlation function is straightforward to compute:

$$\Phi_{\alpha}(n, m) = E[C_{\alpha}(n)C_{\alpha}(m)] = \frac{(\sigma_{\alpha}^2)a^{|n-m|}}{1-a^2}.$$

In the non-stationary case, the noise vector must be written using the unit sample response given in equation (4.9),

$$C_{\alpha}(n) = \sum_{k=-\infty}^n h(n, k)W(k). \quad (4.12)$$

Equation (4.10) is much more complicated than the stationary case, but can be solved to give the

correlation function for a first-order, time-varying AR process:

$$\begin{aligned}\Phi_{\alpha}(n, m) &= \sigma_{\alpha}^2 \left[ \delta(m - n) + \left( \prod_{k=m+1}^n a(k) \right) + \left( \prod_{r=n+1}^m a(r) \right) \right. \\ &\quad \left. + \sum_{l=1}^{\infty} \left( \prod_{k=n-l+1}^n a(k) \prod_{r=n-l+1}^m a(r) \right) \right].\end{aligned}\quad (4.13)$$

This derivation is given in Appendix B.

Equation (4.13) may initially appear complex, but further examination reveals a computationally inexpensive algorithm for computing individual terms. Consider an arbitrary term that corresponds to an element on the diagonal of the covariance matrix  $K_{\alpha}$ :

$$\Phi_{\alpha}(n, n) = \sigma_{\alpha}^2 (1 + a^2(n) + a^2(n)a^2(n-1) + a^2(n)a^2(n-1)a^2(n-2) + \dots). \quad (4.14)$$

Given a term on the diagonal of  $K_{\alpha}$ , terms one step off the diagonal are given by:

$$\begin{aligned}\Phi_{\alpha}(n+1, n) &= \sigma_{\alpha}^2 (a(n+1) + a(n+1)a^2(n) + a(n+1)a^2(n)a^2(n-1) + \dots) \\ &= \Phi_{\alpha}(n, n)a(n+1).\end{aligned}\quad (4.15)$$

Given a term on the diagonal of  $K_{\alpha}$ , calculating the next term down the diagonal is also trivial:

$$\begin{aligned}\Phi_{\alpha}(n+1, n+1) &= \sigma_{\alpha}^2 (1 + a^2(n+1) + a^2(n+1)a^2(n) + a^2(n+1)a^2(n)a^2(n-1) + \dots) \\ &= \Phi_{\alpha}(n, n)a^2(n+1) + \sigma_{\alpha}^2.\end{aligned}\quad (4.16)$$

Terms two steps (or more) off the diagonal follow in a similar way:

$$\Phi_{\alpha}(n+2, n) = \Phi_{\alpha}(n, n+2) = \Phi_{\alpha}(n, n+1)a(n+2) = \Phi_{\alpha}(n, n)a(n+1)a(n+2).$$

Calculating  $\Phi_{\alpha}(n, n)$  from equation (4.14) requires computing a sum involving all previous values of  $a(m)$ ,  $m \leq n$ . This is a stable system, meaning that all poles will be inside the unit circle in the  $z$ -plane ( $a(n) < 1$  for all  $n$ ). For the present work, the poles are also all positive ( $a(n) > 0$ ). At some point in the infinite sum, the product of the square of these terms becomes negligible.  $\Phi_{\alpha}(n, n)$  can be expressed as the individual sum of  $M$  significant terms and the sum of the remaining terms ( $\Delta_M$ ):

$$\Phi_{\alpha}(n, n) = \sigma_{\alpha}^2 (1 + a^2(n) + \dots + a^2(n)a^2(n-1) \dots a^2(n-M+1) + \Delta_M).$$

The term  $\Delta_M$  can be approximated by a geometric sum involving  $\tilde{a} \approx \max_n a(n)$ . The pole location  $a(n)$  is monotonically increasing with resistance  $R$ . The maximum value of  $a(n)$  is easily found by using the resting membrane resistance  $R$ , which is the minimum value of  $R(n)$ . The approximation to  $\Delta_M$  is given by:

$$\alpha_M = \sum_{n=M+1}^{\infty} \tilde{a}^{2n} = \frac{\tilde{a}^{2M}}{1 - \tilde{a}^2}.$$

From the definition of  $\tilde{a}$ , we know that  $\alpha_M \geq \Delta_M$  for all  $M$ . Assuming that all poles are positive, it follows that the error term is bounded by

$$0 \leq \epsilon < \sigma_{\alpha}^2 \alpha_M.$$

With the present data,  $M$  can be chosen relatively low ( $\sim 40$ – $50$ ) to ensure that the error in calculating the first term  $\Phi(1, 1)$  is much less than 1% of the value.

This model leads to a simple algorithm for calculating EPSP KLs. Under each stimulus condition, the EPSP responses are averaged to find the mean signal  $\mathbf{m}_\alpha$ . The resting membrane conductance  $G_{mem}$  is used to find the resting membrane pole location, denoted  $\tilde{a}$ . From the point where the analysis is to begin, a previous resting segment is used to estimate the colored noise variance,  $\hat{\sigma}_{\alpha_c}^2$ . The resting membrane has a relatively stationary pole at  $\tilde{a}$ , so the white noise variance is related to the colored noise variance as  $\hat{\sigma}_\alpha^2 = \hat{\sigma}_{\alpha_c}^2 (1 - \tilde{a}^2)$ . The mean EPSP signal is used to calculate the values of  $R(n)$  using the membrane resting conductance,  $G_{mem}$ . The membrane capacitance  $C$  and the time-varying membrane resistance  $R(n)$  are used to find the time-varying pole location  $a(n)$  (using the impulse invariance method). The pole locations  $a(n)$ , along with  $\tilde{a}$  and  $\hat{\sigma}_\alpha^2$  are used to approximate the term in the first row and column of  $K_\alpha$ , given by  $\Phi(1, 1)$  in equation (4.14). For each successive time step of the analysis, the next row and column of  $K_\alpha$  are calculated according to the relations described in equations (4.15) and (4.16), using the existing values of  $K_\alpha$ . For each stimulus condition a mean vector  $\mathbf{m}_\alpha$  and covariance matrix  $K_\alpha$  are calculated in this manner and are used in the Gaussian EPSP model to calculate the KL distance as given in equation (4.2).

### 4.3 Stimulus Dependent Latency: Comparing KLs

Sections 4.2.2 and 4.1 describe algorithms for estimating KL distances given input EPSPs and spike train outputs for two stimulus conditions. It is informative to plot the KL distance as it accumulates with each time step, and the time-varying information transfer ratio (defined in equation (2.6)) is the ratio of the cumulative output KL and the cumulative input KL. These calculations quantify the performance of hypothetical optimal detectors trying to distinguish two stimulus conditions

using EPSP inputs and spike train outputs.

We would like the analysis to characterize SF system properties and not on experimental procedure. In particular, an issue arises in calculating input or output KLs when responses have latencies that depend on the stimulus. First, consider the SFs in the context of the entire experimental system during sudden-onset stimuli, illustrated with abstract signals in a block diagram in figure 4.3. When

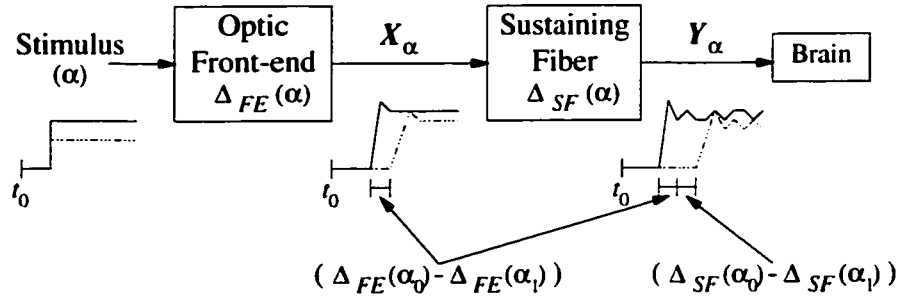


**Figure 4.3** Stimulus dependent delay in the crayfish visual pathway, illustrated with abstract signals in a block diagram. Signals passing through the optic front-end (the pre-SF pathway) incur some delay that may be stimulus dependent  $\Delta_{FE}(\alpha)$ . Signals will then propagate through the sustaining fiber stage and incur another (potentially stimulus dependent) delay  $\Delta_{SF}(\alpha)$ .

a light with intensity  $\alpha_0$  is applied at onset time  $t_0$ , the optic front end (including the photoreceptors through the medullary interneurons) passes the signal along with some delay  $\Delta_{FE}$ . After another delay  $\Delta_{SF}$ , the SF generates a spike train response representing the light stimulus. For the other stimulus condition, a light with intensity  $\alpha_1$  is switched on at  $t_0$  and the information propagates through the front-end and SF, also with some delays.

Problems arise when any of these delays are *stimulus dependent*,  $\Delta_{FE}(\alpha_0) \neq \Delta_{FE}(\alpha_1)$  and  $\Delta_{SF}(\alpha_0) \neq \Delta_{SF}(\alpha_1)$ . If  $\Delta_{FE}(\alpha)$  is stimulus-dependent but the EPSP signals are time-aligned according to  $t_0$ , a large KL distance may be induced by the latency difference. The KL distance is very sensitive to this situation, and even a small latency may introduce a very large distance. Fundamentally, aligning signals by  $t_0$  and not accounting for stimulus-dependent delay implies that these detectors have clairvoyant knowledge of  $t_0$ , a landmark used to compare relative timing

information. Ignoring stimulus-dependent delay in the analysis is unacceptable because giving the detectors any extra knowledge (e.g., the presence and location of  $t_0$ ) would be an artifact of the experimental procedure. We must consider the detection task as it would truly need to be performed: a detector would have to watch a channel for an *indefinite* amount of time, having no knowledge when a signal is supposed to appear (i.e., no knowledge of an absolute timing landmark). With respect to the latency difference between the signals, the detector would have to classify the signals in the worst case scenario, or minimum KL situation.

We must ensure that no extraneous clairvoyant information is passed to the hypothetical detectors, so we induce a latency difference between signals that produces the minimum KL between them. This is conceptualized by the block diagram of figure 4.4. In this diagram, we show the

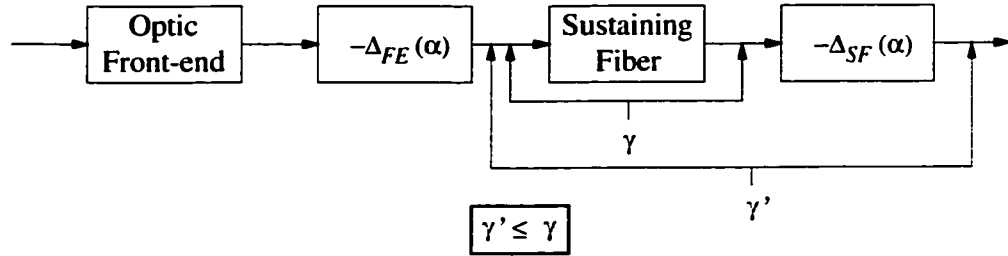


**Figure 4.4** Not accounting for stimulus dependent delay in the analysis would be analogous to providing the hypothetical detectors clairvoyant knowledge of an absolute timing landmark. We attempt to remove the affects of stimulus dependent delay in the analysis by conceptually inserting boxes that remove delay effects. With no timing knowledge the detectors would operate in the worst case scenario, corresponding to the latency shift that produces minimum KL. The affect of the delay correction can be included in the analysis. Because of the data processing inequality (2.1), the information transfer ratio measured with the delay boxes ( $\gamma'$ ) will be a lower bound for the true information transfer ratio ( $\gamma$ ).

insertion of boxes correcting for the stimulus dependent delay. The information processing theory applied here can account for such modifications in the analysis. We are interested in the true information transfer ratio of the SF ( $\gamma$ ), but with the stimulus dependent delay correction we are actually measuring  $\gamma'$ , a lower bound for  $\gamma$  because of the data processing inequality of equation (2.1). With the periodic sine-wave grating stimuli, the correction boxes will introduce phase shifts that result in

the minimum KL between signal sets. It is also important to note that individual responses from one stimulus condition are not shifted relative to each other. The whole set of responses to one stimulus condition are shifted relative to a set from another stimulus condition.

With sudden-onset stimuli, the analysis window containing the transient response does not represent a periodic stimulus, so simple phase shifts to minimize KL are not possible. We therefore approximate minimum KL by aligning responses based on the beginning of significant signal activity. The EPSPs show a noisy background followed by a distinct positive deflection during the transient response. For these signals, relative delay was determined by finding a linear fit to the sharp positive deflection and calculating a common zero-intersect point among the different stimuli conditions. The spike responses exhibit spontaneous activity and can therefore not be aligned by a simple landmark such as the first-spike. For spike responses, type-based detection is used to locate the start of a significant event in the data. Using the theory of types and Kullback-Leibler distances, Gutman [9] derived a detector that uses a sample of training data and has the smallest possible miss probability of *any* detector using training data (with a bound on the false alarm probability exponential decay rate). For spike responses, this is a null-hypothesis test where the hypothesis is the presence of a signal with unknown structure. Essentially we are looking for something which deviates from the background activity, and deviation is measured through KL distances. Training data is taken from the pre-stimulus spike response and a test data vector is formed by incrementally including the remaining spike response. For each stimulus condition, the first bin where the hypothesis is accepted determines the net stimulus dependent latency. This is similar to a method employed by Gruner and Johnson in [8].

## Chapter 5

### Data Analysis

We applied the EPSP and spike train KL estimation methods described in chapter 4 to data collected from crayfish SFs. The resistor-averaged KL (RKL) estimates are used to calculate the information transfer ratio for SFs responding to different stimulus features and over a range of stimulus values. We analyzed datasets from three separate preparations and neural units, representing different stimulus features. Two datasets are responses to sudden-onset stimuli with varying light intensity. The third dataset consists of responses to sine-wave grating stimuli with varying spatial frequency and orientation. Because they are from different preparations, these datasets are analyzed individually.

#### 5.1 Sudden-Onset Light Intensity Dataset 1 ( $LI_1$ )

The first light intensity dataset (denoted  $LI_1$ ) consists of responses to sudden-onset stimuli with log intensity values chosen from the set  $LI_1 = \{-3.5, -3.0, -2.5, -2.0, -1.5, -1.0\}$ , ordered from weakest to strongest. A single trial consists of a dark adapting period followed by a suddenly applied static stimulus covering the SF receptive field. In this preparation the membrane capacitance and resting conductance were determined to be 1.45 nF and  $1/(8.0 \text{ M}\Omega)$  respectively.

The mean EPSP signals elicited from these stimuli are shown in figure 5.1. The EPSPs exhibit a quick positive deflection at stimulus onset, with a magnitude and slope that increase with stimulus intensity. The EPSP transient lasts for a maximum of 150 ms, followed by a decay to a steady-state level that is relatively constant over the next 150 ms. The spike response Post-stimulus time (PST) histograms elicited from these stimuli are shown in figure 5.2. PST histograms are found



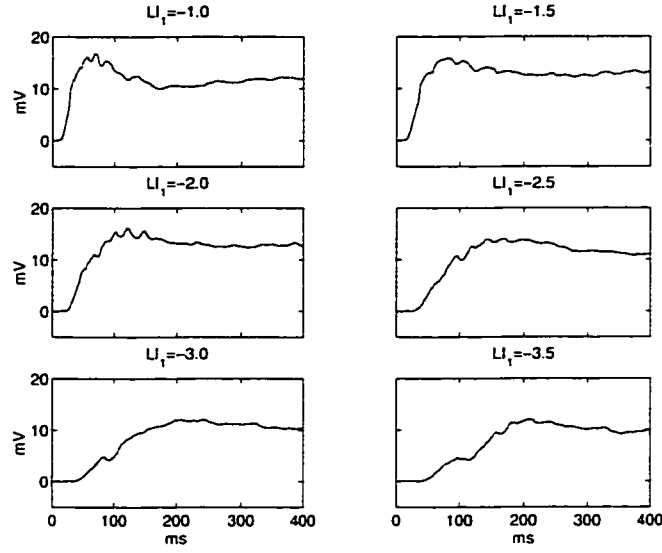


**Figure 5.1** Mean EPSP signals from sudden onset, light intensity dataset  $LI_1$ . Above each plot is the log intensity stimulus value producing the EPSP responses. Mean EPSPs are found by averaging responses from several stimulus repetitions. All sudden-onset stimuli produce a transient positive deflection followed by a decay to a sustained steady-state value. Stronger stimuli produce a larger deflection with a steeper slope.

by quantizing spike responses from several stimulus repetitions into bins and averaging the spike counts in each bin. The spike responses also exhibit transient and steady-state behavior. During the transient response, SFs produce a burst of spikes with maximum rates near 100 Hz for the strongest stimuli. Firing rates drop to a relatively constant nominal level of 15–20 Hz during the initial steady-state response.

Stimulus dependent delay is obviously present in both the EPSP and spike responses. We estimate stimulus-dependent delay with methods described in section 4.3, and align signals by initial significant activity. In the PST histograms shown in figure 5.2, the ‘x’ indicates the beginning of significant activity determined by a type-based detector [9]. The spike responses under different stimulus conditions are aligned by this landmark to estimate spike KLs. The EPSPs are aligned under different stimulus conditions by the common zero-intersect of linear fits to the transient deflections, and the aligned mean EPSPs are shown in figure 5.3. We also use these EPSP and spike train timing landmarks to compare input and output cumulative KL distances and calculate time-

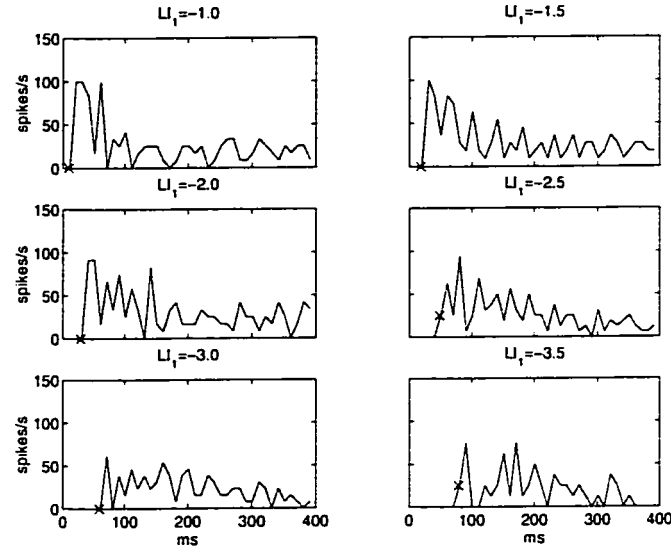


**Figure 5.2** Post-stimulus time (PST) histograms from light intensity dataset  $LI_1$ . Above each plot is the log intensity stimulus value producing the spike responses. PST histograms are found by quantizing spike responses from several stimulus repetitions into bins and averaging the spike counts in each bin. The PST histograms shown here are also normalized by binwidth to estimate the time-varying spike discharge rate [11]. The spike responses to sudden-onset stimuli also exhibit a transient burst of high-rate firing followed by a decay to a sustained steady-state discharge rate. The 'x' marks indicate the beginning of significant signal activity, found by a type-based null-hypothesis test. These marks are used to remove the stimulus dependent delay in spike responses.

varying information transfer ratios.

Cumulative KLs are estimated using input and output responses for all possible pairs of stimuli conditions in the dataset  $LI_1$ . Because we use the resistor averaged KL distance described in section 2.4, the distances are symmetric for each pair of stimuli values. Figure 5.4 shows the cumulative input EPSP KL distances for all possible pairs of stimuli. In this figure the outer axes denote stimuli values and each inner axes contain the cumulative EPSP KL distance for a stimuli pair. The resistor averaged distance has units of bits and the vertical scale on the plots of figure 5.4 is  $RKL/10^4$ . The total EPSP KL distances accumulated over the entire analysis segment are also plotted for each stimuli pair in figure 5.5. There are a few general trends worth noting. As expected, stimuli pairs that are farther apart in intensity (signified by plots more toward the lower left corner of figure 5.4, or the top of figure 5.5) tend to produce responses that have a larger total EPSP KL distance than do pairs

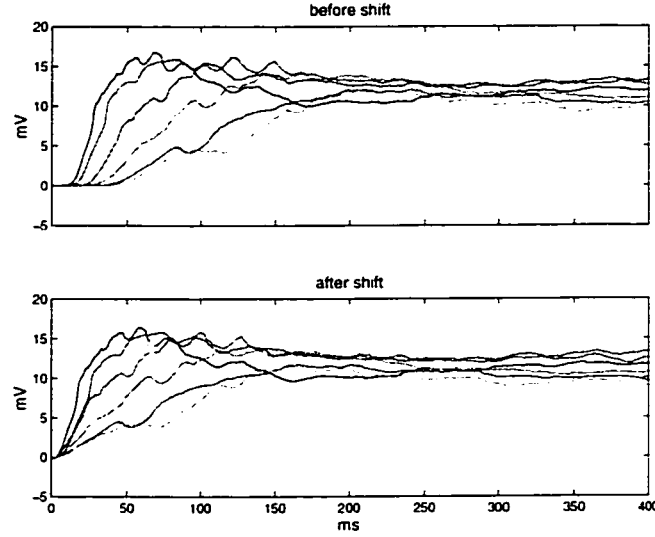


**Figure 5.3** The top plot shows an overlay of mean EPSPs for all stimuli values in the sudden-onset light intensity dataset  $LI_1$ . The bottom plot shows the mean EPSP responses with the estimated stimulus-dependent delay removed. The stimulus-dependent delay is estimated by using a linear fit to the transient deflection for each mean EPSP and calculating a common zero-intersect point.

that are closer together. Cumulative EPSP KLs also generally show two distinct time segments: a large KL accumulation rate during the transient response and a smaller KL accumulation rate over the steady-state response. The difference in KL accumulation rates is observed in the large slope of the cumulative KL plot during the first  $\sim 100$  ms, followed by a much smaller slope during the remaining response. For example, the stimulus pair  $\{\alpha_0 = -1.0, \alpha_1 = -3.5\}$  shows a large EPSP KL accumulation rate of roughly  $5 \times 10^4$  bits / 100 ms =  $5 \times 10^5$  bits/s during the transient response and  $1 \times 10^4$  bits / 250 ms =  $4 \times 10^4$  bits/s during the remaining response. The EPSP KL accumulation rates are over an order of magnitude different during the transient and steady-state time segments in this example.

Similarly, output (spike train) cumulative KL distances for all possible stimuli pairs are shown in figure 5.6. Error bars (90<sup>th</sup> percentile) are also shown for the cumulative spike KLs. The error bars are generated by applying the bootstrap procedure [5, 10] to spike KL estimation, described in [7, 12]. The total spike KL distances accumulated over the entire response segment are also plotted

for each stimuli pair in figure 5.7. The cumulative spike KLs show some of the same general trends that appeared in EPSP cumulative KLs. Generally the stimuli pairs that are farther apart in intensity show larger total KL distances than stimuli pairs that are closer together. Cumulative spike KLs also tend to show roughly the same transient and steady-state behavior as cumulative EPSP KLs. The difference immediately evident is the scale: the spike KLs are four orders of magnitude smaller than the EPSP KLs. The  $\{\alpha_0 = -1.0, \alpha_1 = -3.5\}$  stimulus pair shows spike KL accumulation rates of roughly 5 bits / 100 ms = 50 bits/s during the transient response and 1 bit / 250ms = 4 bits/s during the remaining response. As with the EPSP response, the difference between the transient and steady-state spike KL accumulation rates is roughly one order of magnitude. However, the spike KL accumulation rates are again four orders of magnitude smaller than the EPSP KL accumulation rates.

The time-varying information transfer ratios (the ratio of spike train and EPSP cumulative KLs) for all possible stimuli pairs are shown in figure 5.8. Error bars are plotted using the EPSP KL estimate and the spike KL estimate error bars. We cannot directly calculate error bars for the EPSP KL estimates (and consequently for the information transfer ratio estimates) because of the estimator complexity. The bootstrap procedure is only applicable for certain classes of estimators [5, 10], and it cannot be applied to the EPSP KL estimates to produce error bars. The error bars shown are therefore really a lower limit for the true error bar width. The information transfer ratio is a unit-less quantity and the vertical scale of the plots is  $\gamma/10^{-4}$ . The most significant time-varying trend in the information transfer ratio is the tendency to peak sharply during the transient responses and decay to a relatively constant value. The information transfer ratio peaks are more pronounced for *small* changes in the stimulus value, and the peaks can be nearly an order of magnitude greater than the steady-state values. The steady-state information transfer ratios for each stimuli pair are

also plotted in figure 5.9. The steady-state information transfer ratio values for the different stimuli pairs vary little, with all of the stimuli pairs yielding a final value in the range  $(.6-2) \times 10^{-4}$ . The steady-state information transfer ratio values may exhibit slightly larger values for smaller stimuli changes, though this trend is not clear considering the confidence intervals for the estimates.

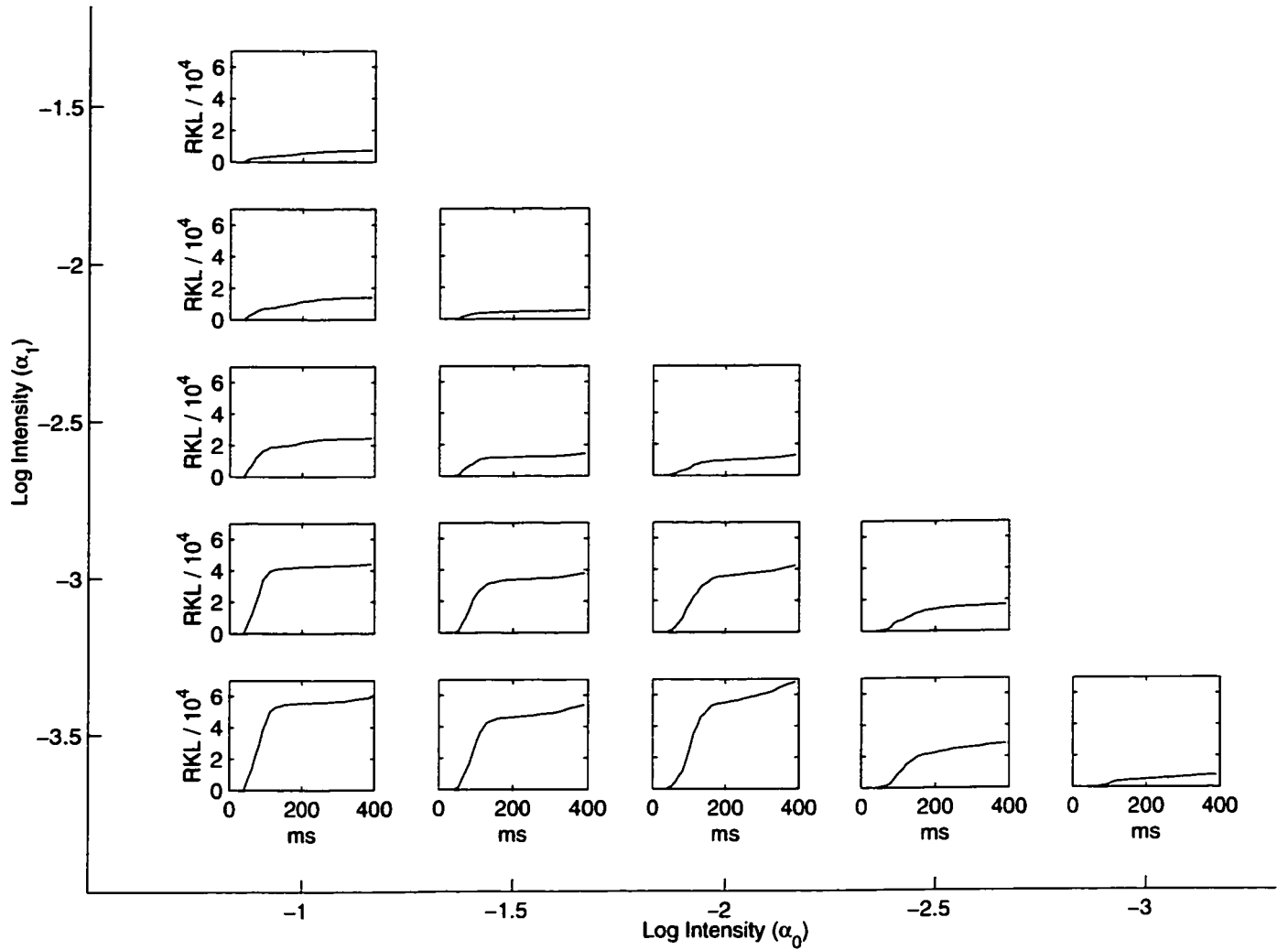


**Figure 5.4** SF input (EPSP) cumulative KL distances for all stimuli pairs from sudden-onset, light intensity dataset  $LI_1$ . The outer axes denote the stimuli values that elicited the responses ( $\alpha_0$  and  $\alpha_1$ ). The inner axes show the cumulative EPSP KL distance for a particular stimuli pair. The y-axis of the inner plots is resistor averaged KL distance /  $10^4$  (units of bits). The EPSP KL distances generally show two distinct segments. This first segment consists of a very large accumulation of KL distance during the transient EPSP response, indicated by a steep jump (large positive slope) in the cumulative KL plot. The second segment shows a marked decrease in the KL accumulation rate (smaller positive slope) during the steady-state response.

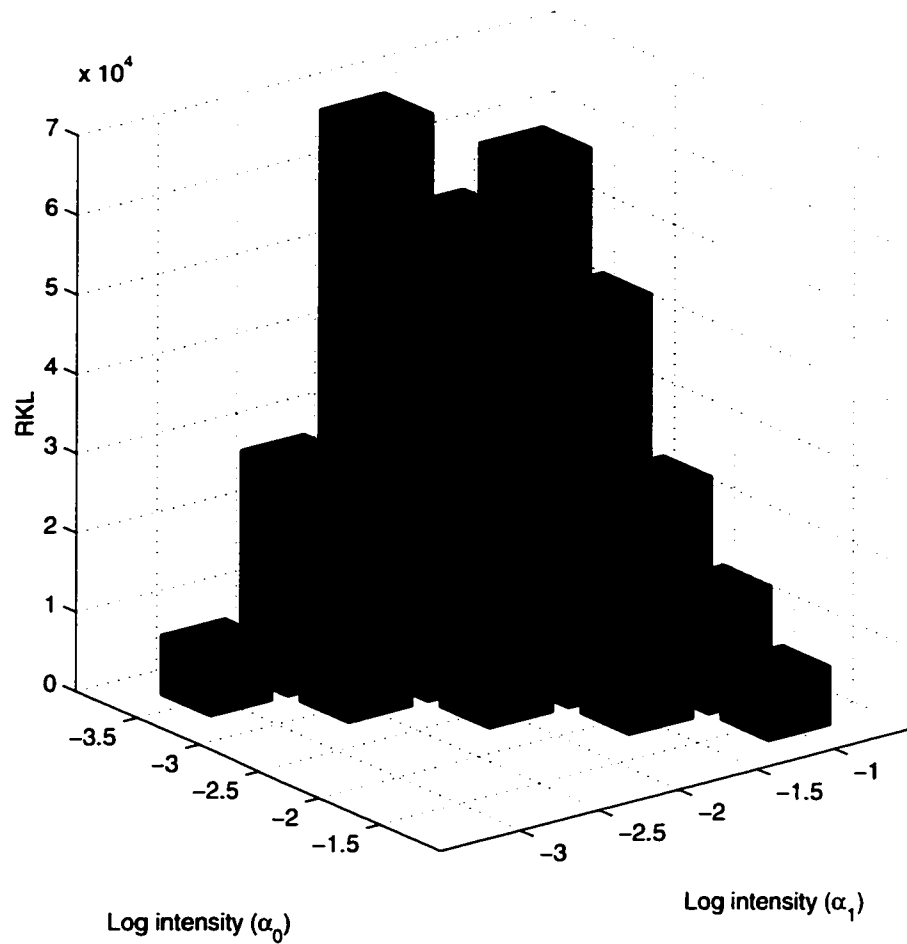


**Figure 5.5** SF KL distances calculated for the total EPSP response. The axes denote the stimuli values that elicited the responses ( $\alpha_0$  and  $\alpha_1$ ). The height of the bar is the total KL distance accumulated over the analysis segment, and is the final value of the cumulative spike response KL plotted in figure 5.4. Generally, larger stimuli differences produce larger EPSP KLs.

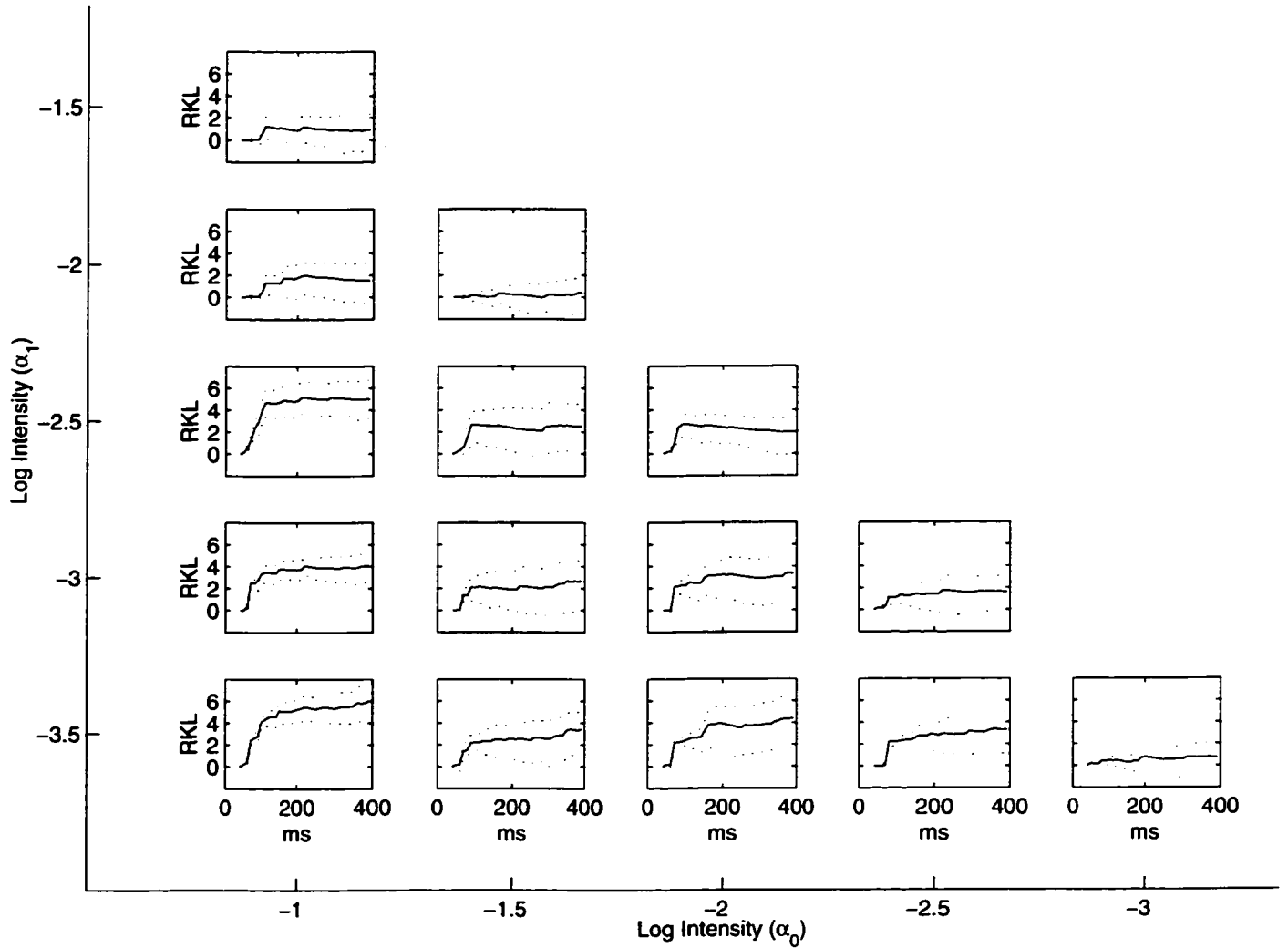


**Figure 5.6** SF output (spike) cumulative KL distances for all stimuli pairs from sudden-onset, light intensity dataset  $LI_1$ . The outer axes denote the stimuli values that elicited the responses ( $\alpha_0$  and  $\alpha_1$ ). The inner axes show the cumulative spike KL distance for a particular stimuli pair. The y-axis of the inner plots is resistor averaged KL distance (units of bits). Notice that this axis is four orders of magnitude smaller than the EPSP cumulative KL plots shown in figure 5.4. Error bars (90<sup>th</sup> percentile) estimated using the bootstrap procedure are also shown as dotted lines. The spike KL distances generally show the same two distinct segments as in the EPSP KL distance plots. This first segment consists of a very large increase in cumulative KL distance during the transient spike response, indicated by a steep jump (large positive slope) in the cumulative KL plot. The second segment shows a marked decrease in the KL accumulation rate (smaller positive slope) during the steady-state response.



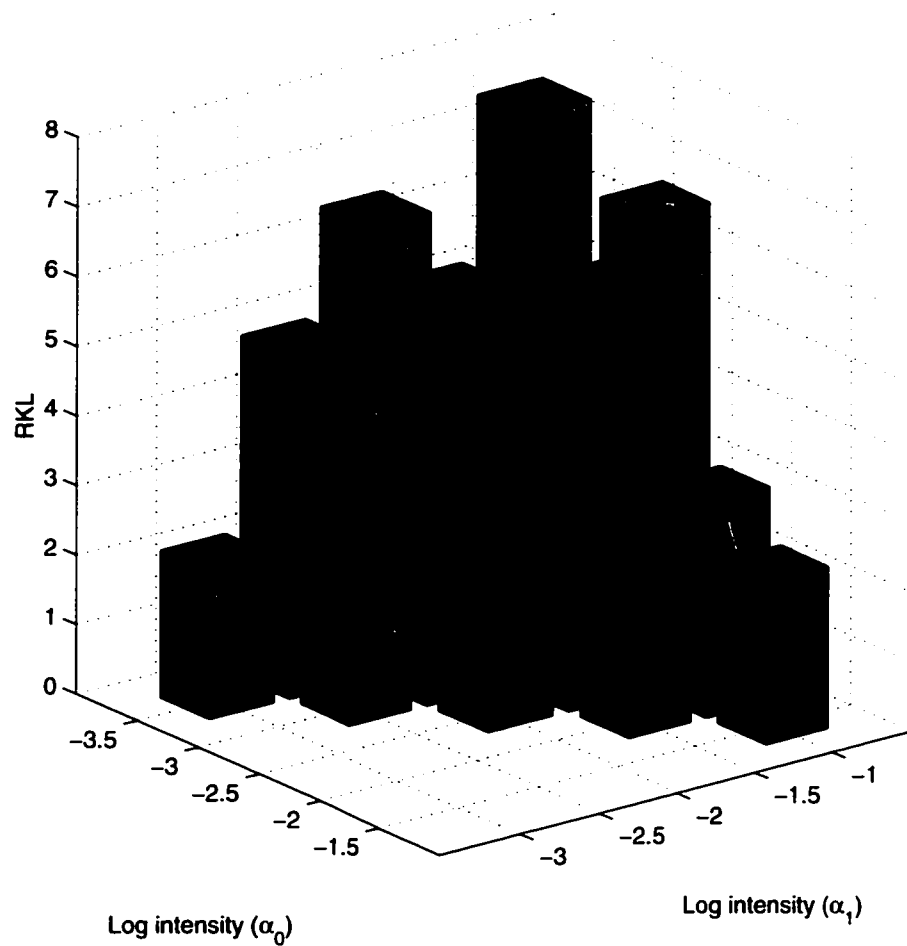


**Figure 5.7** SF KL distances calculated for the total spike response. The axes denote the stimuli values that elicited the responses ( $\alpha_0$  and  $\alpha_1$ ). The two light segments of each bar represent the upper and lower confidence intervals, with the separating line indicating the estimated total KL distance accumulated over the analysis segment (the final value of the cumulative EPSP KL plotted in figure 5.6). Generally, larger stimuli differences produce larger spike response KLs.

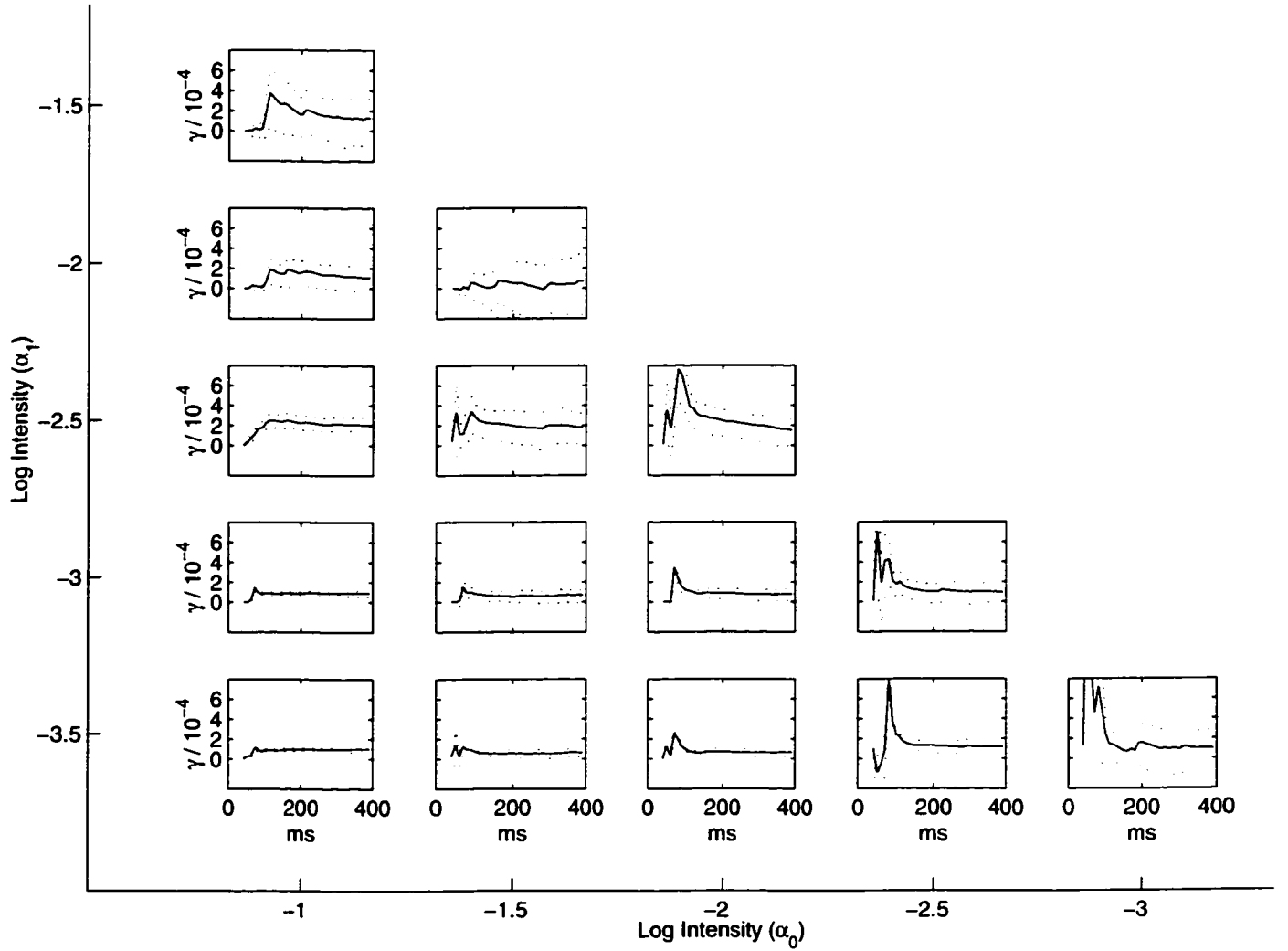


**Figure 5.8** SF time-varying information transfer ratios for all stimuli pairs from sudden-onset, light intensity dataset  $LI_1$ . The outer axes denote the stimuli values that elicited the responses ( $\alpha_0$  and  $\alpha_1$ ). The inner axes show the information transfer ratio for a particular stimuli pair as a function of time. The y-axis of the inner plots is information transfer ratio /  $10^{-4}$  ( $\gamma/10^{-4}$ ), and is unit-less. The steady-state information transfer ratio is relatively invariant to the size of the stimulus change. The time-varying information transfer ratios generally show a peak during the transient response and a decay to a relatively constant steady-state value. The largest transient peaks occur for small stimulus changes.

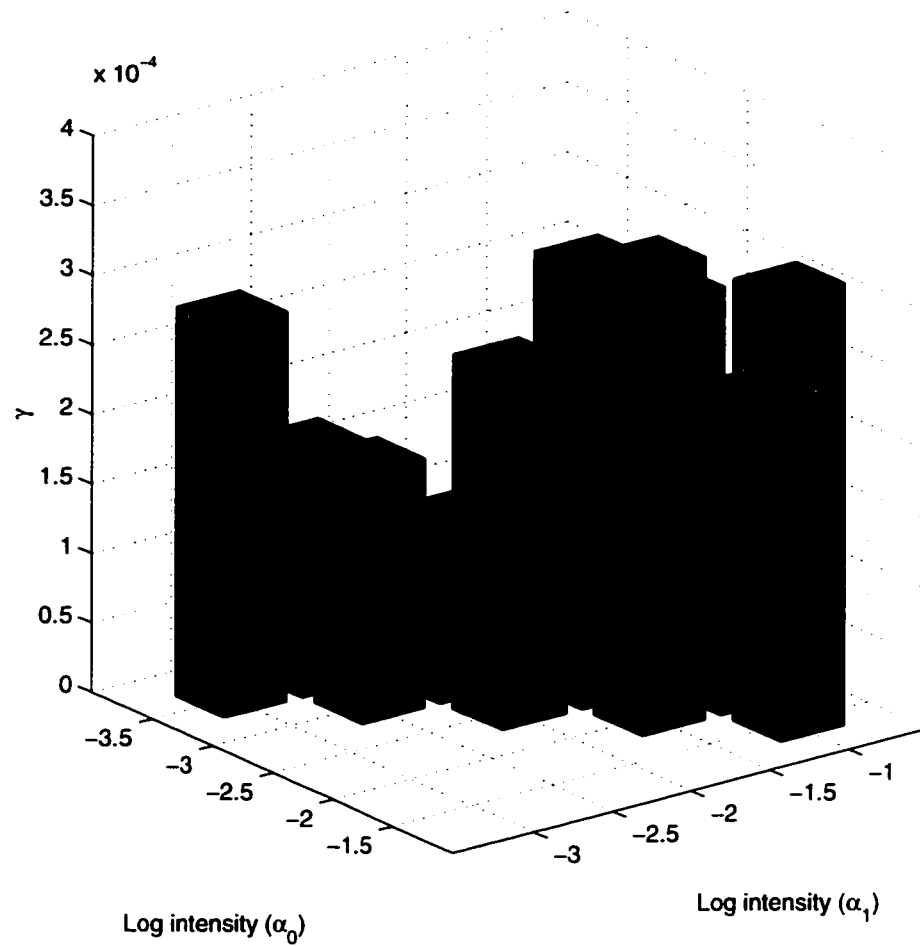


**Figure 5.9** Steady-state SF information transfer ratios for sudden-onset, light intensity dataset  $LI_1$ . The axes denote the stimuli values that elicited the responses ( $\alpha_0$  and  $\alpha_1$ ). The two light segments of each bar represent the upper and lower confidence intervals, with the separating line indicating the steady-state information transfer ratio for each stimuli pair (the final value of the cumulative EPSP KL plotted in figure 5.8).

## 5.2 Sudden-Onset Light Intensity Dataset 2 ( $LI_2$ )

The second light intensity dataset (denoted  $LI_2$ ) consists of responses to sudden-onset stimuli with log intensity values chosen from the set  $LI_2 = \{-3.7, -3.5, -3.0, -2.5, -2.0, -0.5\}$ , ordered from weakest to strongest. The experimental details are essentially the same as the first light intensity dataset ( $LI_1$ ), with a single trial consisting of a dark adapting period followed by a suddenly applied static stimulus covering the SF receptive field. A different preparation is used here than was used in the  $LI_1$  dataset, and the membrane capacitance and resting conductance for this unit was determined to be 8.12 nF and  $1/(4.8 \text{ M}\Omega)$  respectively.

The mean EPSP signals elicited from these stimuli are shown in figure 5.10. The same transient

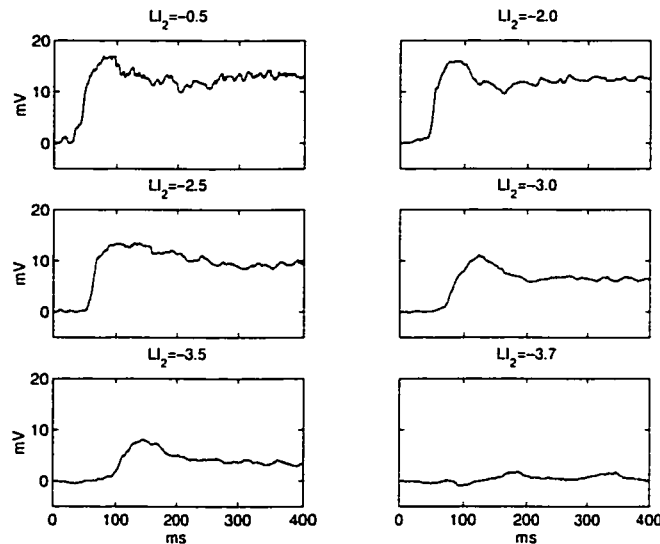


**Figure 5.10** Mean EPSP signals from sudden onset, light intensity dataset  $LI_2$ . Above each plot is the log intensity stimulus value producing the EPSP responses. Mean EPSPs are found by averaging responses from several stimulus repetitions.

and steady-state behavior seen in the EPSPs from dataset  $LI_1$  is also observed here. The most significant difference between the sudden-onset light intensity datasets is the noticeably smaller signal-to-noise ratio (SNR) in the data from  $LI_2$ . The noise power in the  $LI_2$  is noticeably higher than in the  $LI_1$  data, and the weaker stimuli in  $LI_2$  exhibit lower sustained values during the steady-

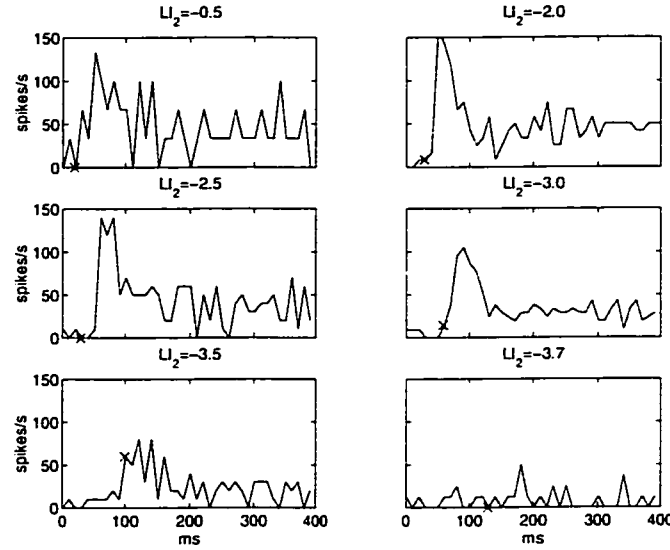


**Figure 5.11** *Post-stimulus time (PST) histograms from light intensity dataset  $LI_2$ . Above each plot is the log intensity stimulus value producing the spike responses. PST histograms are found by quantizing spike responses from several stimulus repetitions into bins and averaging the spike counts in each bin. The PSTs shown here are also normalized by the binwidth to estimate the time-varying spike discharge rate [11]. The 'x' marks indicate the beginning of significant signal activity, found by a type-based null-hypothesis test.*

state response. Because the datasets were collected from different preparations, the membrane characteristics (and consequently the SNRs) can vary substantially. It appears that the weakest stimuli ( $LI_2 = -3.7$ ) is at or below threshold for generating significant SF input above the noise background.

The spike response PST histograms elicited from these stimuli are shown in figure 5.11. These spike responses also generally exhibit the same transient and steady-state behavior seen in the  $LI_1$  spike responses, but with overall higher discharge rates. As with the EPSP responses, it appears that the weakest stimuli ( $LI_2 = -3.7$ ) is at or below threshold for eliciting a SF response.

Stimulus-dependent delay is estimated and removed using the same methods described for dataset  $LI_1$ . In the PST histograms (figure 5.11), the 'x' marks again indicate the beginning of significant activity determined by a type-based detector. The EPSPs are aligned by the zero-intersect of a linear fit to the transient deflection, and the aligned signals are shown in figure 5.12. Cumulative

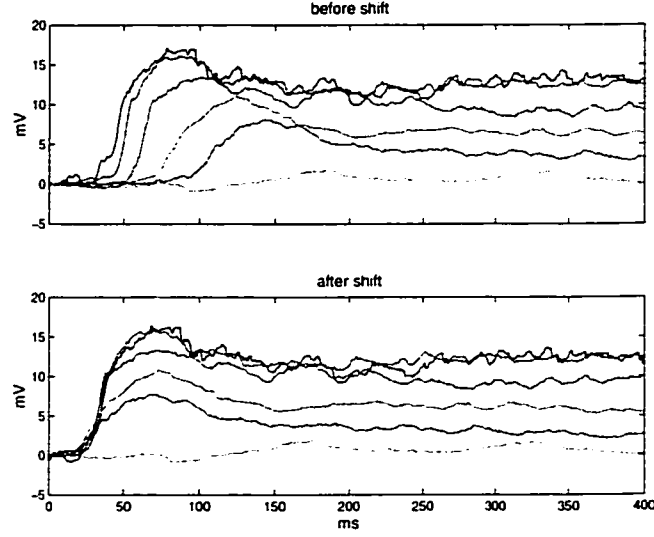


**Figure 5.12** The top plot shows an overlay of mean EPSPs for all stimuli values in the sudden-onset light intensity dataset  $LI_2$ . The bottom plot shows the mean EPSP responses with the estimated stimulus-dependent delay removed. The stimulus-dependent delay is estimated by using a linear fit to the transient deflection for each mean EPSP and calculating a common zero-intersect point.

EPSP KLs are estimated using input and output responses for all possible pairs of stimuli conditions in the set  $LI_2$ , and the resulting estimates are plotted in figure 5.13. In this figure the outer axes again denote stimuli values (from the set  $LI_2$ ) and each inner axes contains the cumulative EPSP KL distance for a stimuli pair. It is important to note that in this dataset, the stimuli intensity values in the set  $LI_2$  are *not* equally spaced. The spacing between the inner plots does not reflect the distance between the stimuli intensity values and the outer axes must be read to interpret the stimulus changes. The resistor averaged distance has units of bits and the vertical scale is  $RKL/10^2$ . The total EPSP KL distances accumulated over the analysis segment are also plotted for each stimuli pair in figure 5.14. The same general trends noted for dataset  $LI_1$  are also observed here, though much less pronounced. Stimuli pairs that are farther apart again tend to produce a larger total EPSP KL distance than pairs that are closer together. The cumulative EPSP KLs also generally show a larger KL accumulation rate during the transient response than in the steady-state response. In one example stimuli pair for this dataset,  $\{\alpha_0 = -2.0, \alpha_1 = -3.5\}$ , we observe an accumulation rate

of roughly  $8 \times 10^2$  bits / 50ms =  $1.6 \times 10^4$  bits/s during the transient response and  $5 \times 10^2$  bits / 125ms =  $4 \times 10^3$  bits/s during the remaining response. The significantly lower SNR for the  $LI_2$  dataset causes both the KL accumulation rates to be two orders of magnitude smaller than those of  $LI_1$ . The difference between transient and steady-state segments in this example is approximately a factor of four, but in the  $LI_1$  example there was a full order of magnitude distinction. The example stimuli pair used here is one of the more dramatic cases, and even less distinction is visible with many other stimuli pairs.

Output (spike train) cumulative KLs for all possible stimuli pairs are shown in figure 5.15. The total EPSP KL distances accumulated over the analysis segment are also plotted for each stimuli pair in figure 5.16. The spike KLs also show less pronounced versions of the same trends observed in dataset  $LI_1$ . Stimuli pairs that are farther apart generally show larger total KL distances than stimuli pairs that are closer together. Differences in transient and steady-state KL accumulation rates are also observable in some stimuli pairs, with the  $\{\alpha_0 = -2.0, \alpha_1 = -3.5\}$  pair showing KL accumulation rates of roughly 1.8 bits / 50ms = 36 bits/s and .4 bits / 125ms = 3.2 bits/s, respectively.

The time-varying information transfer ratios for all possible stimuli pairs are shown in figure 5.17. The information transfer ratio is a unit-less quantity and the vertical scale of the plots is  $\gamma/10^{-2}$ . The steady-state information transfer ratios for each stimuli pair are also plotted in figure 5.18. The steady-state information transfer ratios for this dataset are larger than those estimated for dataset  $LI_1$ . Examining the EPSP and spike KL distances, the spike KLs are in the same range as in  $LI_1$ , but the EPSP KLs are roughly two orders of magnitude smaller because of the difference in SNR. All stimuli pairs involving stimulus log intensity  $LI_2 = -3.7$  have higher than average spike KL distances. The spontaneous SF discharging to this threshold response is highly differentiable

from the responses to above-threshold stimuli. Consequently, the information transfer ratios involving the  $LI_2 = -3.7$  stimulus are abnormally high. If responses to  $LI_2 = -3.7$  are not considered, the steady-state values of the information transfer ratio are relatively constant and are almost all in the range  $(1.7-5) \times 10^{-3}$ . The time-varying information transfer ratios for this dataset again show the tendency to peak sharply during the transient portion of the responses and decay to a relatively constant value. The information transfer ratio peaks are again more pronounced for *small* changes in the stimulus value.



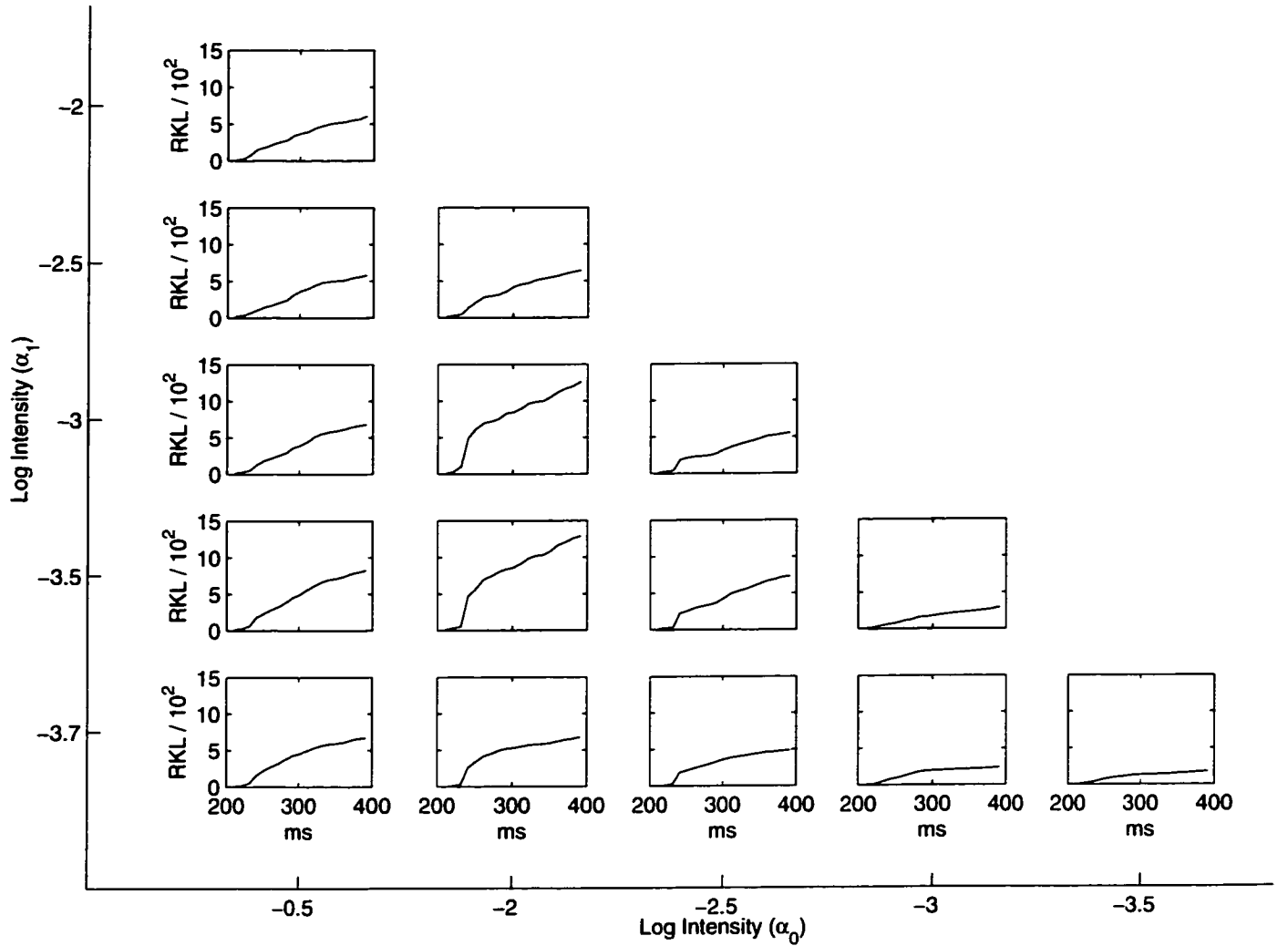


**Figure 5.13** SF input (EPSP) cumulative KL distances for all stimuli pairs from sudden-onset, light intensity dataset  $LI_2$ . The outer axes denote the stimuli values that elicited the responses ( $\alpha_0$  and  $\alpha_1$ ). The inner axes show the cumulative EPSP KL distance for a particular stimuli pair. The y-axis of the inner plots is resistor averaged KL distance /  $10^2$  (units of bits). These EPSP cumulative KL distances show some of the same transient and steady-state behavior seen in the dataset  $LI_1$ , though it is much less pronounced.

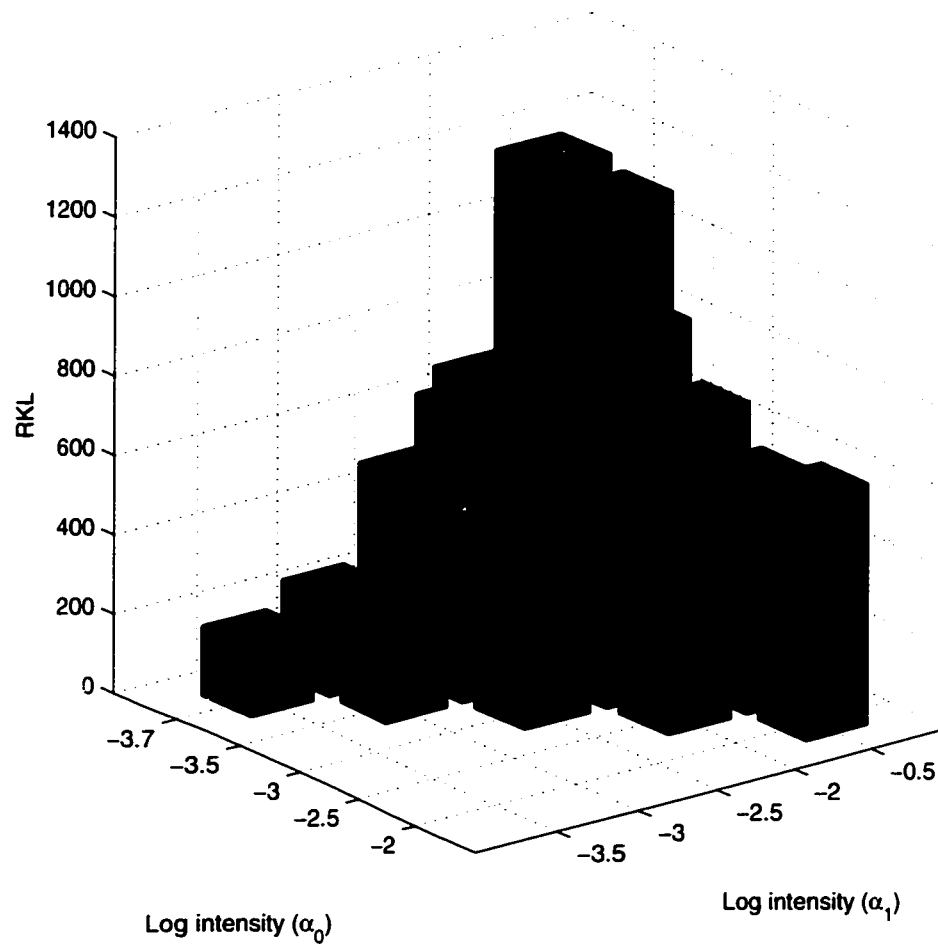


**Figure 5.14** SF KL distances calculated for the total EPSP response. The axes denote the stimuli values that elicited the responses ( $\alpha_0$  and  $\alpha_1$ ). The height of the bar is the total KL distance accumulated over the analysis segment, and is the final value of the cumulative EPSP KL plotted in figure 5.13. Generally, larger stimuli differences produce larger EPSP KLs.

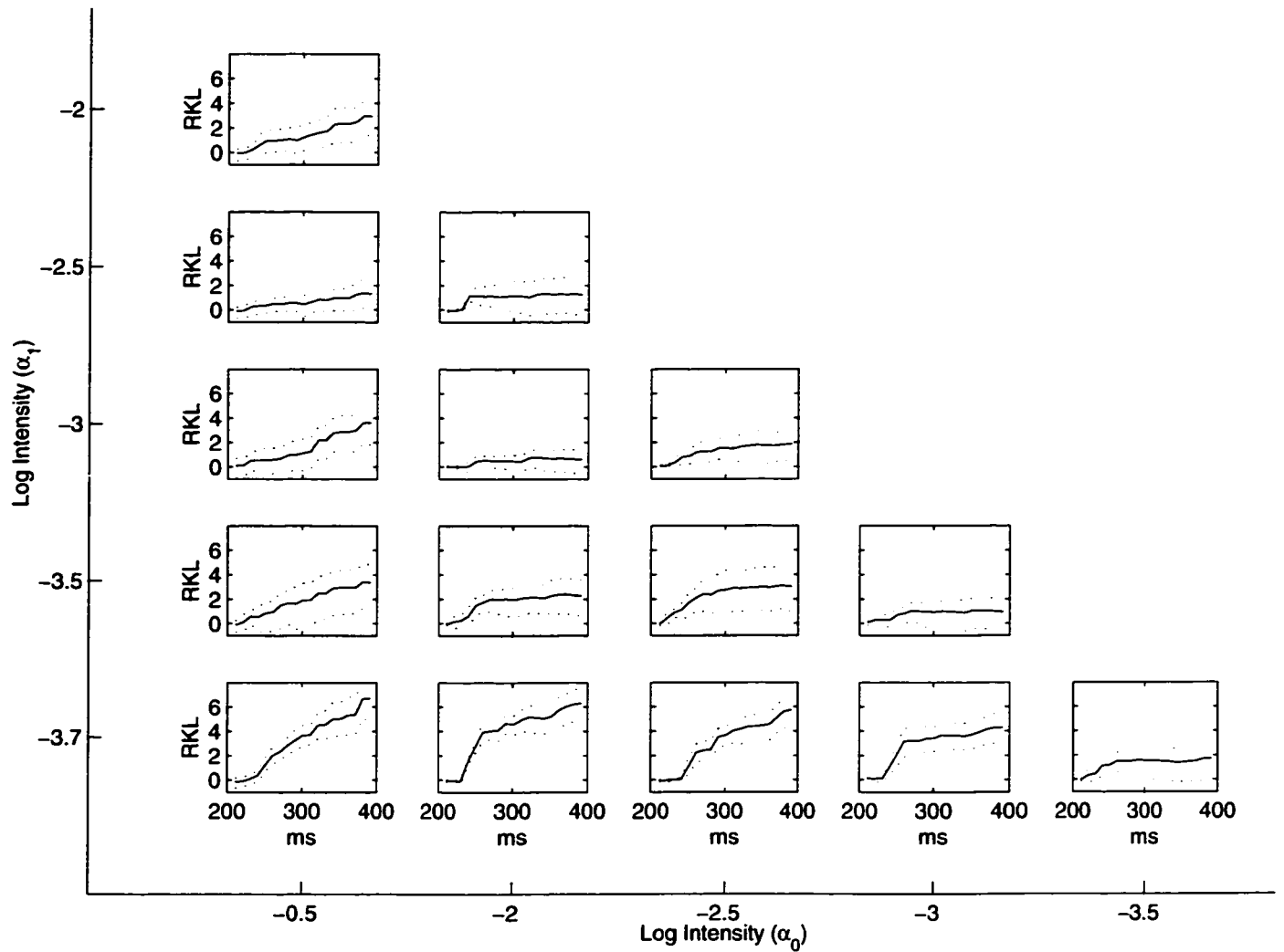


**Figure 5.15** *SF output (spike) cumulative KL distances for all stimuli pairs from sudden-onset, light intensity dataset  $LI_2$ . The outer axes denote the stimuli values that elicited the responses ( $\alpha_0$  and  $\alpha_1$ ). The inner axes show the cumulative spike KL distance for a particular stimuli pair. The y-axis of the inner plots is resistor averaged KL distance (units of bits). Notice that this axis is two orders of magnitude smaller than the EPSP cumulative KL plots shown in figure 5.13. Error bars (90<sup>th</sup> percentile) estimated using the bootstrap procedure are also shown as dotted lines. Spike response KLs for this dataset also show some of the same general behavior as the dataset  $LI_1$ , though less pronounced.*

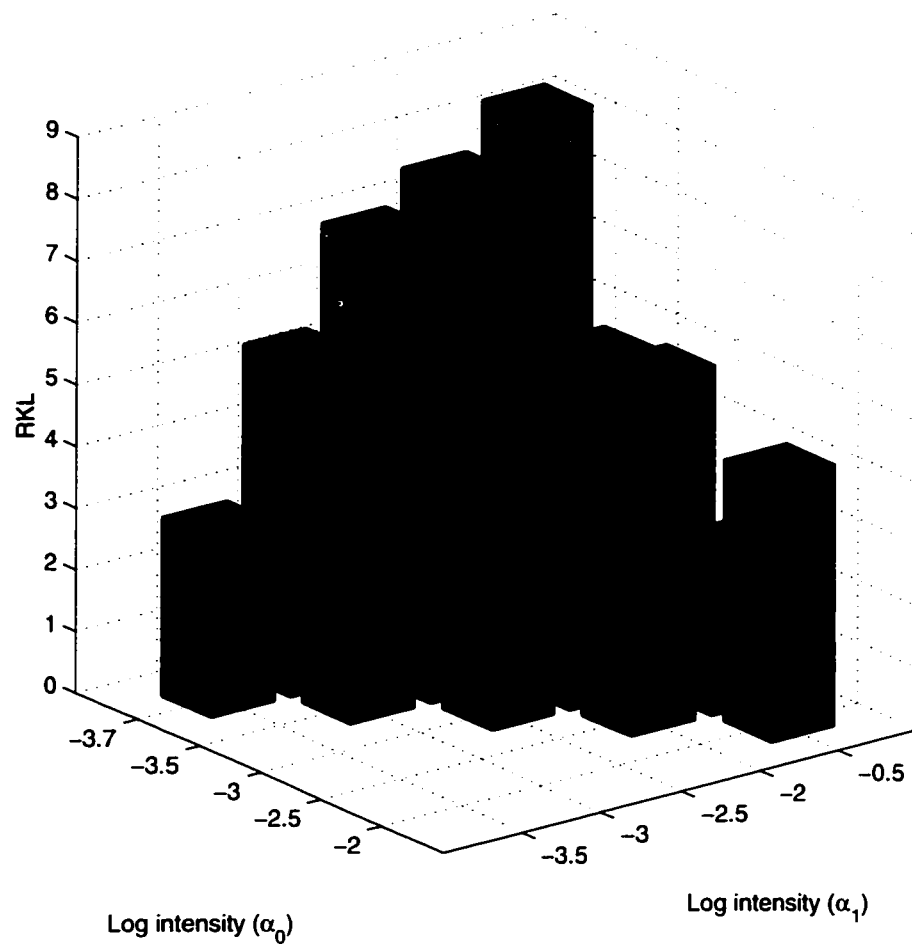


**Figure 5.16** SF KL distances calculated for the total spike response from dataset  $LI_2$ . The axes denote the stimuli values that elicited the responses ( $\alpha_0$  and  $\alpha_1$ ). The two light segments of each bar represent the confidence intervals, with the separating line indicating the estimated total KL distance accumulated over the analysis segment (the final value of the cumulative spike response KL plotted in figure 5.15). Generally, larger stimuli differences produce larger spike response KLs. The weakest stimuli ( $LI_2 = -3.7$ ) is at (or below) threshold for eliciting a SF response. The spontaneous discharging generates large KLs when compared with the structured responses to above-threshold stimuli.

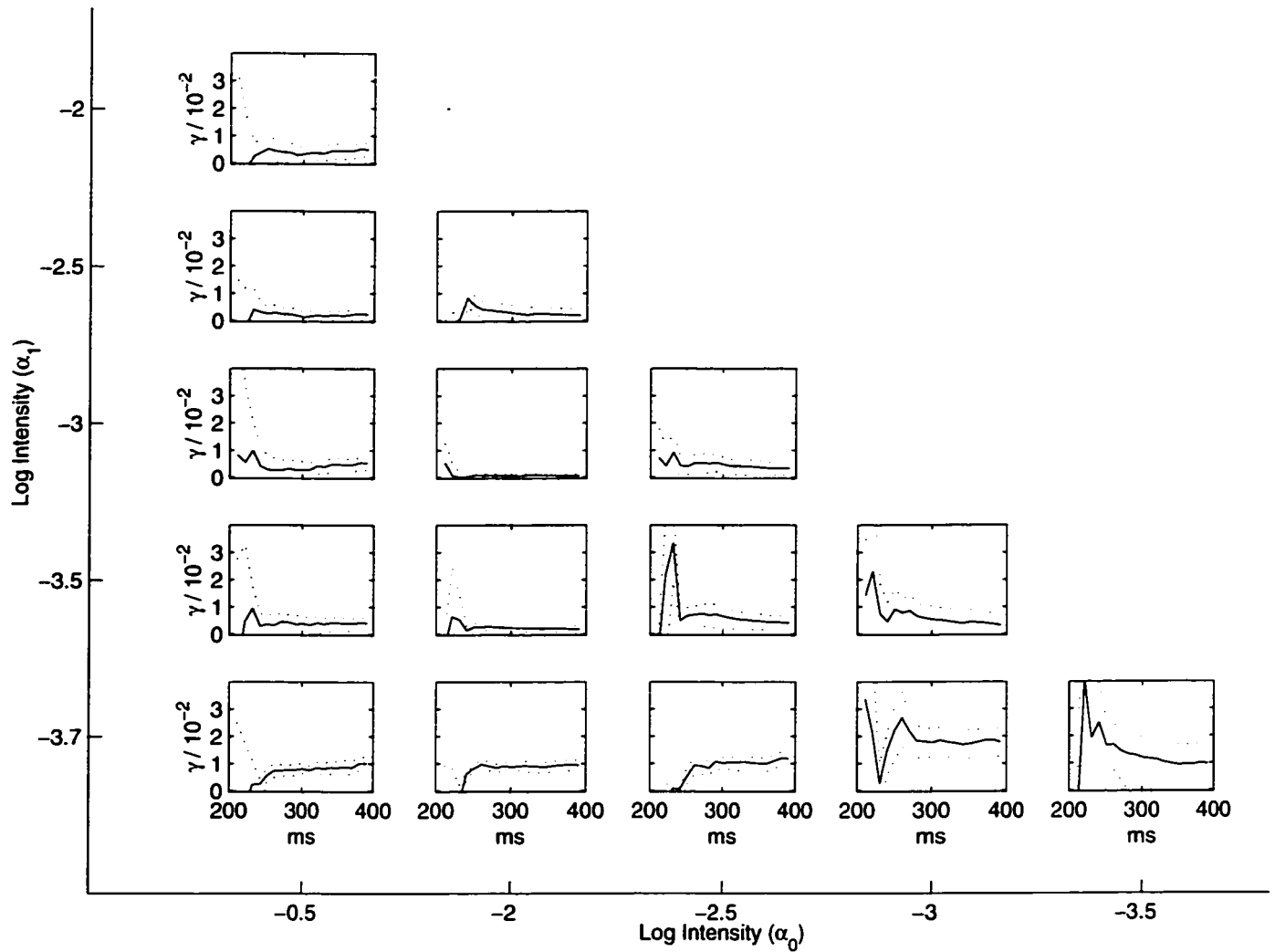


**Figure 5.17** SF time-varying information transfer ratios for all stimuli pairs from sudden-onset, light intensity dataset  $LI_2$ . The outer axes denote the stimuli values that elicited the responses ( $\alpha_0$  and  $\alpha_1$ ). The inner axes show the information transfer ratio for a particular stimuli pair as a function of time. The y-axis of the inner plots is information transfer ratio /  $10^{-2}$  ( $\gamma/10^{-2}$ ), and is unit-less. As with dataset  $LI_1$ , the time-varying information transfer ratios generally show a peak during the transient response and a decay to a relatively constant steady-state value. The peaks are more pronounced for small stimulus changes than for large changes.

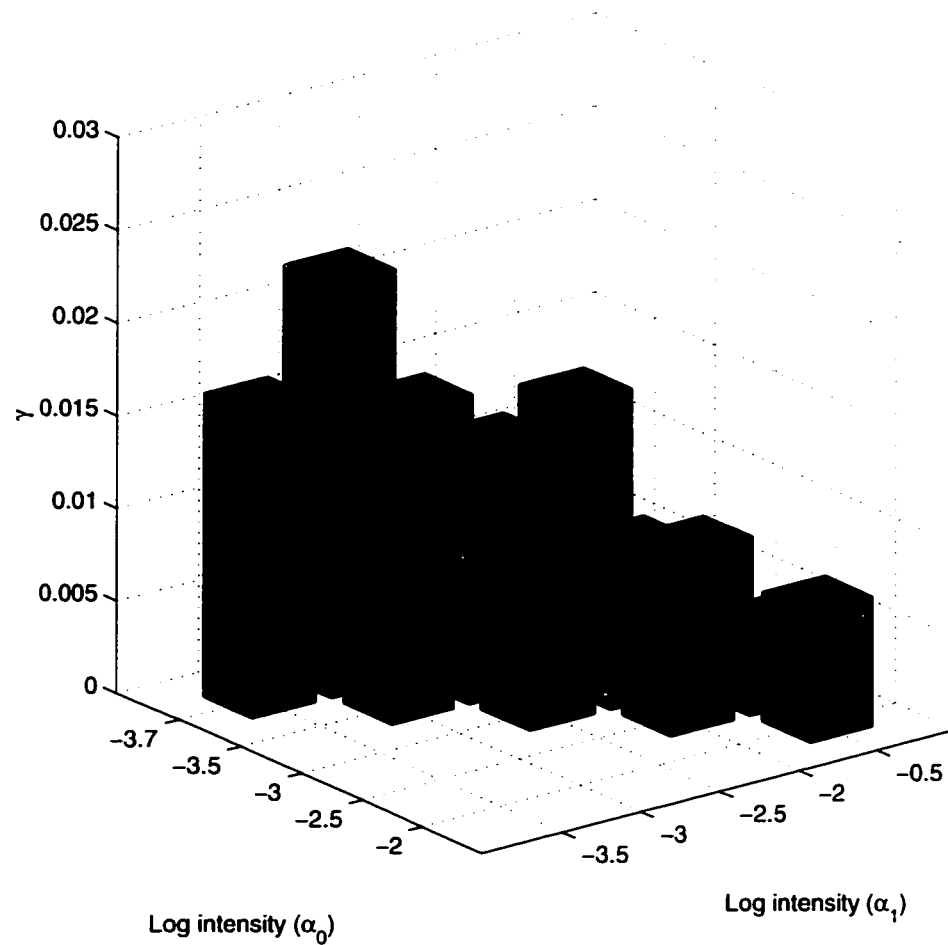


**Figure 5.18** Steady-state SF information transfer ratios for sudden-onset, light intensity dataset  $LI_2$ . The axes denote the stimuli values that elicited the responses ( $\alpha_0$  and  $\alpha_1$ ). The two light segments of each bar represent the confidence intervals, with the separating line indicating the steady-state information transfer ratio for the stimuli pair (the final value of the time-varying information transfer ratio plotted in figure 5.17). The weakest stimulus ( $LI_2 = -3.7$ ) appears to be at (or below) threshold of eliciting SF response. The large KL distances generated when comparing the spontaneous SF discharges in this case to the structure spike responses of stronger stimuli cause the information transfer ratios involving this stimulus to also be higher than the others.

### 5.3 Sine-wave Grating Spatial Frequency Dataset 1 ( $SW_1$ )

The first spatial frequency dataset consists of fixed SF responses to moving sine-wave gratings with spatial frequency parameter values chosen from the set  $SW_1 = \{60, 40, 30, 24, 20, 12\}$ . The spatial frequency parameter  $SW_1$  represents the spatial wavelength of a sine-wave grating, measured in deg/cycle. The spatial wavelength of a grating is the angular distance in the visual field covered by one grating period. In this dataset all of the gratings were moving with an orientation of  $225^\circ$  and a temporal frequency of approximately 2 Hz. A temporal frequency of 2 Hz means that the speed of the stimulus is adjusted depending on the spatial frequency so that a fixed point in space (e.g., the middle of the SF visual field) will have an intensity that varies sinusoidally with a frequency of 2 Hz. An orientation of  $0^\circ$  would represent horizontal bars moving from top to bottom, and  $90^\circ$  would represent vertical bars moving from the front of the preparation to the back. Other orientations represent the logical extension from these examples. In this preparation the membrane capacitance and resting conductance were determined to be 13.6 nF and  $1/(4.45 \text{ M}\Omega)$  respectively.

The mean EPSP signals elicited from these stimuli are shown in figure 5.19, and the corresponding spike response PST histograms in figure 5.20. The EPSP responses to the sine-wave grating stimuli in this dataset have smaller overall signal power than those in the sudden-onset datasets ( $LI_1$  and  $LI_2$ ). The corresponding spike responses also have lower overall discharge rates than the sudden-onset stimuli datasets.

Stimulus-dependent delay was estimated for sudden-onset stimuli datasets  $LI_1$  and  $LI_2$  by determining the beginning of significant signal activity. Sine-wave gratings are continuously repeating stimuli, with no onset landmark to identify. As discussed in section 4.3, EPSP and spike response pairs are compared using the phase shifts yielding minimum KL distances at the SF input and output. Circular shifts in a pair of responses will not affect the total KL accumulated over one response

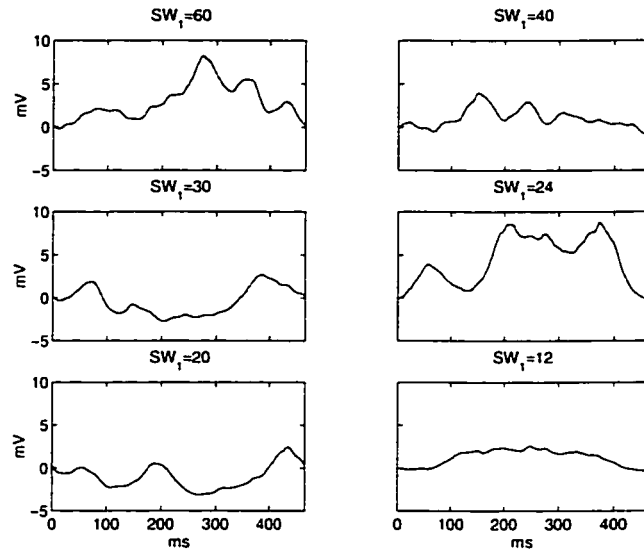


**Figure 5.19** Mean EPSP signals from sine-wave grating, spatial frequency dataset  $SW_1$ . Above each plot is the wavelength stimulus value producing the EPSP responses. Mean EPSPs are found by averaging responses from several stimulus repetitions.

period, but can affect the cumulative KL distance as a function of time. Because there is no concept of a stimulus onset time and therefore no way to compare cumulative KLs at the SF input and output, only the total KL distance accumulated over a period will be examined.

The total EPSP KL distances for each stimuli pair are plotted in figure 5.21. As with the plots for dataset  $LI_2$ , the stimulus values are not equally spaced. The spacing between plotted bars does not reflect the unequal spacing between stimuli values, and the axes must be carefully read to determine the stimulus change. The total EPSP KL distances are on the same scale as the EPSP KLs from dataset  $LI_1$ , but the same trends observed there are not present here. All pairs involving the response to stimulus  $SW_1 = 24$  deg/cycle have larger than average EPSP KL distances. Excluding those responses, all other pairs have a relatively constant total KL near  $10^4$ . In particular, larger KLs for larger stimulus changes are *not* observed.

Total spike response KL distances for each stimuli pair are plotted in figure 5.22. The total spike KLs for this dataset are on the same scale as the responses to the sudden-onset stimuli. Unlike



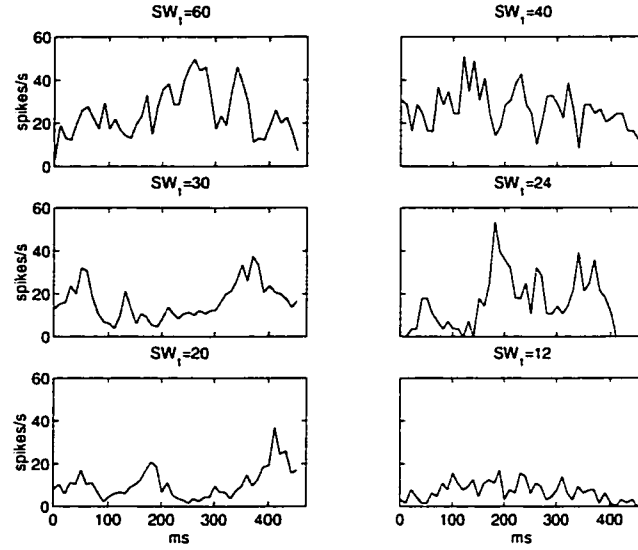


**Figure 5.20** *Post-stimulus time (PST) histograms from sine-wave grating, spatial frequency dataset  $SW_1$ . Above each plot is the wavelength stimulus value producing the EPSP responses. PST histograms are found by quantizing spike responses from several stimulus repetitions into bins and averaging the spike counts in each bin. The PSTs shown here are also normalized by the binwidth to estimate the time-varying spike discharge rate [11].*

the EPSP responses for this dataset, the spike responses do exhibit larger KLs for larger stimulus changes. The presence of output KL distance structure that is not evident with the input KLs is surprising and inexplicable at this point. There does appear to be a preference in the spike KL distances toward the left portion of figure 5.22. Because of the unequal spacing between the spatial wavelengths in the set  $SW_1$ , adjacent stimuli pairs in the left half of the figure represent greater absolute stimulus changes than those pairs in the right half of the figure.

The information transfer ratios for each stimuli pair are also plotted in figure 5.23. The information transfer ratios for this dataset are on the same scale as the information transfer ratios for dataset  $LI_1$ . The information transfer ratios exhibit some structure, with larger values for larger changes in stimuli. This trend occurs because the same behavior is observed in the spike KLs, but very little structure is present in the EPSP KLs.

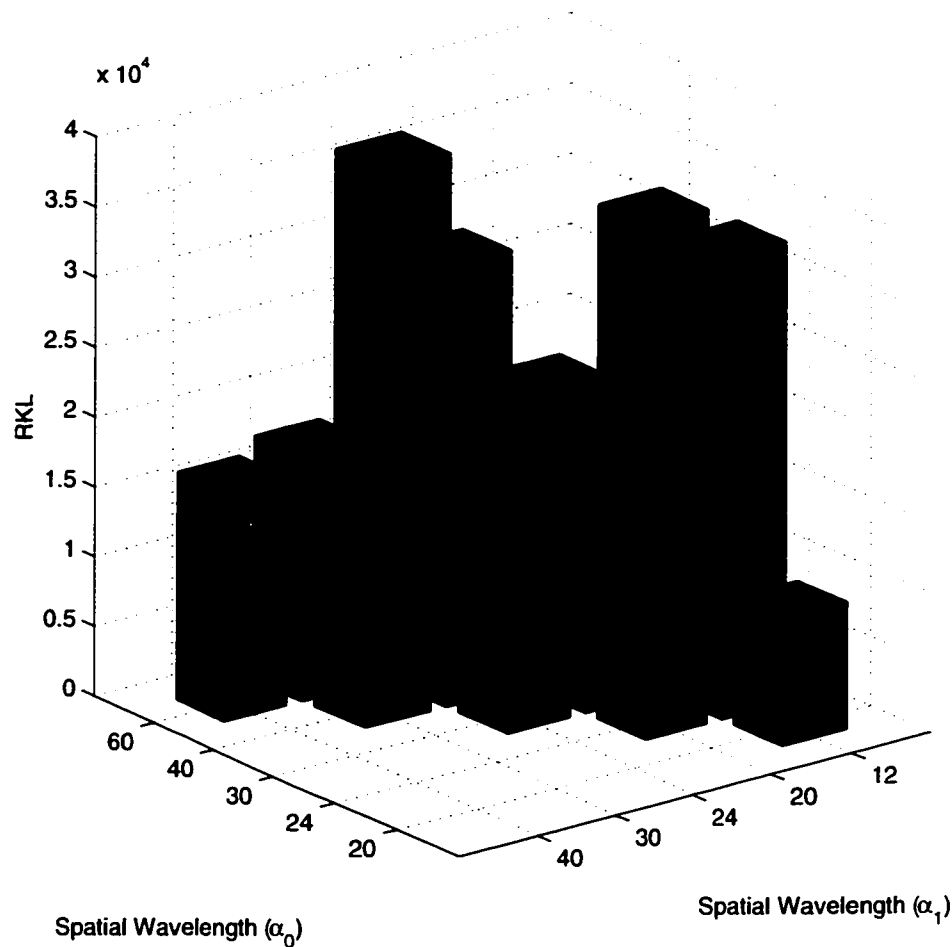


**Figure 5.21** SF KL distances calculated for one period of EPSP response to sine-wave grating stimuli. The axes denote the stimuli values that elicited the responses ( $\alpha_0$  and  $\alpha_1$ ). The height of the bar is the total KL distance accumulated over one period.

#### 5.4 Sine-wave Grating Spatial Frequency Dataset 2 ( $SW_2$ )

The second spatial frequency dataset consists of fixed SF responses to moving sine-wave gratings with spatial frequency parameter values chosen from the set  $SW_2 = \{60, 40, 30, 24, 20, 12\}$ . These are the same spatial wavelengths used in the first spatial frequency dataset ( $SW_1$ ). In this dataset all of the gratings were moving with an orientation of  $45^\circ$ , the opposite direction as the gratings in dataset  $SW_1$ . The grating again had a temporal frequency of approximately 2 Hz. The same preparation and unit was used in this dataset as was used in  $SW_1$ , so the membrane capacitance and

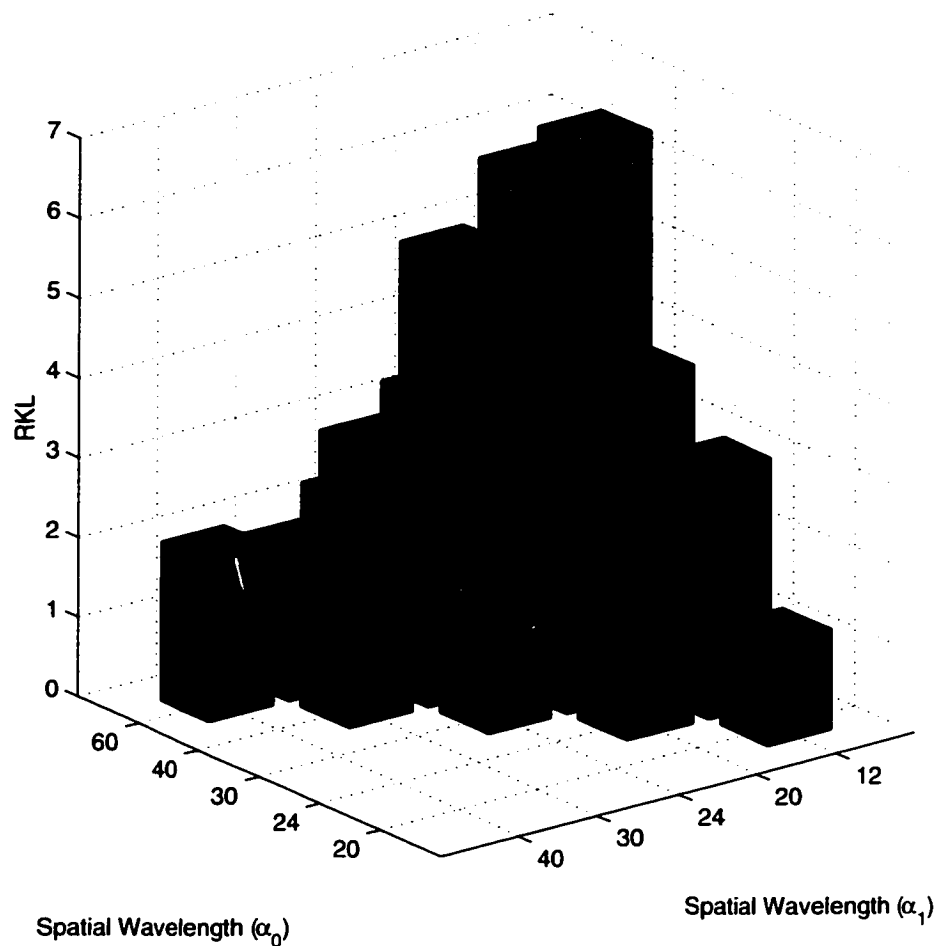


**Figure 5.22** SF KL distances calculated for one period of a spike response to sine-wave grating stimuli. The axes denote the stimuli values that elicited the responses ( $\alpha_0$  and  $\alpha_1$ ). The two light segments of each bar represent the confidence intervals, with the separating line indicating the estimated total KL distance accumulated over one period.

resting conductance values are the same.

The mean EPSP signals elicited from these stimuli are shown in figure 5.24, and the corresponding spike response PST histograms in figure 5.25. Both the mean EPSPs and spike responses have less overall structure than responses to the same stimuli moving in the opposite direction (dataset  $SW_1$ ).

The total EPSP KL distances for each stimuli pair are plotted in figure 5.26. The EPSP KL distances are on the same scale as the EPSP KLs generated with the dataset  $SW_1$ , but in this dataset

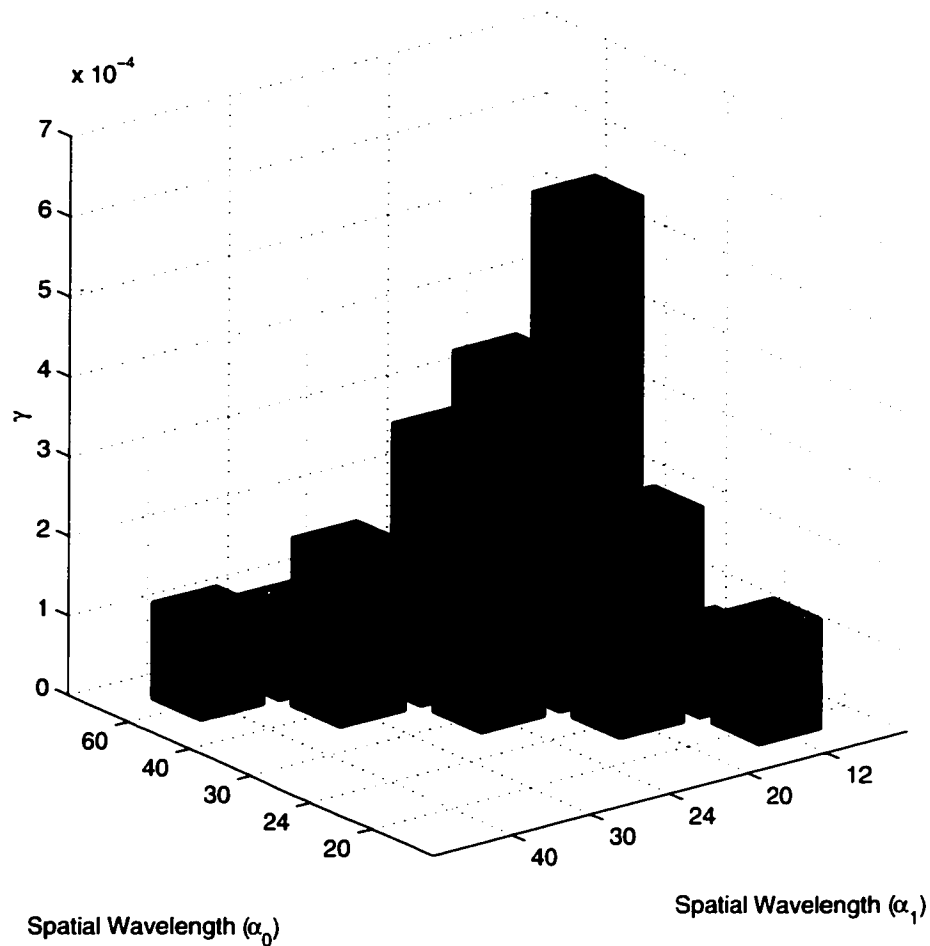


**Figure 5.23** SF information transfer ratios for sine-wave grating, spatial frequency dataset  $SW_1$ . The axes denote the stimuli values that elicited the responses ( $\alpha_0$  and  $\alpha_1$ ). The two light segments of each bar represent the confidence intervals, with the separating line indicating the information transfer ratio  $\gamma$  for the stimuli pair.

there are not large distances generated when the stimulus with spatial wavelength  $SW_2 = 24$  is used. The apparent preference for differentiating the stimulus  $SW_1 = 24$  and not  $SW_2 = 24$  could represent directionally selective “tuning” for a particular spatial frequency, or it may be an anomaly of this dataset. The behavior should be observed across a broader range of preparations to examine the presence of a significant trend. As in dataset  $SW_1$ , the EPSP responses do not generate the largest KL distances for the largest spatial wavelength changes. There does appear to be a slight preference for the stimuli pairs shown in the left half of figure 5.26, representing larger spatial

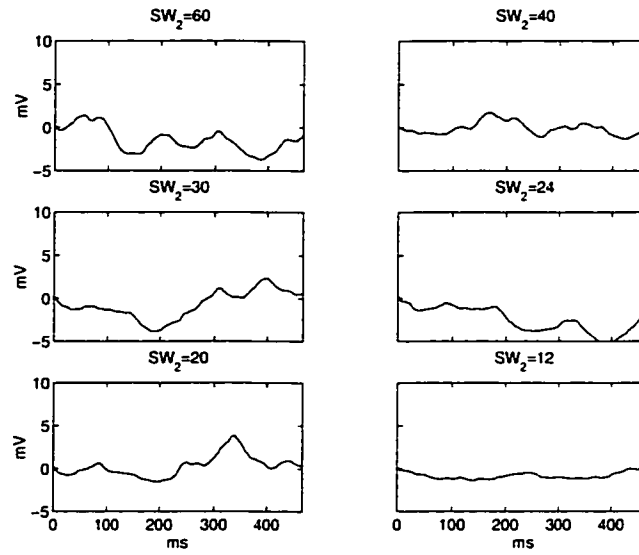


**Figure 5.24** Mean EPSP signals from sine-wave grating, spatial frequency dataset  $SW_2$ . Above each plot is the wavelength stimulus value producing the EPSP responses. Mean EPSPs are found by averaging responses from several stimulus repetitions.

wavelengths and absolute stimulus changes than the pairs on the left half of the figure.

Total spike response KL distances for each stimuli pair are plotted in figure 5.27. The spike KLs in this dataset show larger KL distances between responses with large stimulus changes. This trend was observed in all of the sudden-onset datasets, but not in the first sine-wave grating dataset  $SW_1$ .

The information transfer ratios for each stimuli pair are also plotted in figure 5.28. The information transfer ratios for this dataset are generally near  $10^{-4}$ , as in the  $LI_1$  dataset. Because the EPSP KLs show little structure and the spike KLs show preference for both large stimulus changes and stimuli with large wavelengths, those trends are also observable in the information transfer ratios.

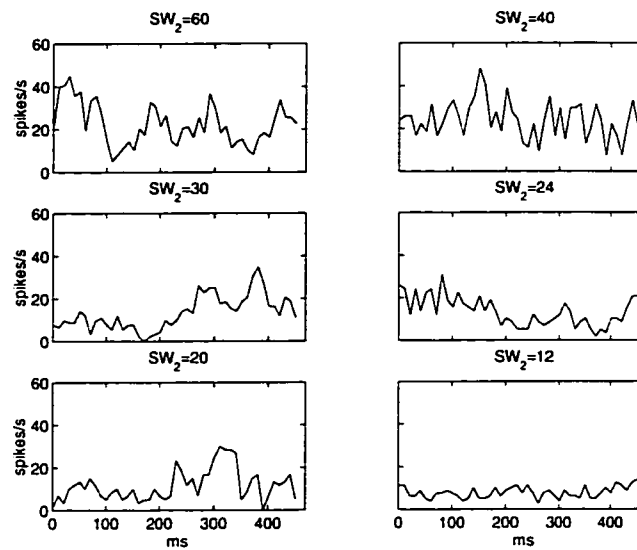


**Figure 5.25** Post-stimulus time (PST) histograms from sine-wave grating, spatial frequency dataset  $SW_2$ . Above each plot is the wavelength stimulus value producing the EPSP responses. PST histograms are found by quantizing spike responses from several stimulus repetitions into bins and averaging the spike counts in each bin. The PSTs shown here are also normalized by the binwidth to estimate the time-varying spike discharge rate [11].

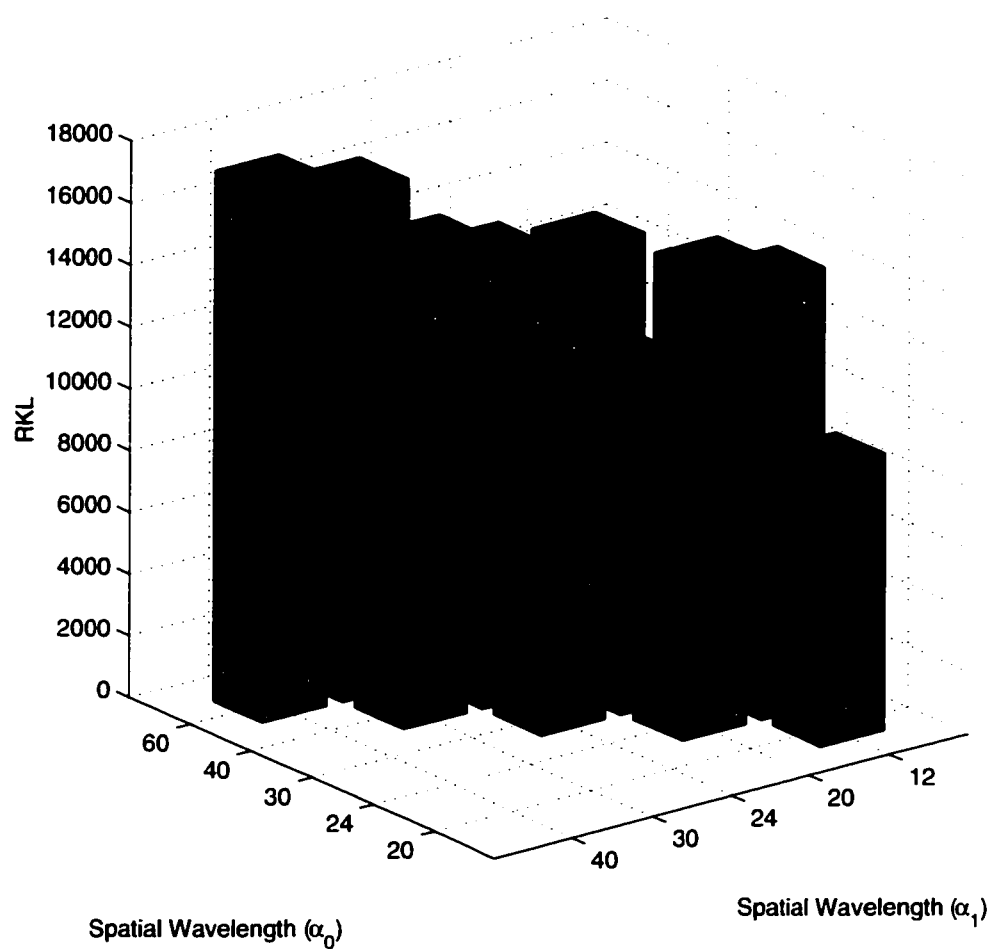


**Figure 5.26** SF KL distances calculated for one period of EPSP response to sine-wave grating stimuli. The axes denote the stimuli values that elicited the responses ( $\alpha_0$  and  $\alpha_1$ ). The height of the bar is the total KL distance accumulated over one period.

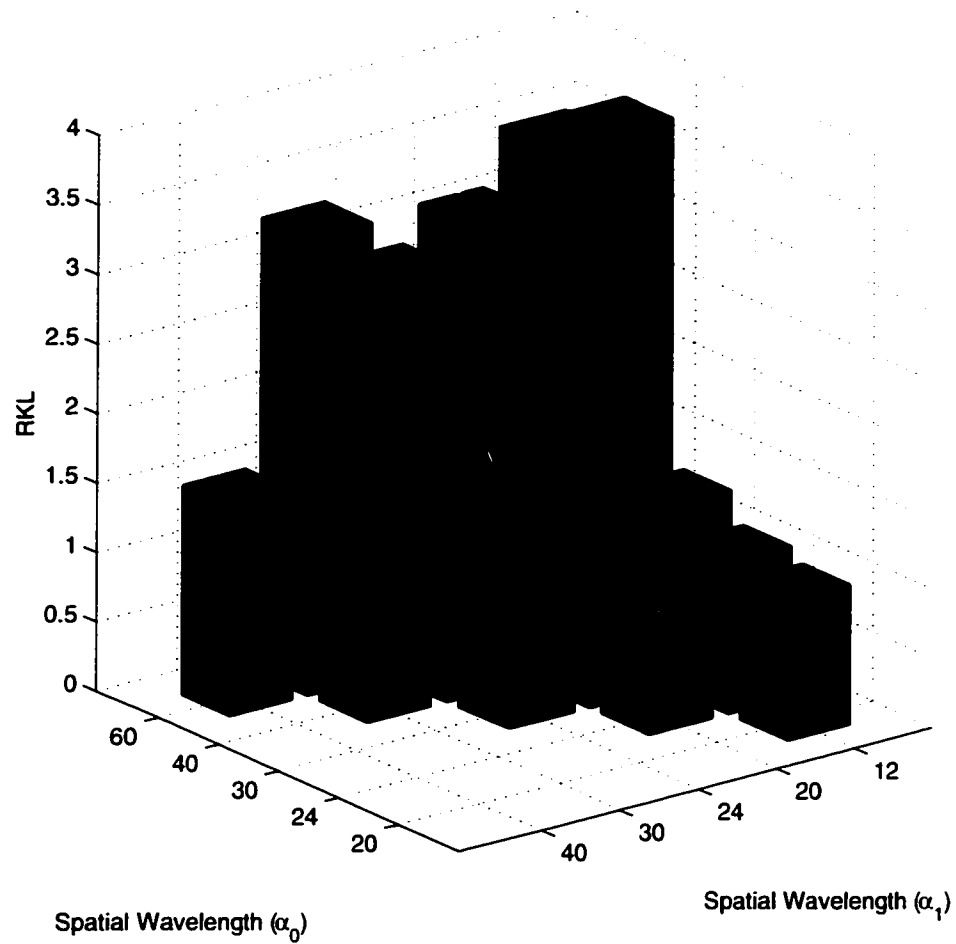


**Figure 5.27** SF KL distances calculated for one period of a spike response to sine-wave grating stimuli. The axes denote the stimuli values that elicited the responses ( $\alpha_0$  and  $\alpha_1$ ). The two light segments of each bar represent the confidence intervals, with the separating line indicating the total KL distance accumulated over one period.



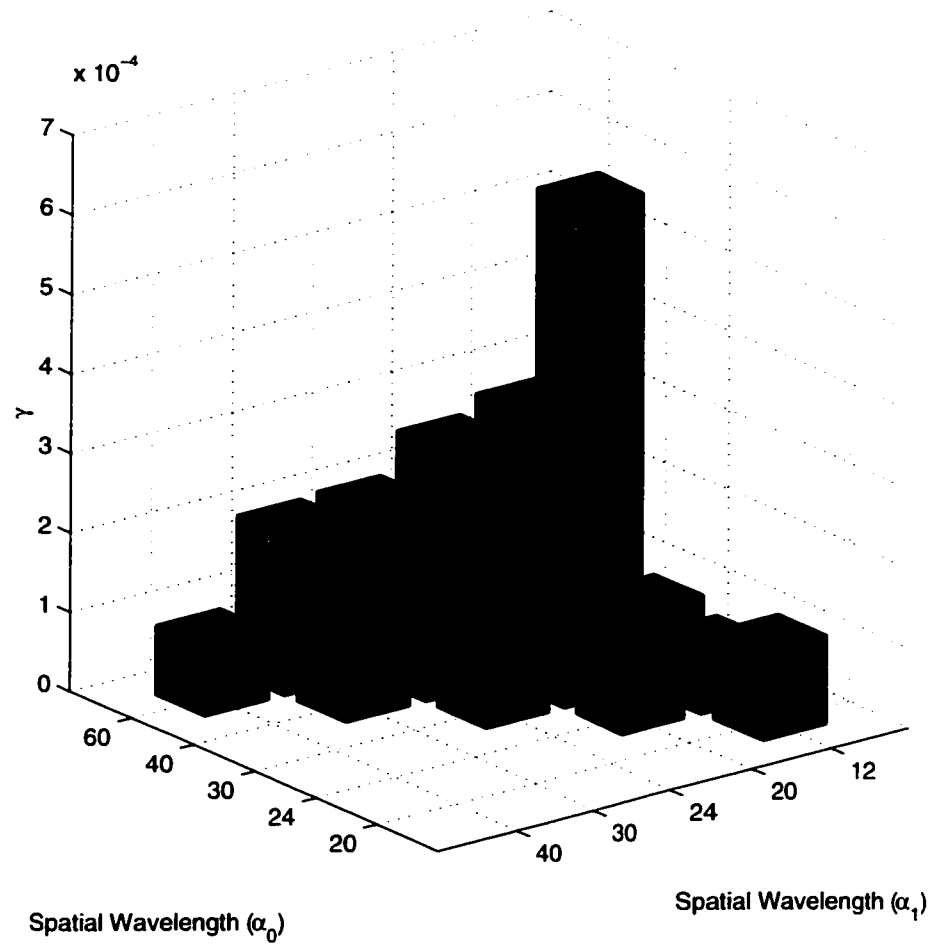


**Figure 5.28** SF information transfer ratios for sine-wave grating, spatial frequency dataset  $SW_2$ . The axes denote the stimuli values that elicited the responses ( $\alpha_0$  and  $\alpha_1$ ). The two light segments of each bar represent the confidence intervals, with the separating line indicating the information transfer ratio  $\gamma$  for the stimuli pair.

### 5.5 Sine-wave Grating Orientation (Motion Direction) Dataset (*SD*)

The sine-wave grating stimuli used as datasets  $SW_1$  and  $SW_2$  present gratings with the same wavelength parameters to the same preparation and neural unit, but with opposite motion directions. These datasets can also be considered jointly as six separate trials where orientation (motion direction) is the changing parameter. To be explicit, responses to the same wavelength and opposite motion directions are compared directly for all six different values of grating spatial wavelength. The EPSP KLs, spike response KLs and information transfer ratios are plotted in figure 5.29. The

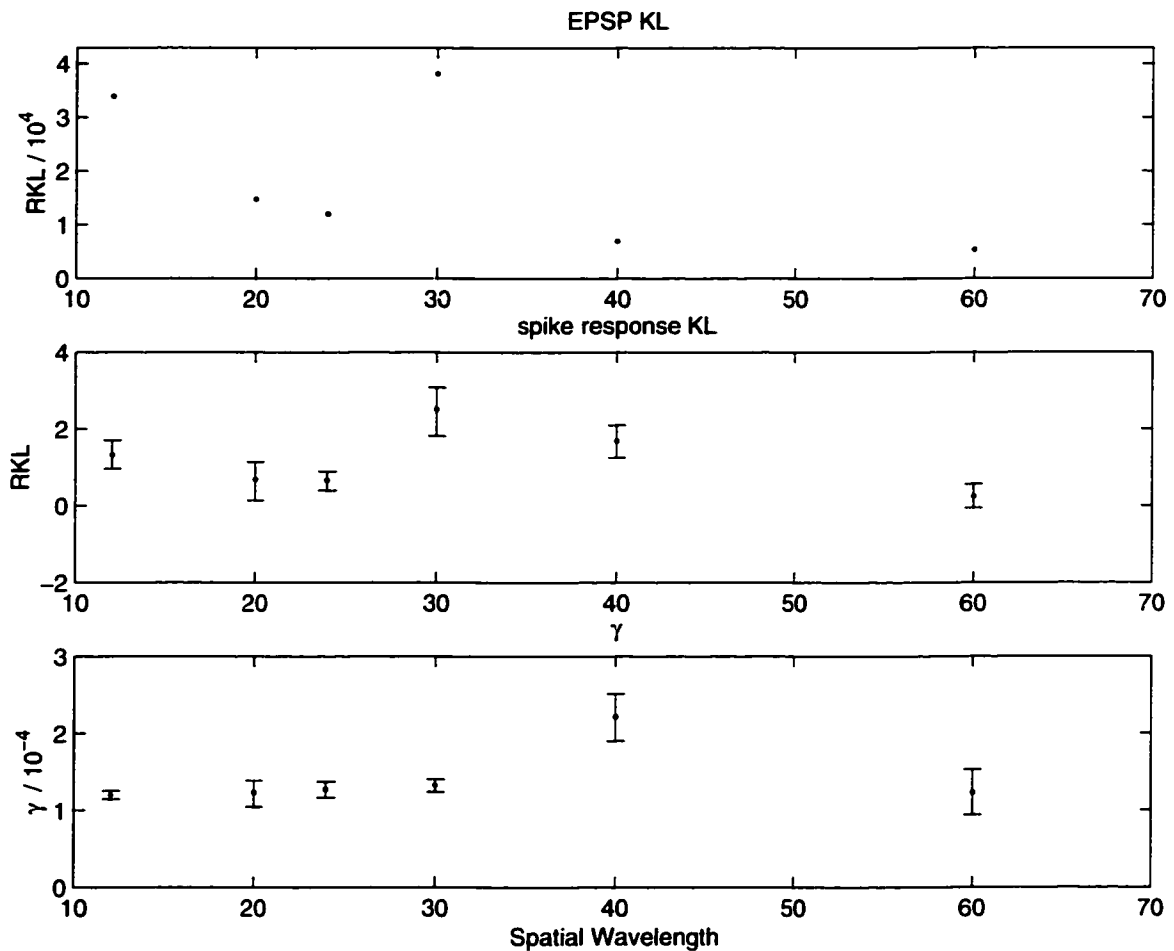


**Figure 5.29** Responses to sine-wave gratings with the same wavelength and opposite motion direction were compared separately for all six values of wavelength available in datasets  $SW_1$  and  $SW_2$ . The top plot shows the EPSP KL distances, the middle plot shows the spike response KL distances, and the bottom plot shows the information transfer ratios.

information transfer ratios are nearly all less than  $10^{-4}$ , with the exception of the responses to  $40^\circ$  deg/cycle stimuli. The information transfer ratios tend to increase as the spatial wavelengths approach  $40^\circ$  deg/cycle, possibly indicating a “tuning”, or preference for that range of stimuli when representing direction information.

## 5.6 Theoretical Spike Generator Example

The preceding data analysis illuminated some general trends: unexpectedly low values of the SF information transfer ratio, time-varying information processing capabilities with sudden-onset stimuli and possibly better information transfer for small stimulus changes. One wonders if these effects are inherent in any system that converts analog stimuli to point process responses or whether the SFs have unique characteristics. We want to explore the role of general spike generators and specifically the effect of discharge rates in such systems. We use a simple theoretical system that takes a Gaussian random variable  $\tilde{X} \sim N(\theta, \tilde{\sigma}^2)$  as input and produces a Poisson process  $\tilde{Y}$  with rate  $\lambda = G\tilde{X}$  as output ( $G$  is a deterministic scaling factor). By specifying  $\theta$  and  $\tilde{\sigma}^2$ , the unconditional distribution on  $\tilde{Y}$  can be analytically determined. Given two different mean input values  $\theta_0$  and  $\theta_1$ , the KL distance between the input Gaussian random variables and the output Poisson random variables can be analytically calculated. The derivation of the unconditional probability at the output of this theoretical system can be found in Appendix C. The calculation finds the probability mass function for  $\tilde{Y}$  (technically it has infinite support, but enough terms can be found to render the error negligible). This theoretical system is not intended to be an accurate model for SF behavior, but rather an abstract exploration of spike generators having input SNRs and output discharge rates similar to the SFs.

We explored the theoretical system’s information processing properties by varying the difference

between input means  $\theta_0$  and  $\theta_1$  which were chosen to be comparable to the steady-state EPSP values found in dataset  $LI_1$ . A gain factor  $G$  was chosen so that  $\lambda$  was comparable to the steady-state discharge rates seen in the same data. The results are plotted in figure 5.30. The output KL distance

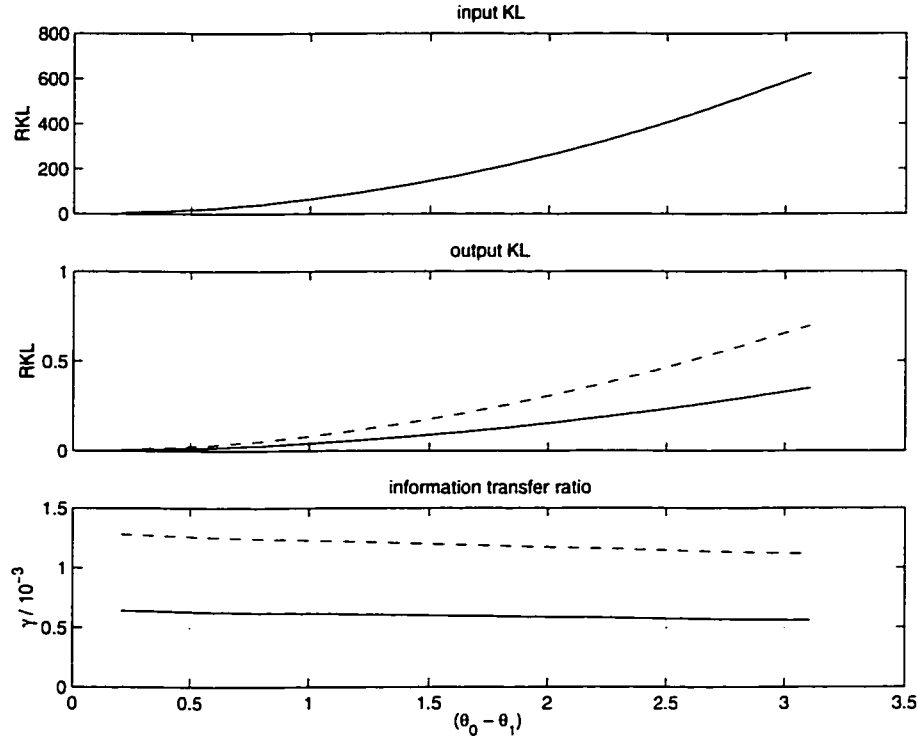


**Figure 5.30** Information processing characteristics for a simple theoretical spike generator. The top panel shows the input KL for two Gaussian random variables with increasing difference between the means,  $(\theta_0 - \theta_1)$ . The middle panel shows the output KL for a simple spike generator with event rates that are multiplicative scalings of the input means. As the input mean difference increases the difference in event rates also increases contributing to higher KL. The dotted line shows the result when the scaling factor is doubled. The bottom panel shows the corresponding information transfer ratios. The event rates are in the same general range as the steady-state spike rates typically seen in SF data, and the information transfer ratio is on the order of  $10^{-3}$ . The information transfer ratio for this simple theoretical system does show the trend that the system has better information processing capabilities for small input changes than for large changes.

is plotted as the solid line in the middle panel of figure 5.30. As expected, increasing the input mean difference  $(\theta_0 - \theta_1)$  increases the rate difference  $(\lambda_0 - \lambda_1)$ , and therefore increases the KL distance at the system output. The resulting information transfer ratio is plotted as the solid line in the bottom panel of figure 5.30. The output KL values (and consequently the information transfer ratios) are

much smaller than those estimated in the  $LI_1$  data. The discrepancy exists partially because in this simple spike generator we approximate rates (and input-output relationships) that are similar to only the steady-state portion of the SF responses. Two distinct trends observed in this theoretical spike generator match those seen in the SF analysis: the information transfer ratios are very low using the present rates and the system has better information processing capabilities for small changes in the input than large changes. The same experiment was repeated with the gain factor doubled (doubling the output rates), and these results are plotted in figure 5.30 as dotted lines. The increased output rates also increase the output KL distance and therefore increase the information transfer ratio.

The simple system can be extended to explore the time-varying nature of its information transfer ratio to input *changes*. Given a Gaussian random process  $\tilde{X}(t)$ , an intensity function  $\lambda(t) = G\tilde{X}(t)$  can be formed in the same manner as above. The unconditional probability mass function on event counts in a time bin  $0 \leq t \leq T$  depends on the integral of the intensity function over that bin,  $\Lambda(0, T) = \int_0^T \lambda(t)dt$ . If  $\tilde{X}(t)$  is a Gaussian random process then  $\Lambda(0, T)$  is a Gaussian random variable. Given input random processes with two different means, the unconditional probability mass functions for event counts in the bin  $0 \leq t \leq T$  and the resulting output KL distance can be computed. In the SF spike responses to sudden-onset stimuli there is transient behavior that cannot be explained by a simple scaling of the EPSPs. The sudden EPSP *changes* also play a role in increasing the discharge rate. We can use a more complicated intensity function to capture some transient behavior in the output process. We use an extended intensity function

$$\lambda(t) = G_s \tilde{X}(t) + G_t \frac{d\tilde{X}(t)}{dt}, \quad (5.1)$$

incorporating both a steady-state gain  $G_s$  and a transient gain  $G_t$ . The statistics of  $\Lambda(0, T)$  are

only slightly more complicated to compute using this extended intensity function. As in the earlier theoretical system, we do not intend to model actual SF spike generation. The only goal of this theoretical spike generator is to explore the time-varying information processing properties of a simple spike generation system that incorporates dependence on input changes over time.

Using a sample pair of responses from the  $LI_1$  dataset, values of  $G_s$  and  $G_t$  are estimated that roughly predict the discharge rate range estimated in PST histograms for spike responses under both stimulus conditions. The top panels of figure 5.31 show the mean EPSP functions for the two example stimuli. The middle panels contain the PST histogram estimated rates as dots and solid lines indicating event rates predicted by approximating equation (5.1) using the mean EPSPs. The cumulative EPSP KLs taken from the data analysis of section 5.1 are plotted in the top panel

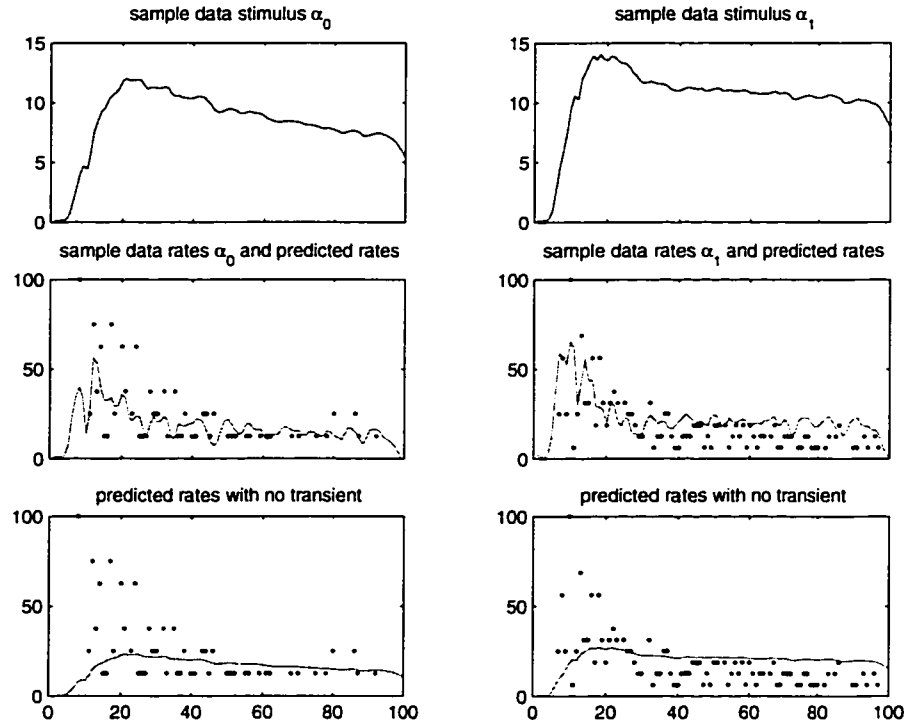


**Figure 5.31** Sample mean EPSPs, estimated spike rates from data and predicted event rates. The top panels show the mean EPSPs from the sample pair of stimuli taken from the  $LI_1$  dataset. The middle panels show the estimated spike rates from the data PST histograms (as dots) and the event rates predicted from the EPSPs and equation (5.1). The bottom panels show the same estimated spike rates from the data and predicted rates when  $G_t = 0$ .

of figure 5.32. We determine the probability mass functions for event counts in each bin using

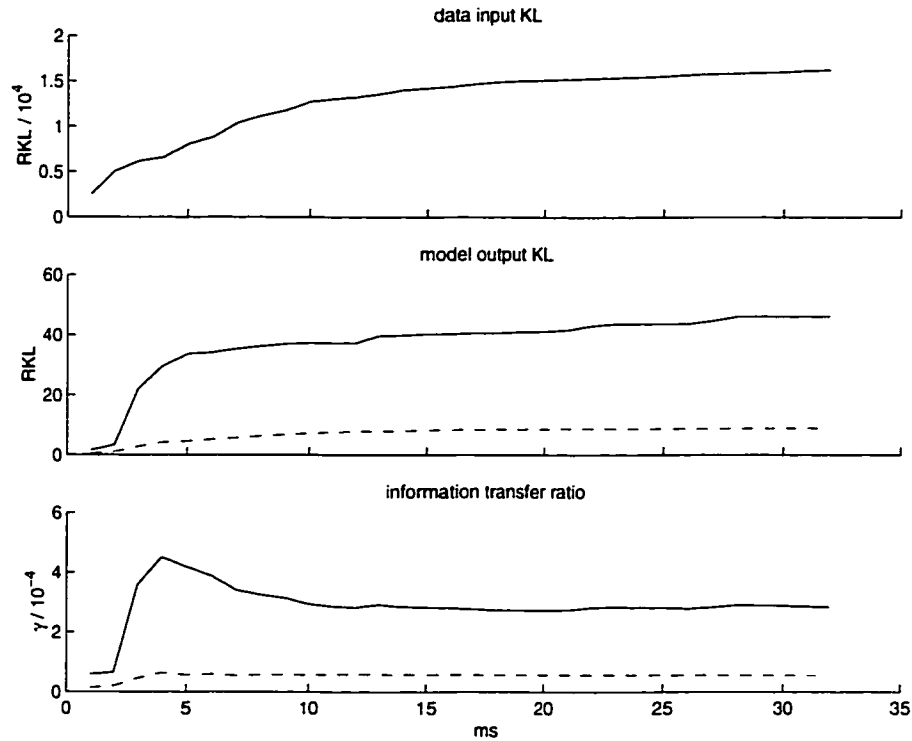


**Figure 5.32** Information processing characteristics of a simple time-varying system. The input processes are an example pair of EPSP responses from dataset  $LI_1$ . Their cumulative KLs are shown in the top panel. The middle panel shows the cumulative KL for the simple theoretical spike generator. The solid line shows results from the complex intensity function depending on the EPSP derivative and the dotted line shows results from the simplified intensity function with  $G_t = 0$ . The bottom panel shows the time-varying information transfer ratio for this theoretical system. The solid line again denotes results from the complex intensity function and the dotted line represents results from the simplified intensity function. Notice that when the output's direct dependence on transient input behavior is removed by simplifying the intensity function, the information transfer ratio does not exhibit the same sharp transient peak.

the intensity function of equation (5.1) and the mean EPSPs under each stimulus condition. The cumulative KLs are calculated (assuming independent bins) and are plotted as the solid line in the middle panel of figure 5.32. The resulting time-varying information transfer ratio for this system is plotted as the solid line in the bottom panel of figure 5.32. The same transient peak seen in the SF analysis is also present here.

Even though both input and output KLs exhibit some transient and steady-state behavior, it is

not necessary that every system with time-varying behavior will automatically exhibit time-varying information processing capabilities. To illustrate, the same theoretical analysis was repeated setting  $G_t = 0$ . The output event rates will still have transient and steady-state rates because the input EPSPs have transient and steady-state values, but the higher-order explicit dependence on EPSP change is eliminated. The bottom panels of figure 5.31 shows the PST histogram estimated rates from the data as dots and solid lines indicate the event rates predicted using the mean EPSPs and equation (5.1) with  $G_t = 0$ . The resulting cumulative output KL and time-varying information transfer ratio are plotted as dashed lines in figure 5.32. The input and output cumulative KLs still show some transient and steady-state behavior, though it is less pronounced in the output KL. The time-varying information transfer ratio is much more constant and does not obviously show a large peak followed by a decay to a steady-state value.



## Chapter 6

### Conclusions

The SF information transfer ratios calculated in this work are tied together by their common range of the values. Regardless of the stimulus feature being examined (e.g., light intensity in sudden-onset stimuli, spatial frequency in sine-wave gratings, motion direction) the steady-state information transfer ratios were on the order of  $10^{-3}$  *at the maximum* (only in one case) and almost always on the order of  $10^{-4}$ . As described in section 2.4, the information transfer ratio is always between zero and one, with a value of zero representing total information loss about the stimulus change. Such a large decrease in information content at the SF stage is counter-intuitive as a system design. The SFs receive inputs from an excitatory receptive field that frequently has an inhibitory surrounding field. Other than the general receptive field properties, very little processing has been performed on the signals by the SF stage and it can be thought of as a front-end to stages where significant processing does occur. From a design standpoint, it is generally desirable to minimize unrecoverable loss at all stages, particularly in the front-end.

We must also recall that the information transfer ratio is not an arbitrary measure of performance, but specifically characterizes the asymptotic performance difference between optimal detectors operating on the EPSP and spike train responses. The asymptotic false alarm error rate for a Neyman-Pearson type detector has an exponential decay rate that is equal to the KL distances between the data. Because of the data processing inequality (2.1), the false-alarm error rate for the detector operating on the EPSP inputs must decay faster than the rate for the detector distinguishing the spike response outputs. Graphically, the performance difference is shown in 6.1. As the observation time increases ( $L$ ), the false-alarm error probabilities for optimal detectors at the

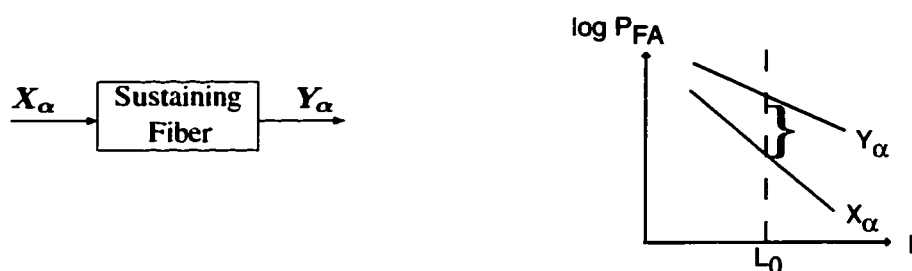


**Figure 6.1** Shown are conceptual asymptotic false-alarm rates for optimal Neyman-Pearson operating on the SF input EPSPs ( $X_\alpha$ ) and output spike trains ( $Y_\alpha$ ). The slopes of the lines are the negative of the EPSP and spike response KL distances. The ratio of the slopes is the SF information transfer ratio. The vertical offsets are problem dependent, so the absolute performance difference for an specific number of observations  $L_0$  is unknown.

input and output of a system will eventually become straight lines when plotted on semilogarithmic coordinates. The slopes of these lines are the negative of the KL distances between the probability functions. The *ratio* of these slopes is the information transfer ratio. In the simple theoretical spike generation example the information transfer ratio is on the order of  $10^{-3}$ , meaning the *slopes* differ by a factor of 1000 (three orders of magnitude). The large slope difference suggests that the performance gap can be overwhelming with increasing observation time.

We know crayfish are able to extract information about stimuli from SF output spike trains because eyestalk reflexes are influenced by the specific light stimulus. Initially the crayfish ability to extract useful information from the SF response seems to contradict the information processing analysis that shows very little stimulus information is being passed from input to output. It is imperative to remember the information transfer ratio measures information present at the SF output *relative* to information available at the input. There may be enough information in the SF output to make reasonable decisions about the stimulus, but the present question is how well *could* those decisions be made by observing the SF EPSP input instead. The very low information transfer ratio values can be illuminated by considering the rate at which the EPSP and spike signals can be used to convey information. In the analog EPSPs, information can be communicated as fast

as the highest frequencies present in those signals. Theoretically, even a sampled version of the analog signal could communicate information with each sample. However, a single spike train can only communicate information with each action potential, and it therefore limited by the discharge rate. With the stimuli used in this analysis, the discharge rates are not high enough to convey the vast amount of information about the stimulus contained in the analog EPSPs. The discrepancy is particularly evident when the EPSP SNRs are very high. The simple theoretical example in section 5.6 showed that the output KL distance increases (resulting in better information processing capabilities) as event rates increase. We conclude that the crayfish SF may be severely limited in its information processing capabilities by the low spike rates typically produced.

With the second sudden-onset light intensity dataset  $LI_2$ , the information transfer ratios were generally an order of magnitude larger than in the first sudden-onset light intensity dataset  $LI_1$ . The two experiments were essentially the same, but were performed on two different preparations. The primary difference in the datasets was the discrepancy in SNRs of the EPSP signals. The EPSP responses in the preparation used to collect the  $LI_2$  data were much noisier than the corresponding responses from the  $LI_1$  preparation. Though the spike responses KLs were on the same scale in these two datasets, a system's information processing capabilities are quantified according to what it presents at the output given what was present at the input. For preparations and units that output spike trains with comparable KLs, the unit that produces those spike responses with lower SNR EPSPs has suppressed less information about the stimulus present in the EPSPs. Because of the inherent variation between the responses, we may not make direct comparisons using data collected from different preparations.

Plotting the information transfer ratio as a function of time for the sudden-onset stimuli revealed an interesting trend in the dynamic SF information processing capabilities. The time-varying in-

formation transfer ratio generally revealed a sharp increase immediately after the stimulus onset, followed by a slow decrease to a sustained value during the steady-state response. The peak could be as much as an order of magnitude larger than the sustained value, and was generally more pronounced for small stimulus changes. When also observing the stimulus-dependent crayfish light reflex to sudden-onset stimuli, the behavior is complete within 100–150 ms after the transient spike response. Accounting for the latency of the motoneurons and muscle contractions, the information from the stimulus conveyed in the reflex behavior must be communicated through the SF in the first 100 ms after stimulus onset. This corresponds to the transient portion of the spike response, and corroborates our characterization of the time-varying SF information transfer ratio. The amount of information being transmitted about a whole stimulus from input to output may have overall low values, but the SF is communicating the majority of that information during the transient response.

The SF information processing capabilities appear to be limited in part by the discharge rates present at the output, which clearly depend on the value of the input EPSP ( $v(t)$ ). The performance increase during the transient response may be because of significant firing rate increases due to a dependence on *changes* in the EPSP  $\left(\frac{dv(t)}{dt}\right)$ . The same time-varying information transfer ratio behavior was observed with the simple theoretical spike generator described in section 5.6 when the outputs were explicitly dependent on recent changes in the input. The dynamic information transfer ratio peak was not as evident in the theoretical example when the output only depends on the current input value. With dependence only on the present input value ( $v(t)$ ) and no direct dependence on changes in the  $\left(\frac{dv(t)}{dt}\right)$ , the theoretical spike generator would transfer information about stimulus changes with the same efficiency as it transfers information about sustained values. The transient nature of the information transfer ratio is consistent with a system that is meant to encode stimulus *changes* more efficiently than absolute stimulus values.

The membrane noise model presented in section 4.2.1 is necessary to characterize the probability law governing the EPSP SF inputs. Unless measurement noise and spike separation artifacts can be eliminated, such a model will be needed. When looking at the power spectrum of sample EPSP responses, it appears that this membrane model may not completely characterize the activity. The most dominant characteristics are captured and the present model suffices as a first-order approximation. However, to be more accurate in estimating KL distances between EPSP responses, higher-order models should be explored.

We are presently unable to generate error bars for EPSP KL or information transfer ratio estimates. The bootstrap procedure was employed to calculate error bars in the spike response KL estimates, but the bootstrap procedure cannot be applied effectively to all types of estimators. Methods for quantifying the confidence of the EPSP KL and information transfer ratio estimates should be explored. The confidence bounds for the spike response KL estimates are very wide, and it is desirable increase the confidence of the estimates. The single biggest factor in our estimator accuracy is the amount of available data, and an increase in the dataset size would improve the estimates. The independent bin assumption used in estimating spike response KLs may also be unrealistic and larger datasets would allow for higher order Markov dependence structures to be included.

Finally, the present analysis concentrates on SF performance over a few stimulus features. Larger segments of the system should be analyzed over a wider range of stimulus features. Optomotor neurons receive inputs from the SFs and there may be complicated interactions taking place within the SF ensembles. The optomotor neurons give input to the muscles responsible for eyestalk reflex movement, and this behavior could be considered as one output of the total crayfish visual system. The larger picture of total information processing in the crayfish visual system can only be achieved when the post-sustaining fiber components are also analyzed.

## References

1. S. Ali and S. Silvey. A general class of coefficients of divergence of one distribution from another. *Journal of the Royal Statistical Society, Series B*, 28(1):131–142, 1966.
2. C.S. Burrus, R.A. Gopinath, and H. Guo. *Introduction to Wavelets and Wavelet Transforms: A Primer*. Prentice Hall, Englewood Cliffs, NJ, 1997.
3. W.J. Conover. *Practical Nonparametric Statistics*. John Wiley & Sons, New York, NY, second edition, 1980.
4. T.M. Cover and J.A. Thomas. *Elements of Information Theory*. John Wiley & Sons, Inc., New York, NY, 1991.
5. B. Efron and R.J. Tibshirani. *An Introduction to the Bootstrap*. Chapman & Hall, New York, NY, 1993.
6. R.M. Glantz. Personal communication, 2002.
7. C.M. Gruner. *Quantifying information coding limits in sensory systems*. Doctor of Philosophy, Rice University, Houston, TX, August 1998.
8. C.M. Gruner and D.H. Johnson. Detection of change in periodic, nonstationary data. In *Proceedings of the International Conference on Acoustics, Speech, and Signal Processing*, Atlanta, GA, 1996.
9. M. Gutman. Asymptotically optimal classification for multiple tests with empirically observed statistics. *IEEE Transactions on Information Theory*, 35(2):401–408, March 1989.
10. P. Hall. *The Bootstrap and Edgeworth Expansion*. Springer-Verlag, New York, NY, 1992.
11. D.H. Johnson. Point process models of single-neuron discharges. *J. Comp. Neuroscience*, 3(4):275–299, December 1996.
12. D.H. Johnson, C.M. Gruner, K. Baggerly, and C. Seshagiri. Information-theoretic analysis of neural coding. *J. Comp. Neuroscience*, 10:47–69, 2001.
13. D.H. Johnson, C.M. Gruner, and R.M. Glantz. Quantifying information transfer in spike generation. *Neurocomputing*, 32–33:1047–54, June 2000.
14. D.H. Johnson and G.C. Orsak. Relation of signal set choice to the performance of optimal non-gaussian detectors. *IEEE Transactions on Communications*, 41(9):1319–1328, September 1993.
15. D.H. Johnson and S. Sinanović. Symmetrizing the Kullback-Leibler distance. *submitted to IEEE transactions on Information Theory*, 2001.
16. E.R. Kandel, J.H. Schwartz, and T.M. Jessell. *Principles of Neural Science*. Appleton & Lange, Norwalk, CT, third edition, 1991.

17. M.D. Kirk. *The Crayfish Visual System: Intracellular Studies and Morphologies of Identified Interneurons*. Doctor of Philosophy, Rice University, Houston, TX, April 1982.
18. M.D. Kirk, B. Waldrop, and R.M. Glantz. The crayfish sustaining fibers, I. Morphological representation of visual receptive fields in the second optic neuropil. *Journal of Comparative Physiology*, 146:175–179, 1982.
19. M.D. Kirk, B.R. Waldrop, and R.M. Glantz. The crayfish sustaining fibers, II. Responses to illumination, membrane properties and adaptation. *Journal of Comparative Physiology*, 150:419–425, 1983.
20. J.G. Nicholls, A.R. Martin, B.G. Wallace, and P.A. Fuchs. *From Neuron to Brain*. Sinauer Associates, Inc., Sunderland, MA, fourth edition, 2001.
21. A.V. Oppenheim, R.W. Schaffer, and J.R. Buck. *Discrete-Time Signal Processing*. Prentice Hall, Upper Saddle River, NJ, second edition, 1999.
22. A. Papoulis. *Probability, Random Variables, and Stochastic Processes*. McGraw-Hill Book Company, New York, NY, 1965.
23. L. Rabiner and R. Schaffer. *Digital Processing of Speech Signals*. Prentice Hall, Englewood Cliffs, NJ, 1978.
24. S. Sinanović. Toward a theory of information processing. Master of Science, Rice University, Houston, TX, April 2000.
25. H. Stark and J.W. Woods. *Probability, Random Processes and Estimation Theory for Engineers*. Prentice Hall, Upper Saddle River, NJ, second edition, 1994.
26. B. Waldrop and R.M. Glantz. Synaptic mechanisms of a tonic EPSP in crustacean visual interneurons: Analysis and simulation. *Journal of Neurophysiology*, 54(3):636–650, 1985.
27. C.A.G. Wiersma and T. Yamaguchi. The neuronal components of the optic nerve of the crayfish as studied by single unit analysis. *Journal of Comparative Neurology*, 138:337–358, 1966.

## Appendix A

### Membrane Physiology

We must understand the physiological basis of EPSP generation to develop a model capturing the membrane noise characteristics. The neural membrane is a two-layer lipid structure, approximately 6 nm thick, that is virtually impermeable to ions [20]. An electrical potential across the membrane is created by an excess of cations (positively charged ions) and anions (negatively charged ions) on opposite sides of the membrane. For example, a negative membrane potential is produced by an excess of anions inside and cations outside the membrane with equal and opposite charges. Both the intracellular cytoplasm and the extracellular solution are electrically neutral, so the strongest electrical force these ions feel is their mutual attraction. The excess ions will be attracted toward each other but remain separated by the impermeable cell membrane. Cell membranes separate and store ionic charge the same way capacitors function with free electrons.

While the lipid membrane itself is impermeable to ions, it is embedded with proteins forming ion channels. These channels can be non-selective, but are frequently specific. They can allow only cation or anion movement, and sometime are specific to a particular ion species. These channels open and close stochastically, with the probability of opening frequently influenced by the presence of a stimulating factor. For *voltage-gated channels* the probability of a channel opening increases with electrical potential across the membrane. For *ligand-gated channels*, the probability of a channel opening increases in the presence of a specific chemical agent (the preferred agent can vary between channels) [16, 20]. Ion channels allow passive ion movement across the cell membrane when they are in the open state. By controlling the probability of a channel being open at any given time, the gating stimulus determines the channel's ability to allow ionic movement. In electrical



terms, the gating condition (along with the channel's inherent properties) controls the membrane *conductance* for an ion. Conductance ( $G$ ) is measured in Siemens and is the reciprocal of resistance ( $R = 1/G$ ). The membrane conductance for a specific ion depends on the single open channel conductance and the average number of open channels. The net membrane conductance is a function of the individual ionic membrane conductances. The membrane ionic current through an ion channel at a specific time depends on both the amount of gating condition present and the electrochemical gradient providing the driving force.

The four most significant ions in neurophysiology are sodium ( $\text{Na}^+$ ), potassium ( $\text{K}^+$ ), calcium ( $\text{Ca}^{2+}$ ) and chloride ( $\text{Cl}^-$ ). These ions are present in different concentrations in both the intracellular cytoplasm and the extracellular solution. An individual ionic membrane current is given by Ohm's Law, given by

$$I_{\text{K}^+} = (G_{\text{K}^+})(V_{\text{K}^+}), \quad (\text{A.1})$$

for the  $\text{K}^+$  example. The ionic current depends on both the membrane ionic conductance and the driving force (voltage) applied to the ion species. A membrane electrical potential exerts force on any charged ion. However, for each ion species, an intracellular and extracellular concentration imbalance creates a chemical potential that also exerts a driving force. The electrochemical potential provides the net ionic driving force. For example, if there is a higher concentration of  $\text{K}^+$  inside the cell than outside, the chemical gradient draws  $\text{K}^+$  molecules out of the cell. If there is also a negative membrane electrical potential, the negatively charged intracellular space will draw positively charged  $\text{K}^+$  ions in. Given the intracellular and extracellular concentrations of an ion species, there is a membrane *equilibrium potential* where the electrical and chemical potentials are equal and opposite, producing zero net ionic movement. The equilibrium potential is given by the Nernst

equation [20], which (staying with the  $K^+$  ion example) is given by

$$E_{K^+} = \frac{RT}{zF} \ln \left( \frac{K_{out}^+}{K_{in}^+} \right), \quad (A.2)$$

where  $R$  is the thermodynamic gas constant,  $T$  is the absolute temperature,  $z$  is the valence of the ion,  $F$  is Faraday's constant and  $\left( \frac{K_{out}^+}{K_{in}^+} \right)$  is the ratio of extracellular and intracellular  $K^+$  concentrations. If  $V_m$  is the membrane electrical potential (typically in the range  $-(60-80)$  mV), then the net driving force on  $K^+$  ions would be  $(V_m - E_{K^+})$ . Substituting back into equation (A.1), the total  $K^+$  current is

$$I_{K^+} = (G_{K^+})(V_m - E_{K^+}). \quad (A.3)$$

Given the intracellular and extracellular concentrations of any ion, the equilibrium potential for that ion can be calculated using the Nernst equation (A.2). The membrane potential determines the ionic driving force and Ohm's law (A.3) calculates net ionic current. Sodium and potassium are the two ions we will focus on presently. Typical neurons have much higher concentrations of  $K^+$  inside than out, and much higher concentrations of  $Na^+$  outside than in.

When there is no signaling activity (no EPSP present), the membrane is said to be at rest. In the resting state, the membrane electrical potential as well as intracellular and extracellular ionic concentrations are at steady-state values. In the resting state there is zero net current across the membrane, as well as zero net ionic current for every ion species. Because there is only one membrane electrical potential ( $V_m$ ) but each ion will have it's own equilibrium potential ( $E_{Na^+}, E_{K^+}, E_{Ca^{2+}}, E_{Cl^-}$ ), zero net ionic current can only be achieved for every species because of active ion movement against the electrochemical gradient. Active pumps in the cell membrane expend metabolic energy transporting sodium out of the cell and potassium in, both against their

electrochemical gradients. The pumps are electrogenic, moving three sodium molecules out for every two potassium molecules in, resulting in a net outward current [20]. A zero net ionic current requires that the passive ionic currents must be equal and opposite the currents due to the active pump. Mathematically this is stated as  $\frac{I_{Na+}}{I_{K+}} = -\frac{3}{2}$ . Requiring the net membrane current to be zero means that the ionic currents must be equal and opposite as well,  $\frac{3}{2}(I_{K+}) = \frac{3}{2}(G_{K+})(V_m - E_{K+}) = -(I_{Na+}) = -(G_{Na+})(V_m - E_{Na+})$ . Solving for  $V_m$ , the resting membrane potential is given by:

$$V_m = \frac{1.5(G_{K+})(E_{K+}) + (G_{Na+})(E_{Na+})}{1.5(G_{K+}) + (G_{Na+})}. \quad (A.4)$$

Equation (A.4) is a variation of the Goldman constant field equation [20]. Equation (A.4) can be extended to include other ion species that contribute to the resting membrane potential.

A compound EPSP in the integrative region is a composite of individual EPSPs originating in the input region (generally the dendritic tree). As described in section 2.1, these individual EPSPs are generated by the presence of neurotransmitter released from an adjacent neuron's presynaptic terminal. The chemical neurotransmitter is the activating condition for ligand-gated ion channels in the postsynaptic terminal. Each individual ion channel has a fixed conductance, but an elevated gating condition increases the average number of open channels, thereby increasing the net membrane conductance. Increased conductance allows more free ions to traverse the cell membrane, contributing to the EPSP. The conductance change responsible for EPSP generation has been measured in crayfish SFs by Waldrop and Glantz, [26]. The measured relationship between increasing membrane conductance and EPSPs is critical to the membrane noise model developed in section 4.2.1.

## Appendix B

### Correlation structure of a non-stationary system

Consider a white Gaussian noise process  $W(n) \sim N(0, \sigma^2)$ . The colored Gaussian noise process  $C(n)$  is created by filtering  $W(n)$  by the non-stationary, first-order AR system described by the difference equation

$$C(n) = a(n)C(n-1) + W(n),$$

where  $a(n)$  is a time-varying pole. The unit pulse response of this system is given by

$$h(n, k) = \left( \prod_{l=k+1}^n a(l) \right) \delta(n - k), \quad (\text{B.1})$$

the system response at sample  $n$  to a unit pulse at sample  $k$ ,  $\delta(k)$ . It is important to note a notation convention here. The product operator used in equation (B.1) is defined to be zero for any terms where the lower index exceeds the upper index,  $\prod_{l=\alpha}^{\beta} x(l) = 0, \alpha > \beta$ . The colored noise process  $C(n)$  can be written in terms of the unit pulse response,

$$C(n) = \sum_{k=-\infty}^n h(n, k) W(k).$$

Making the variable substitution  $l = n - k$ , the expression for  $C(n)$  simplifies to

$$\begin{aligned}
 C(n) &= \sum_{l=0}^{\infty} h(n, n-l) W(n-l) \\
 &= \sum_{l=0}^{\infty} \left( \prod_{k=n-l+1}^n a(k) u(n - (n-l)) + \delta(n - (n-l)) \right) W(n-l) \\
 &= W(n) + \sum_{l=1}^{\infty} \left( \prod_{k=n-l+1}^n a(k) W(n-l) \right). \tag{B.2}
 \end{aligned}$$

The correlation function for the non-stationary system is found from the general definition of correlation,  $\Phi(n, m) = E[C(n)C(m)]$ . Because  $W(n)$  is a white noise process, its correlation function is  $E[W(n)W(m)] = \sigma^2 \delta(m - n)$ . The white noise correlation function simplifies the colored noise correlation function to:

$$\begin{aligned}
 E[C(n)C(m)] &= \sigma^2 \delta(m - n) + \sigma^2 \left( \sum_{l=1}^{\infty} \prod_{k=n-l+1}^n a(k) \delta(m - n + l) \right) \\
 &\quad + \sigma^2 \left( \sum_{q=1}^{\infty} \prod_{r=m-q+1}^m a(r) \delta(n - m + q) \right) \\
 &\quad + \sigma^2 \left( \sum_{l,q=1}^{\infty} \prod_{k=n-l+1}^n a(k) \prod_{r=m-q+1}^m a(r) \delta(n - l + q - m) \right) \\
 E[C(n)C(m)] &= \sigma^2 \delta(m - n) + \sigma^2 \left( \prod_{k=n-(n-m)+1}^n a(k) \right) + \sigma^2 \left( \prod_{r=m-(m-n)+1}^m a(r) \right) \\
 &\quad + \sigma^2 \left( \sum_{l=1}^{\infty} \prod_{k=n-l+1}^n a(k) \prod_{r=m-(m-n+l)+1}^m a(r) \right).
 \end{aligned}$$

The correlation function for a non-stationary, first order AR system is therefore given by:

$$\begin{aligned} \Phi(n, m) = & \sigma^2 \left( \delta(m - n) + \left( \prod_{k=m+1}^n a(k) \right) + \left( \prod_{r=n+1}^m a(r) \right) \right. \\ & \left. + \left( \sum_{l=1}^{\infty} \prod_{k=n-l+1}^n a(k) \prod_{r=n-l+1}^m a(r) \right) \right). \end{aligned}$$

## Appendix C

### Analytic Analysis of Theoretical Spike Generator

Consider a system that takes a Gaussian random variable  $\tilde{X} \sim N(\theta, \tilde{\sigma}^2)$  as input, and produces as output a Poisson random variable  $\tilde{Y}$  with rate parameter  $\lambda = G\tilde{X}$  (where  $G$  is a deterministic gain). We want to calculate a KL distance between two input Gaussian random variables with different means, as well as the KL between the resulting output Poisson random variables. The KL between two Gaussian random variables is straightforward, and described in section 4.2. Calculating the output between two Poisson random variables is also trivial given the probability mass function for the event counts.

The conditional probability mass function for  $\tilde{Y}$  is

$$P_{\tilde{Y}}(n|\lambda) = \frac{(\lambda T)^n e^{-\lambda T}}{n!}.$$

To simplify the notation, we set  $T = 1$ . Because  $\tilde{X}$  is a Gaussian random variable,  $\lambda$  is also a Gaussian random variable. To analytically calculate a KL distance, we must find the *unconditional* probability mass function describing the output counts. The unconditional probability mass function for the output  $\tilde{Y}$  is given by

$$P_{\tilde{Y}}(n) = \int_0^\infty \frac{\lambda^n e^{-\lambda}}{n!} P_{(G\tilde{X})}(\lambda) d\lambda. \quad (\text{C.1})$$

The unconditional probability mass function simplifies by calculating the  $Z$ -transform of equation

(C.1):

$$\sum_{n=0}^{\infty} \left( \int_0^{\infty} \frac{\lambda^n e^{-\lambda}}{n!} P_{(G\tilde{X})}(\lambda) d\lambda \right) z^n = \int_0^{\infty} e^{\lambda(z-1)} P_{(G\tilde{X})}(\lambda) d\lambda. \quad (C.2)$$

The simplified equation (C.2) is the Laplace transform of  $P_{(G\tilde{X})}(\lambda)$ , evaluated at  $s = z - 1$ . The Laplace transform of a probability density function is also known as the “moment generating function” [25] for the random variable. For a Gaussian, the moment generating function is

$$M_{\tilde{X}}(s) = e^{\left(\frac{s^2 \tilde{\sigma}^2}{2} + s\theta\right)}. \quad (C.3)$$

The simplification of equation (C.2) follows from equation (C.3) (with  $\tilde{X} \sim N(\theta, \tilde{\sigma}^2)$ ):

$$M_{\lambda}(z - 1) = M_{(G\tilde{X})}(z - 1) = e^{\left(\frac{(z-1)^2 G^2 \tilde{\sigma}^2}{2} + G(z-1)\theta\right)}. \quad (C.4)$$

The unconditional probability mass function describing output counts is the inverse  $Z$ -transform of equation (C.4), which is very difficult to compute directly. The inverse  $Z$ -transform can also be calculated by finding the Taylor series expansion around zero (using a symbolic mathematics package). In practice only a finite number of terms in the probability mass function can be found, but the number of terms can be chosen large enough so that the remaining probabilities are very small and are not considered.

There is a detail in this derivation that must be noted. A Gaussian random variable technically has infinite support. The rate parameter  $\lambda$  for the Poisson output is found by a simple scaling of the input Gaussian random variable, but  $\lambda$  cannot be negative. If  $\theta$  is large compared to  $\tilde{\sigma}^2$ , the probability of a negative value for  $\tilde{X}$  will be very small. The corresponding probability of a negative  $\lambda$  will be small enough to have no significant effect on our calculations.